Year : 2019

On the Thermo-Mechanics of Ductile Strain Localization in the Lithosphere and New Steps towards a Nappe Theory of the Helvetic Alps

Kiss Daniel

UNIL | Université de Lausanne
Institut des sciences de la Terre

Faculté des géosciences et de l'environnement
Institut des sciences de la Terre

On the thermo-mechanics of ductile strain localization in the Lithosphere and new steps towards a nappe theory of the Helvetic Alps

Thèse de doctorat

présentée à la Faculté des géosciences et de l'environnement de l'Université de Lausanne
pour l'obtention du grade de Docteur en sciences de la Terre par

Dániel Kiss

MSc en géophysique, l'Université Eötvös Loránd, Budapest

Jury

Prof. Dr. Othmar Müntener	UNIL	Président du jury
Prof. Dr. Stefan M. Schmalholz	UNIL	Directeur de thèse
Prof. Dr. Yury Y. Podladchikov	UNIL	Expert interne
Prof. Dr. Jean-Luc Epard	UNIL	Expert interne
Prof. Dr. Yuri Fialko	UCSD, SIO	Expert externe

UNIL | Université de Lausanne
Faculté des géosciences et de l'environnement
bâtiment Géopolis bureau 4631

IMPRIMATUR

Vu le rapport présenté par le jury d'examen, composé de

Président de la séance publique :	M. le Professeur Othmar Müntener
Président du colloque :	M. le Professeur Othmar Müntener
Directeur de thèse :	M. le Professeur Stefan Schmalholz
Expert interne :	M. le Professeur Yury Podladchikov
Expert interne :	M. le Professeur Jean-Luc Epard
Expert externe :	M. le Professeur Yuri Fialko

Le Doyen de la Faculté des géosciences et de l'environnement autorise l'impression de la thèse de

Monsieur Daniel KISS

Titulaire d'un
Master en géophysique
De l'Université Eötvös Lorand de Budapest

intitulée

On the Thermo-Mechanics of Ductile Strain Localization in the Lithosphere and New Steps towards a Nappe Theory of the Helvetic Alps

Lausanne, le 10 octobre 2019

Pour le Doyen de la Faculté des géosciences et de l'environnement

Professeur Othmar Müntener

ABSTRACT

The generation of ductile shear zones is essential for the formation of tectonic plate boundaries, such as subduction or strike-slip zones. Ductile shear zones are one of the most prominent geological features on the tectonic nappe, outcrop and micro-structural scales too. However, the primary mechanism of ductile strain localization is still contentious.

In the first paper of this thesis we study the spontaneous generation of ductile shear zones by thermal softening using thermo-mechanical numerical simulations for linear and power-law viscous flow in one-dimension (1D), 2D and 3D. We provide a temperature and thickness prediction that requires knowledge of only the boundary velocity, flow law and thermal parameters, but no *a priori* information about the shear zone itself, such as thickness, stress and strain rate. The prediction is valid for 1D, 2D and 3D shear zones in bulk pure and simple shear. Applying typical flow laws for lithospheric rocks shows that shear zone generation by thermal softening occurs for typical plate tectonic velocities of few cm.yr^{-1} or strain rates between 10^{-16} and 10^{-14} s^{-1}.

In the second paper of this study we present two-dimensional numerical simulations of convergence at a hyper-extended passive margin with exhumed sub-continental mantle. We consider visco-elasto-plastic deformation, heat transfer and thermo-mechanical coupling by shear heating and associated thermal softening due to temperature dependent viscosity. The simulations show subduction initiation for convergence velocities of 2 cm.yr^{-1}, Moho temperatures between 525 and 600 °C and reasonable maximal deviatoric stresses around the Moho of ca 800 MPa. Subduction initiates in the region with thinned continental crust and is controlled by a thermally-activated ductile shear zone in the mantle lithosphere. The shear zone temperature can be predicted with a recently published analytical equation. The modeled forced subduction agrees with geological data and reconstructions of subduction during closure of the Piemont-Liguria basin during Alpine orogeny.

Tectonic nappes are observed for more than a hundred years. Although geological studies often refer to a "nappe theory", the physical mechanisms of nappe formation are still incompletely understood. In the third paper we present results of two-dimensional numerical simulations of shortening of a passive margin, to investigate the thermo-mechanical processes of detachment, transport and stacking of nappes. We apply a visco-elasto-plastic rheology and we consider tectonic inheritance with two initial mechanical heterogeneities: (1) lateral heterogeneity of the basement-cover interface due to half-grabens and horsts and (2) vertical heterogeneities due to layering of mechanically strong and weak sedimentary units. The model shows the detachment and horizontal transport of a thrust nappe and stacking of this thrust nappe above a fold nappe. We apply our model to the Helvetic nappe system in Western Switzerland. The modelled structures and temperature field agree with data from the Helvetic nappe system, which is characterised by stacking of the Wildhorn thrust nappe above the Morcles fold nappe.

SUMMARY FOR THE GENERAL PUBLIC

Deformation is often observable in rocks, such as folds, or ruptures with noticeable displacements. One of the most spectacular examples on the large scale (scale of mountains) is located along the Rhone Valley near Martigny, in Switzerland. Here, a several km thick and tens of km long packet of folded sedimentary rocks, the so-called Morcles fold nappe can be found. It is easily observable for example on the Dent de Morcles and on the Dents du Midi. On the top of the Morcles nappe another nappe, the Wildhorn, is located. The Wildhorn nappe is a packet of rock that has been transported over the basal shear zone or thrust (a sliding surface with intense shear deformation) several tens of km from its original place. It is observable for example on the Wildhorn or on the Les Diablerets. Although such nappes are observed for more than a hundred years, the physical mechanisms of nappe formation are still incompletely understood.

On the global scale, rock deformation is characterized by zones of intense and localized deformation separated by domains of little or no deformation. This deformation mode is reflected by plate tectonics. The strong outermost shell of the Earth (lithosphere) consists of several tectonic plates, that are floating on a weak shell (asthenosphere), each of them moving in its own direction. Lithospheric deformation is typically localized at plate boundaries, where two plates meet. Such localized deformation behavior is natural in the brittle-frictional regime (when rocks break in an everyday sense). However, in the ductile regime (when rocks flow or slowly creep, typically in a few tens of km depth) deformation tends to be distributed. Understanding the physical processes that are promoting localized ductile deformation over distributed ductile deformation is a key to understand plate tectonics better.

The aim of this thesis is to formulate and apply models, based on continuum mechanics, to understand spontaneous ductile strain localization and nappe formation. In the first paper of the thesis we study spontaneous generation of ductile shear zones by thermal softening and shear heating, that is the conversion of dissipative work into heat. Based on a simple 1D model we determined a new analytical formula that could be used to estimate temperatures of shear zones. In the second paper of this thesis we present result of 2D numerical simulations on subduction initiation. Subduction initiation is when a new plate boundary forms, where the two plates move towards each other, one of the two moves below the other and sinks into the asthenosphere. We demonstrate that spontaneous generation of ductile shear zones is a feasible mechanism of subduction initiation. We show that the analytical formula, presented in the first paper is applicable for lithospheric scale scenarios with complex rheology and geometry. In the third paper of this thesis we present a new mechanical model of detachment, transport and stacking of tectonic nappes, applied to the Helvetic Nappe System. The modeled structures and temperature field agree with the data from the Helvetic Nappe System, which is characterized by stacking of the Wildhorn thrust nappe above the Morcles fold nappe.

RÉSUMÉ

La formation des zones de déformation ductile est essentielle pour la formation des limites des plaques tectoniques, comme les zones de subduction ou les zones de failles transformantes. Les zones de déformation ductiles sont l'une des formations géologiques les plus importantes pour la compréhension des nappes tectoniques, y compris à l'échelle de l'affleurement et de l'analyse structurale microscopique. Cependant, le mécanisme principal de la localisation de la déformation ductile est toujours controversé.

Dans le premier article de cette thèse, nous étudions la génération spontanée des zones de cisaillement ductile par ramollissement dû à la chauffe (thermal softening) à l'aide de simulations numériques thermo-mécaniques en une dimension (1D), en 2D et en 3D pour des lois de fluage visqueuses linéaire et de loi de puissance. La prédiction de la température nécessite de connaître uniquement la vitesse des conditions de bordure, les lois de fluage et les paramètres thermiques, mais a priori pas d'information sur la zone de cisaillent en elle-même, comme l'épaisseur, le stress et le taux de déformation. La prédiction est valide pour les zones de cisaillement en 1D, 2D et 3D dans un contexte de cisaillement pur à grande échelle, et de cisaillement simple. L'utilisation de lois de fluage typique pour des roches lithosphériques montre que la génération des zones de cisaillement par le ramollissement dû à la chauffe (thermal softening) se produit pour des valeurs de vitesse de plaques tectoniques typiques de quelques cm·an-1 ou pour un taux de déformation entre 10^{-16} et 10^{-14} s^{-1}. Les résultats indiquent que la modification de la structure et des paramètres physiques d'une roche uniquement à cause de la température est un mécanisme possible pour la génération spontanée d'une zone de cisaillement dans la lithosphère.

Dans le second article de cette étude, nous présentons des simulations numériques en deux dimensions de convergence de plaque à une marge passive hyper-étendue avec exhumation de manteau subcontinental. Nous considérons une déformation visco-elasto-plastique, un transfert de chaleur et un couplage thermo-mécanique par chauffe due au frottement (shear heating) et par ramollissement thermique (thermal softening) dû à la viscosité qui est dépendante de la température. Les simulations montrent une vitesse de convergence de 2 cm/an, une température du Moho entre 525 et 600 °C ainsi qu'un stress déviatorique maximal situé au Moho d'environ 800 MPa. Ces valeurs sont raisonnablement concordantes avec des données observées dans la nature. La subduction s'initie dans la région oú la croûte continentale est la plus fine et est contrôlée par l'activation thermique d'une zone de cisaillement dans le manteau lithosphérique. La température de la zone de cisaillement peut être prédite par une équation analytique publiée récemment. Le modèle de subduction forcée est en accord avec les données géologique et les reconstructions de subduction pendant la fermeture du bassin du Piemont-Ligurie durant l'orogenèse alpine.

Les nappes tectoniques sont observées depuis plus de cent ans. Bien que les études géologiques se réfèrent souvent à la « théorie des nappes », les mécanismes physiques qui forment ces nappes sont encore mal compris. Dans le troisième article, nous présentons les résultats des simulations numériques en deux dimensions d'un raccourcissement d'une marge passive pour investiguer le processus thermo-mécanique de détachement, de trans-

port et d'empilement des nappes. Nous utilisons une rhéologie visco-elasto-plastique et nous considérons des héritages tectoniques avec deux hétérogénéités mécaniques initiales : (1) une hétérogénéité latérale de l'interface socle- couverture due aux demi-grabens et horst et (2) une hétérogénéité verticale due à l'alternance de couches mécaniquement dures et faibles des unités sédimentaires. Le modèle montre le détachement et le transport horizontal d'une nappe chevauchante et de l'empilement de cette nappe sur une nappe plissée. Nous appliquons notre modèle au système des nappes hélvétiques en Suisse occidentale. Les structures modélisées et le champ de température concordent avec les données du système des nappes helvétiques, caractérisé par l'empilement de la nappe de charriage du Wildhorn au-dessus de la nappe plissée de Morcles.

RÉSUMÉ GRAND PUBLIC

La déformation est souvent observée dans les roches, comme des plis, ou des ruptures avec des déplacements notables. L'un des exemples les plus spectaculaires à grande échelle (à l'échelle des montagnes) est situé le long de la vallée du Rhône, proche de Martigny, en Suisse. On y trouve un paquet de roches sédimentaires plissées de plusieurs km d'épaisseur et de dizaines de km de long, appelé pli de la nappe de Morcles. Il est facilement observable par exemple sur la Dent de Morcles ou sur les Dents du Midi. La nappe du Wildhorn, autre nappe tectonique alpine, se trouve au-dessus de la nappe de Morcles. La nappe du Wildhorn est un paquet de roche qui a été transportée par- dessus la zone de cisaillement basale ou le chevauchement (une surface de glissement avec une déformation de cisaillement intense) de plusieurs dizaines de km de sa place d'origine. Ce déplacement est observable par exemple sur le Wildhorn ou sur les Diablerets. Bien que ces nappes sont observées depuis plus de cent ans, les mécanismes physiques qui forment ces nappes sont encore mal compris. A l'échelle globale, la déformation des roches est caractérisée par des zones de déformations intenses et la localisation de la déformation est séparée par des domaines de petites déformation ou des domaines sans déformation. Ce mode de déformation est reflété par la tectonique des plaques. La couche dure la plus externe de la Terre (la lithosphère) est constituée de plusieurs plaques tectoniques, qui flottent sur une couche plus faible (l'asthénosphère), chacune de ces plaques bougent entre elles en suivant leur propre direction. La déformation lithosphèrique est typiquement localisée en bordure de plaque, oú deux plaques se rencontre. Ce comportement de localisation de la déformation est naturel dans le régime de déformation cassant (lorsque des roches se brisent au quotidien). Toutefois, en régime ductile (lorsque les roches s'écoulent ou fluent lentement, généralement à quelques dizaines de km de profondeur), la déformation a tendance à se répartir. Comprendre les processus physiques qui favorisent la localisation de la déformation ductile par rapport à la distribution de la déformation ductile est une clé pour mieux comprendre la tectonique des plaques.

L'objectif de cette thèse est de formuler et d'appliquer des modèles, basés sur la mécanique des milieux continus, pour comprendre la localisation spontanée des contraintes ductiles et la formation des nappes. Dans le premier article de cette thèse nous étudions la génération spontanée des zones de cisaillement ductiles par ramollissement dû à la température (thermal softening) et par chauffe de frottement (shear heating) c'est-à-dire à la conversion du travail dissipatif en chaleur. Sur la base d'un modèle simple 1D, nous avons déterminé une nouvelle formule analytique pouvant être utilisée pour estimer la température des zones de cisaillement. Dans le deuxième article, nous présentons les résultats de simulations numériques 2D sur l'initiation de la subduction. L'initiation à la subduction se produit lorsqu'une nouvelle limite de plaque se forme, oú les deux plaques se rapprochent l'une de l'autre, et oú l'une des deux plaques passe en dessous de l'autre et plonge dans l'asthénosphère. Nous démontrons que la génération spontanée des zones de cisaillement ductile est un mécanisme possible pour l'initiation de la subduction. Nous montrons que la formule analytique présentée dans notre premier article peut s'appliquer aux scénarios à l'échelle lithosphérique avec une rhéologie et une géométrie complexe. Dans le troisième article de cette thèse, nous présentons un nouveau modèle mécanique de détachement, de

transport et d'empilement de nappes tectoniques, appliqué au système des nappes helvétiques. Les structures modélisées et le champ de température concordent avec les données du système des nappes helvétiques, caractérisé par l'empilement de la nappe de charriage du Wildhorn au-dessus de la nappe plissée de Morcles.

Contents

CHAPTER 1

Introduction

Ductile shear zones are one of the most important geological features, that appear on most geological length scales and their lifespan covers a significant range of the geologically important time scales. Shear zones are not only interesting geological features, but the physical processes involved in the formation of shear zone could possibly have great implications for geodynamics, or lithospheric dynamics. A significant part of the lithosphere is dominated by ductile deformation, mostly because with increasing confining pressure brittle failure becomes increasingly unlikely (e.g. Burov et al., 2006). Therefore, the generation of ductile shear zones is essential for the formation of tectonic plate boundaries, such as subduction or strike-slip zones (e.g. Regenauer-Lieb et al., 2001; Bercovici and Ricard, 2012; Thielmann and Kaus, 2012). Although the importance of understanding ductile strain localization is clear (Poirier, 1980), the primary mechanism of ductile strain localization is still contentious.

In this thesis I am using models, based on continuum mechanics to investigate physical mechanisms related to ductile strain localization. I focus on two scenarios: (i) spontaneous ductile strain localization by shear heating and thermal softening and (ii) strain localization (or partitioning) due to the presence of inherited mechanical heterogeneities during tectonic nappe formation.

1.1 Definitions

Some of the terms in this thesis either do not have a clear definition or they might have conflicting meaning in different scientific communities, therefore I clarify the most important ones here.

We use **brittle** deformation interchangeably with **plastic** deformation.

The term, **detachment** of a nappe, we use to describe the situation, when the rock units, forming the frontal part of a thrust sheet are being separated from their original position. After this a low angle shear zone, similar to a detachment zone (décollement), can develop.

Dissipation happens when energy in some initial form is converted irreversibly into a final form. In other words, all processes that result in entropy production are dissipative (and irreversible too). After the first chapter we use **dissipation** as an abbreviation of "dissipation due to the conversion of the mechanical work that is used for non-elastic shear deformation into heat", which is interchangeable with **shear heating**.

Ductile deformation is, when the macroscopic (much larger than an individual dislocation) deformation behavior is described mathematically by a relation between stress and strain rate, such as by flow laws for diffusion, dislocation or Peierls creep (i.e. low temperature plasticity). This is a scale independent definition!

Induced or forced subduction initiation (SI) is caused by forces originating far away from the SI site, typically due to far-field plate motions.

A tectonic **nappe** is a rock packet not in its place, resting on a substratum that is not its original one. The nappes discussed in this thesis, extend a few km vertically, and tens of km horizontally.

Plastic deformation occurs, when the plastic yield strength (pressure sensitive for most rock) is reached. In the numerical models, presented here, it is represented by Drucker-Prager plasticity.

Spontaneous shear zone generation is, when the fundamental shear zone parameters, such as thickness, shear stress and strain rate, are not *a priori* prescribed by the natural or model configuration.

Spontaneous subduction initiation (SI) is caused by forces originating at the site of the SI. It is typically associated with significant lateral variation of buoyancy.

1.2 From fundamental laws of physics to continuum mechanics

My goal here is to show, how the mathematical models that are most commonly used in geodynamics can be derived from the fundamental laws of physics (with the help of certain phenomenological laws). None of this material is a new scientific result. I use the framework of classical irreversible thermodynamics (e.g. De Groot and Mazur, 1984; Müller and Müller, 2009) to couple the laws of classical mechanics and thermodynamics. Most importantly, I will check that the system of equations satisfies the fundamental laws of physics. I derive a self-consistent system of equations, that describes shear heating and thermal softening in a viscous material. Here I do not show more, but the realm of possibilities extends much further.

1.2.1 Realm of applicability

In general, continuum mechanics is applicable if the characteristic length of the studied process is much larger than the average mean free path of particles, that is ca 10^{-9} m in liquids and solids (e.g. Chung, 1988). Our system of governing equations is based on Newtonian mechanics, that is applicable for most processes on Earth (e.g. provided that velocities are much smaller than the speed of light).

In this exercise I consider an isotropic, single phase (no percolating fluids) material, that is deforming viscously in an external gravity field. Compositional differences are possible, but they are only reflected in variable material properties. This means no chemical interaction of any kind are permitted (i.e. diffusion or reactions). I also neglect nuclear reactions (i.e. radioactive decay) and interactions between the model material and electromagnetic fields. I refer to all these assumptions as the axiom.

1.2.2 Index notation

I use a notation, where vectors and tensors are represented with the subscripts i,j,k... that can take the values 1,2 and 3 representing components in the three directions of orthonormal basis vectors. So instead of $\underline{v} = [v_x, v_y, v_z]$ we use $v_i = [v_1, v_2, v_3]$, similarly for tensors. If indices are repeated within a term that implies summation: $M_{ij}N_{ij} = \sum_{i=1}^{3}\sum_{j=1}^{3} M_{ij}N_{ij}$. If I use subscripts to distinguish similar quantities, the spatial indexes

are displayed as superscripts, with no further implications (e.g. $q_E^j = [q_E^1, q_E^2, q_E^3]$ is the energy flux vector).

1.2.3 Conservation of mass (continuity equation)

Assume a continuum of a given density $\rho(x_j, t)$ and take an arbitrary volume of this continuum, that is in rest (has a stationary shape and position). The total mass in this volume can be given as the integral of the density inside this volume:

$$m(t) = \int \rho(x_j, t) \, \mathrm{d}V. \tag{1.1}$$

Due to the conservation of mass, the total mass in this volume can change only if matter flows in or out of this volume (i.e. it cannot be created or destroyed). We can calculate the change of total mass by integrating the material flux through the surface of this volume:

$$\mathrm{d}m = - \oint (\rho v_j \mathrm{d}t) \, \mathrm{d}A_j, \tag{1.2}$$

where A_j is the surface vector with the length of its area and with the direction normal to the surface, pointing outward (note that $v_j \mathrm{d}t \mathrm{d}A_j$ gives a volume that crossed the boundary surface). Now we can write an ordinary differential equation to describe change of mass with time:

$$\frac{\mathrm{d}m}{\mathrm{d}t} = \frac{\mathrm{d}}{\mathrm{d}t} \left(\int \rho \, \mathrm{d}V \right) = - \oint \rho v_j \, \mathrm{d}A_j. \tag{1.3}$$

This is the so-called integral form of the conservation equation.
Since V is not time dependent, we can use the Leibniz rule to change the order of differentiation and integration in the middle term, and the Gauss-Ostrogradsky theorem (divergence theorem) to reformulate the surface integral on the right hand side as a volume integral

$$\int \frac{\partial \rho}{\partial t} \mathrm{d}V = - \int \frac{\partial \rho v_j}{\partial x_j} \, \mathrm{d}V. \tag{1.4}$$

This can be reformulated as

$$\int \frac{\partial \rho}{\partial t} + \frac{\partial \rho v_j}{\partial x_j} \, \mathrm{d}V = 0. \tag{1.5}$$

If this relationship is true for any arbitrary volume then this integral is satisfied if the integrand is zero

$$\frac{\partial \rho}{\partial t} + \frac{\partial \rho v_j}{\partial x_j} = 0. \tag{1.6}$$

This is the so-called divergence form of the conservation equation (also called conservative form). An alternative form, using material time derivatives, is:

$$\frac{1}{\rho} \frac{\mathrm{d}\rho}{\mathrm{d}t} = -\rho \frac{\mathrm{d}}{\mathrm{d}t} \left(\frac{1}{\rho} \right) = - \frac{\partial v_j}{\partial x_j}. \tag{1.7}$$

Using the chain rule one can show that the term in the middle equals to the left hand side. This form will be more convenient later on.

Leibniz integral rule

The derivative of an integral of a scalar field $f(x_i, t)$ is

$$\frac{\mathrm{d}}{\mathrm{d}t}\left(\int_a^b f(x,t)\ \mathrm{d}x\right) = \int_a^b \frac{\partial f(x,t)}{\partial t}\ \mathrm{d}x,$$

if the integration bounds a and b are constants (with respect to t in this case).

Gauss-Ostrogradsky theorem (divergence theorem)

Let us assume that V is a finite volume of the three dimensional space ($\mathbf{R}^3$) and it is bounded by piecewise smooth surfaces A_j. If F_j is a vector-field that is differentiable on V, then the following relationship applies between volume and surface integrals of F_j:

$$\int \frac{\partial F_j}{\partial x_j}\mathrm{d}V = \oint F_j \mathrm{d}A_j.$$

Chain rule

$$\frac{\mathrm{d}f(g(t))}{\mathrm{d}t} = \frac{\mathrm{d}f(g(t))}{\mathrm{d}g(t)}\frac{\mathrm{d}g(t)}{\mathrm{d}t}$$

Example: Transition from material derivatives of ρ to material derivatives of $1/\rho$ in the continuity equation

$$-\rho\frac{\mathrm{d}}{\mathrm{d}t}\left(\frac{1}{\rho}\right) = -\rho\frac{\mathrm{d}\rho^{-1}}{\mathrm{d}t} = -\rho\frac{\mathrm{d}\rho^{-1}}{\mathrm{d}\rho}\frac{\mathrm{d}\rho}{\mathrm{d}t} = -\rho\left(-\rho^{-2}\right)\frac{\mathrm{d}\rho}{\mathrm{d}t} = \frac{1}{\rho}\frac{\mathrm{d}\rho}{\mathrm{d}t}.$$

1.2.4 Balance of any specific (per unit mass) physical quantity

In continuum dynamics, the balance of any specific (per unit mass) physical quantity (let us call it M) can be written in the following (conservative or divergence) form:

$$\frac{\partial \rho M}{\partial t} + \frac{\partial(\rho v_j M + q_M^j)}{\partial x_j} = Q_M, \tag{1.8}$$

where q_M is the non-convective flux of M and Q_M is the (local) source of M. This formulation is preferable for conservative numerical schemes, but it is more convenient to use material derivatives to derive fluxes and to check thermodynamic admissibility. Using differentiation rules (sum and product rules) we get

$$\rho\frac{\partial M}{\partial t} + M\frac{\partial \rho}{\partial t} + \rho v_j\frac{\partial M}{\partial x_j} + \rho M\frac{\partial v_j}{\partial x_j} + v_j M\frac{\partial \rho}{\partial x_j} + \frac{\partial q_M^j}{\partial x_j} = Q_M. \tag{1.9}$$

Note that, the blue terms sum up to zero, due to the conservation of mass (eq. 2.1), so

$$\rho\left(\frac{\partial M}{\partial t} + v_j\frac{\partial M}{\partial x_j}\right) + \frac{\partial q_M^j}{\partial x_j} = Q_M. \tag{1.10}$$

Now we can write our balance laws using material derivatives:

$$\rho \frac{\mathrm{d}M}{\mathrm{d}t} = -\frac{\partial q_M^j}{\partial x_j} + Q_M. \tag{1.11}$$

By definition, a conservation law is special case of a balance law, that has zero source ($Q_M = 0$).

1.2.5 Ingredients (fundamental laws, constitutive equations and local thermodynamic equilibrium)

Fundamental laws of physics:

Conservation (balance) of mass (Lomonosov et al. 1756; Euler 1757; Lavoisier 1773):

$$\rho \frac{\mathrm{d}}{\mathrm{d}t}\left(\frac{1}{\rho}\right) - \frac{\partial v_j}{\partial x_j} = 0 \tag{1.12}$$

Conservation (balance) of linear momentum (Newton 1687; Euler 1757):

$$\rho \frac{\mathrm{d}v_i}{\mathrm{d}t} + \frac{\partial q_p^{ij}}{\partial x_j} = 0 \tag{1.13}$$

Conservation (balance) of angular momentum (Newton 1687; Cauchy 1827):

$$\rho \frac{\mathrm{d}\epsilon_{ijk} r_j v_k}{\mathrm{d}t} + \frac{\partial q_L^{ij}}{\partial x_j} = 0 \tag{1.14}$$

Conservation (balance) of total energy (Joule 1843, 1850):

$$\rho \frac{\mathrm{d}E}{\mathrm{d}t} + \frac{\partial q_E^j}{\partial x_j} = 0 \tag{1.15}$$

Balance of entropy and the second law of thermodynamics (Carnot, 1824; Clausius, 1854) :

$$\rho \frac{\mathrm{d}S}{\mathrm{d}t} + \frac{\partial q_S^j}{\partial x_j} = Q_s \geq 0 \tag{1.16}$$

Constitutive equations

Unlike the fundamental laws, that are valid regardless of model assumptions, for any material, the fluxes of the conserved quantities can vary based on model assumptions. E.g. a different stress-strain relationship is needed for viscous and plastic deformation. These different behaviours of matter are described by the constitutive equations. Also, the constitutive equations are usually involve some material properties, that is essential to include in the model to have good predictive power for the considered material.

Fourier's law of heat conduction Fourier (1822):

$$q_{\mathrm{Heat}}^j = -\lambda \frac{\partial T}{\partial x_j}. \tag{1.17}$$

Flow of viscous fluids (final form by Stokes, 1845) :

$$q_m^{ij} = \sigma_{ij} + \delta_{ij} \int_0^{x_j} \rho g_i dx_j \tag{1.18}$$

$$\sigma_{ij} = -\delta_{ij} P + 2\eta \left(\frac{1}{2} \left(\frac{\partial v_i}{\partial x_j} + \frac{\partial v_j}{\partial x_i} \right) - \frac{1}{3} \delta_{ij} \frac{\partial v_k}{\partial x_k} \right), \tag{1.19}$$

where $\Phi = f(x_j)$ is the gravity potential.

Equation of state :

$$P = f(T, \rho) \text{ or } T = f(P, \rho) \text{ or } \rho = f(P, T) \tag{1.20}$$

Local Thermodynamic Equilibrium (LTE)

The fundamental laws of thermodynamics and the equations of state, were originally formulated for closed systems, in equilibrium (pressure, temperature and composition - i.e. stable phases - are uniform). The framework of classical irreversible thermodynamics is the established way to quantify non-equilibrium processes, such as thermal conduction, chemical diffusion or combustion dynamics (e.g. De Groot and Mazur, 1984; Müller and Müller, 2009). This framework has been successfully applied to design many devices that operate far from equilibrium, such as internal combustion engines or rocket nozzles. The key assumption of LTE is that, even in systems that are not in global equilibrium, every infinitesimal material point is in thermodynamic equilibrium locally and in every instant of time. This allows us to use equilibrium-relationships in open systems, that are not in equilibrium. One of these equilibrium concepts is the so-called fundamental thermodynamic relationship, that says that the internal energy can be partitioned into different forms, in this case as heat, gravitational potential energy or volumetric work:

$$\mathrm{d}U = -g_j \mathrm{d}x_j(t) + T\mathrm{d}S - P\mathrm{d}V, \tag{1.21}$$

where $x_j(t)$ denotes the path of a material point. The exact terms we consider here are always model specific, hence this relationship is an axiom that defines what type of a thermodynamic system we consider (e.g. for an elastic model we should consider elastic strain energy). The LTE says that this relationship is satisfied instantaneously, thus we can write this relationship in terms of time increments

$$\frac{\mathrm{d}U}{\mathrm{d}t} = -g_j \frac{\mathrm{d}x_j(t)}{\mathrm{d}t} + T\frac{\mathrm{d}S}{\mathrm{d}t} - P\frac{\mathrm{d}V}{\mathrm{d}t}. \tag{1.22}$$

Finally, let us reformulate the fundamental thermodynamic relationship in terms of total energy, so we can later relate it to the conservation of energy, using $E_{\text{tot}} = U + E_{\text{kin}}$

$$\frac{\mathrm{d}E}{\mathrm{d}t} = \frac{\mathrm{d}}{\mathrm{d}t}\left(\frac{v_i v_i}{2}\right) - g_j v_j + T\frac{\mathrm{d}S}{\mathrm{d}t} - P\frac{\mathrm{d}V}{\mathrm{d}t}. \tag{1.23}$$

Variable	**symbol**	**units (SI)**
spatial coordinates	x_j	m
time	t	s
mass	m	kg
temperature	T	K
pressure	P	Pa
specific volume	V, ρ^{-1}	$\mathrm{m^3kg^{-1}}$
specific energy	E	$\mathrm{J.kg^{-1}}$
specific entropy	S	$\mathrm{J.K^{-1}.kg^{-1}}$
density	ρ	$\mathrm{kg.m^{-3}}$
velocity	v_j	$\mathrm{m.s^{-1}}$
non-advective momentum flux	q_p^{ij}	Pa
non-advective energy flux	q_E^j	$\mathrm{W.m^{-2}}$
non-advective entropy flux	q_E^j	$\mathrm{W.K^{-1}.m^{-2}}$
specific entropy production	Q_S	$\mathrm{J.K^{-1}.kg^{-1}s^{-1}}$
gravitational acceleration	g_j	$\mathrm{m.s^{-2}}$
total stress	σ_{ij}	Pa
deviatoric stress	τ_{ij}	Pa
thermal conductivity	λ	$\mathrm{W.m^{-1}K^{-1}}$
viscosity	η	Pa.s
total strain rate	$\dot{\epsilon}_{ij}$	$\mathrm{s^{-1}}$
symmetric, deviatoric strain rate	$\dot{\epsilon}^{ij}_{\mathrm{sym}}$	$\mathrm{s^{-1}}$
antisymmetric, deviatoric strain rate	$\dot{\epsilon}^{ij}_{\mathrm{asym}}$	$\mathrm{s^{-1}}$
volumetric strain rate	$\dot{\epsilon}^{ij}_{\mathrm{vol}}$	$\mathrm{s^{-1}}$
thermal expansion coefficient	α	$\mathrm{K^{-1}}$
compressibility	β	$\mathrm{Pa^{-1}}$
specific heat capacity at const. P	C_P	$\mathrm{J.K^{-1}kg^{-1}}$
Kronecker delta	δ_{ij}	-
Levi-Civita symbol	ϵ_{ijk}	-

1.2.6 Recipe for viscous flow, with gravity

Step 1 - Write a system of equations using the balance laws

$$\rho \frac{\mathrm{d}}{\mathrm{d}t}\left(\frac{1}{\rho}\right) = \frac{\partial v_j}{\partial x_j} \tag{1.24}$$

$$\rho \frac{\mathrm{d}v_i}{\mathrm{d}t} = -\frac{\partial q_p^{ij}}{\partial x_j} \tag{1.25}$$

$$\rho \frac{\mathrm{d}E}{\mathrm{d}t} = -\frac{\partial q_E^{j}}{\partial x_j} \tag{1.26}$$

$$\rho \frac{\mathrm{d}S}{\mathrm{d}t} = -\frac{\partial q_S^{j}}{\partial x_j} + Q_S \tag{1.27}$$

(For conservation of angular momentum see section 1.2.7)

Step 2 - Write the LTE specific to the model and bring it into a convenient form

$$\frac{\mathrm{d}E}{\mathrm{d}t} = T\frac{\mathrm{d}S}{\mathrm{d}t} - P\frac{\mathrm{d}V}{\mathrm{d}t} + \frac{\mathrm{d}}{\mathrm{d}t}\left(\frac{1}{2}v_i v_i\right) - v_j g_j. \tag{1.28}$$

Let's notice, that in the $P\mathrm{d}V$ term $V = \rho^{-1}$ is the specific volume and also that the kinetic energy term can be reformulated using the chain rule. After all of these changes and multiplying by ρ we get an equation with all of the transient terms from the balance laws:

$$\rho\frac{\mathrm{d}E}{\mathrm{d}t} = T\rho\frac{\mathrm{d}S}{\mathrm{d}t} - P\rho\frac{\mathrm{d}}{\mathrm{d}t}\left(\frac{1}{\rho}\right) + v_i\rho\frac{\mathrm{d}v_i}{\mathrm{d}t} - v_j\rho g_j. \tag{1.29}$$

Step 3 - Substitute the balance laws into the time derivatives

$$-\frac{\partial q_E^{j}}{\partial x_j} = -T\frac{\partial q_S^{j}}{\partial x_j} + TQ_S - P\frac{\partial v_j}{\partial x_j} - v_i\frac{\partial q_p^{ij}}{\partial x_j} - v_j\rho g_j \tag{1.30}$$

Step 4 - Solve for TQ_S

$$TQ_S = -\frac{\partial q_E^{j}}{\partial x_j} + T\frac{\partial q_S^{j}}{\partial x_j} + P\frac{\partial v_j}{\partial x_j} + v_i\frac{\partial q_p^{ij}}{\partial x_j} + v_j\rho g_j \tag{1.31}$$

Step 5 - Cancel the potentials

Let us separate the momentum flux into parts that are related either to body forces (related to potential fields, in this case gravity) or to surface forces (stresses)

$$q_p^{ij} = -\sigma_{ij} - \delta_{ij}\int_0^{x_i} \rho g_j \mathrm{d}x_i, \tag{1.32}$$

where the negative sign of σ_{ij} is a convention. Since,

$$v_i\frac{\partial q_p^{ij}}{\partial x_j} = -v_i\frac{\partial \sigma_{ij}}{\partial x_j} - v_i\rho g_i, \tag{1.33}$$

if we substitute back to equation (1.31) we get:

$$TQ_S = -\frac{\partial q_E^j}{\partial x_j} + T\frac{\partial q_S^j}{\partial x_j} + P\frac{\partial v_j}{\partial x_j} - v_i\frac{\partial \sigma_{ij}}{\partial x_j} \tag{1.34}$$

Kronecker delta (δ_{ij}) and index notation

$$\delta_{i=j} = 1 \text{ and } \delta_{i\neq j} = 0, \text{ alternatively } \delta_{ij} = \begin{bmatrix} 1 & 0 & 0 \\ 0 & 1 & 0 \\ 0 & 0 & 1 \end{bmatrix}$$

Example:

$$\delta_{ij}\frac{\partial v_i}{\partial x_j} = \sum_i\sum_j \delta_{ij}\frac{\partial v_i}{\partial x_j} = \sum_{i=j}\sum_j 1\frac{\partial v_i}{\partial x_j} + \sum_{i\neq j}\sum_j 0\frac{\partial v_i}{\partial x_j} = \sum_j \frac{\partial v_j}{\partial x_j} = \frac{\partial v_j}{\partial x_j}.$$

Step 6 - Choose an energy flux such a way that all terms with divergences of unknown fluxes cancel

We are trying to choose fluxes, that ensure non-negative entropy production. We do not know much about the divergences of the fluxes, yet our equation is filled with these terms. Let us use the product rule ($\nabla(aq) - q\nabla a = a\nabla q$) for the terms with the momentum and entropy fluxes:

$$TQ_S = \frac{\partial}{\partial x_j}\left(-q_E^j + Tq_S^j - v_i\sigma_{ij}\right) - q_S^j\frac{\partial T}{\partial x_j} + P\frac{\partial v_j}{\partial x_j} + \sigma_{ij}\frac{\partial v_i}{\partial x_j}. \tag{1.35}$$

A particular way to cancel the divergence of the energy flux is to use

$$q_E^j = Tq_S^j - v_i\sigma_{ij}. \tag{1.36}$$

Now we are left with gradients and divergences of quantities that we can handle.

$$TQ_S = -q_S^j\frac{\partial T}{\partial x_j} + P\frac{\partial v_j}{\partial x_j} + \sigma_{ij}\frac{\partial v_i}{\partial x_j}. \tag{1.37}$$

Step 7 - Apply the second law of thermodynamics

The second law of thermodynamics (translated to our problem) says that Q_S must never be negative, so

$$TQ_S = -q_S^j\frac{\partial T}{\partial x_j} + P\frac{\partial v_j}{\partial x_j} + \sigma_{ij}\frac{\partial v_i}{\partial x_j} \geq 0, \tag{1.38}$$

since we use an absolute temperature scale.

Step 8 - Determine the remaining fluxes and make sure that $Q_S \geq 0$

The fluxes must satisfy our empirical knowledge, listed as the phenomenological laws and we must check if the proposed ones are admissible (i.e. $Q_S \geq 0$). One way to choose $Q_S \geq 0$ as some coefficient times the corresponding derivative from equation (1.38). This way we will end up with sums of squares and we only have to choose a coefficient with the

correct sign. Our motivation for the entropy flux is Fourier's law of heat conduction

$$q_S^j = -\frac{\lambda}{T}\frac{\partial T}{\partial x_j}. \tag{1.39}$$

The factor $1/T$ is necessary to satisfy Fourier's law once the heat transfer equation is derived. Heat is $T\mathrm{d}S$ at constant volume and Fourier's law describes the heat flux.

For the momentum flux we have to include that pressure differences induce fluid flow, and we have to take into account viscosity, that is a "resistance" of fluids against deformation. In other words viscous deformation is non-reversible. The most straightforward solution to make viscous dissipation never negative, would be to simply merge Bernoulli's and Newton's law and extend it into a tensor form:

$$\sigma_{ij} = -\delta_{ij}P + \eta\frac{\partial v_i}{\partial x_j}. \tag{1.40}$$

This is admissible for any non-negative η, but unfortunately it is not correct.
The strain rate tensor can be expressed as a sum of its symmetric and antisymmetric parts

$$\frac{\partial v_i}{\partial x_j} = \frac{1}{2}\left(\frac{\partial v_i}{\partial x_j} + \frac{\partial v_j}{\partial x_i}\right) + \frac{1}{2}\left(\frac{\partial v_i}{\partial x_j} - \frac{\partial v_j}{\partial x_i}\right). \tag{1.41}$$

The symmetric part can be further divided into volumetric and deviatoric parts (as the antisymmetric is already deviatoric):

$$\frac{\partial v_i}{\partial x_j} = \left\{\frac{1}{2}\left(\frac{\partial v_i}{\partial x_j} + \frac{\partial v_j}{\partial x_i}\right) - \frac{1}{3}\delta_{ij}\frac{\partial v_k}{\partial x_k}\right\} + \frac{1}{3}\delta_{ij}\frac{\partial v_k}{\partial x_k} + \frac{1}{2}\left(\frac{\partial v_i}{\partial x_j} - \frac{\partial v_j}{\partial x_i}\right), \tag{1.42}$$

The antisymmetric part of the strain rate tensor represents rigid body rotation, that should not generate viscous dissipation, as there is no internal deformation. Also, here we consider zero bulk viscosity (that is a good assumption in most cases), so we want to make sure that volumetric deformation is reversible, therefore dissipation should depend only on the symmetric, deviatoric strain rates:

$$\sigma_{ij} = -\delta_{ij}P + 2\eta\left(\frac{1}{2}\left(\frac{\partial v_i}{\partial x_j} + \frac{\partial v_j}{\partial x_i}\right) - \frac{1}{3}\delta_{ij}\frac{\partial v_k}{\partial x_k}\right). \tag{1.43}$$

The factor 2 in front of η is introduced by convention, to satisfy Newton's law in simple shear ($\tau = \eta\ \partial v_x/\partial y$), when the flow velocities are parallel everywhere and only vary in a flow-perpendicular direction.
Substituting these fluxes back into the entropy source equation (eq. 1.38), we get:

$$TQ_S = \frac{\lambda}{T}\frac{\partial T}{\partial x_j}\frac{\partial T}{\partial x_j} + P\frac{\partial v_j}{\partial x_j} + \left[-\delta_{ij}P + 2\eta\left(\frac{1}{2}\left(\frac{\partial v_i}{\partial x_j} + \frac{\partial v_j}{\partial x_i}\right) - \frac{1}{3}\delta_{ij}\frac{\partial v_k}{\partial x_k}\right)\right]\frac{\partial v_i}{\partial x_j} \geq 0. \tag{1.44}$$

We already made sure that the entropy flux is admissible. Now we take a look at the momentum flux times strain rate term. For simplicity we are going to denote the strain rate tensor as $\dot{\epsilon}_{ij}$, that can be constructed as a sum of its symmetric-deviatoric and

antisymmetric-deviatoric and volumetric parts

$$\dot{\epsilon}_{ij} = \frac{\partial v_i}{\partial x_j} = \dot{\epsilon}^{ij}_{\text{sym}} + \dot{\epsilon}^{ij}_{\text{asym}} + \dot{\epsilon}^{ij}_{\text{vol}} \tag{1.45}$$

$$\dot{\epsilon}^{ij}_{\text{sym}} = \frac{1}{2}\left(\frac{\partial v_i}{\partial x_j} + \frac{\partial v_j}{\partial x_i}\right) - \frac{1}{3}\delta_{ij}\frac{\partial v_k}{\partial x_k} \tag{1.46}$$

$$\dot{\epsilon}^{ij}_{\text{asym}} = \frac{1}{2}\left(\frac{\partial v_i}{\partial x_j} - \frac{\partial v_j}{\partial x_i}\right) \tag{1.47}$$

$$\dot{\epsilon}^{ij}_{\text{vol}} = \frac{1}{3}\delta_{ij}\frac{\partial v_k}{\partial x_k}. \tag{1.48}$$

Using this notation, the entropy production terms will be

$$TQ_S = \frac{\lambda}{T}\frac{\partial T}{\partial x_j}\frac{\partial T}{\partial x_j} + P\frac{\partial v_j}{\partial x_j} + \left(-\delta_{ij}P + 2\eta\dot{\epsilon}^{ij}_{\text{sym}}\right)\left(\dot{\epsilon}^{ij}_{\text{sym}} + \dot{\epsilon}^{ij}_{\text{asym}} + \dot{\epsilon}^{ij}_{\text{vol}}\right) \geq 0. \tag{1.49}$$

Let us consider first the term:

$$-\delta_{ij}P\left(\dot{\epsilon}^{ij}_{\text{sym}} + \dot{\epsilon}^{ij}_{\text{asym}} + \dot{\epsilon}^{ij}_{\text{vol}}\right) = -P\frac{\partial v_j}{\partial x_j}, \tag{1.50}$$

since $\delta_{ij}P$ is a diagonal tensor and $\dot{\epsilon}^{ij}_{\text{asym}}$ has zeros in its main diagonal

$$-\delta_{ij}P\dot{\epsilon}^{ij}_{\text{asym}} = 0 \tag{1.51}$$

and $\dot{\epsilon}^{ij}_{\text{sym}}$ is deviatoric, so the sum of its elements in the main diagonal is zero

$$-\delta_{ij}P\dot{\epsilon}^{ij}_{\text{sym}} = -P\left(\delta_{ij}\dot{\epsilon}^{ij}_{\text{sym}}\right) = 0. \tag{1.52}$$

and finally

$$-\delta_{ij}P\dot{\epsilon}^{ij}_{\text{vol}} = -P\left(\delta_{ij}\dot{\epsilon}^{ij}_{\text{vol}}\right) = -P\frac{\partial v_j}{\partial x_j}. \tag{1.53}$$

Now let us consider the second term:

$$2\eta\dot{\epsilon}^{ij}_{\text{sym}}\left(\dot{\epsilon}^{ij}_{\text{sym}} + \dot{\epsilon}^{ij}_{\text{asym}} + \dot{\epsilon}^{ij}_{\text{vol}}\right) = 2\eta\dot{\epsilon}^{ij}_{\text{sym}}\dot{\epsilon}^{ij}_{\text{sym}}. \tag{1.54}$$

Let us notice that the product of a symmetric and an antisymmetric tensor is always antisymmetric, and the sum of the elements of an antisymmetric tensor is always zero

$$2\eta\dot{\epsilon}^{ij}_{\text{sym}}\dot{\epsilon}^{ij}_{\text{asym}} = 0. \tag{1.55}$$

The volumetric strain rate tensor is a diagonal tensor and the sum of the diagonal elements of the symmetric-deviatoric tensor is zero:

$$2\eta\dot{\epsilon}^{ij}_{\text{sym}}\dot{\epsilon}^{ij}_{\text{vol}} = \eta\dot{\epsilon}^{ij}_{\text{sym}}\frac{2}{3}\delta_{ij}\frac{\partial v_k}{\partial x_k} = \eta(\delta_{ij}\dot{\epsilon}^{ij}_{\text{sym}})\frac{2}{3}\frac{\partial v_k}{\partial x_k} = 0. \tag{1.56}$$

Now we can write a simplified form of the entropy source equation (1.49):

$$TQ_S = \frac{\lambda}{T}\frac{\partial T}{\partial x_j}\frac{\partial T}{\partial x_j} + P\frac{\partial v_j}{\partial x_j} - P\frac{\partial v_j}{\partial x_j} + 2\eta\dot{\epsilon}^{ij}_{\mathrm{sym}}\dot{\epsilon}^{ij}_{\mathrm{sym}} \geq 0, \tag{1.57}$$

and simplifying further

$$TQ_S = \frac{\lambda}{T}\frac{\partial T}{\partial x_j}\frac{\partial T}{\partial x_j} + 2\eta\dot{\epsilon}^{ij}_{\mathrm{sym}}\dot{\epsilon}^{ij}_{\mathrm{sym}} \geq 0. \tag{1.58}$$

With all the previous steps we also ensured positive entropy production and we could make sure that we only get viscous dissipation by non-volumetric internal deformation.
Note: In this case $\tau_{ij} = 2\eta\dot{\epsilon}^{ij}_{\mathrm{sym}}$.

Step 9 - Substitute back fluxes and sources into the balance equations

$$\rho\frac{\mathrm{d}}{\mathrm{d}t}\left(\frac{1}{\rho}\right) = \frac{\partial v_j}{\partial x_j} \tag{1.59}$$

$$\rho\frac{\mathrm{d}v_i}{\mathrm{d}t} = -\frac{\partial}{\partial x_j}\left(\delta_{ij}P - 2\eta\dot{\epsilon}^{ij}_{\mathrm{sym}} - \delta_{ij}\int_0^{x_i}\rho g_j \mathrm{d}x_i\right) \tag{1.60}$$

$$\rho\frac{\mathrm{d}E}{\mathrm{d}t} = -\frac{\partial}{\partial x_j}\left(-\lambda\frac{\partial T}{\partial x_j} - v_i\sigma_{ij}\right) \tag{1.61}$$

$$\rho\frac{\mathrm{d}S}{\mathrm{d}t} = -\frac{\partial}{\partial x_j}\left(-\frac{\lambda}{T}\frac{\partial T}{\partial x_j}\right) + \frac{\lambda}{T^2}\frac{\partial T}{\partial x_j}\frac{\partial T}{\partial x_j} + \frac{\tau_{ij}\dot{\epsilon}^{ij}_{\mathrm{sym}}}{T} = -\frac{1}{T}\frac{\partial}{\partial x_j}\left(-\lambda\frac{\partial T}{\partial x_j}\right) + \frac{\tau_{ij}\dot{\epsilon}^{ij}_{\mathrm{sym}}}{T} \tag{1.62}$$

So far we made sure to obey the fundamental laws of nature (conservation of mass, momentum and energy, plus non-negative entropy production), and we made no other assumptions than the LTE. If we count v_i as one unknown, we have four equations for six unknowns (ρ, v_i, P, E, T, S). This is not a closed system of equations, to get one we need two more equations. Here we are going to use equations of state to close the system, but an ultimately correct way would be to know exactly $T(\rho, U \text{ or } S)$ and $P(\rho, U \text{ or } S)$ (i.e. thermodynamic look-up table).

Step 10 - Close the system of equations with the suitable Equations of State (EoS)

We do not have equations for P and T, so let us formulate $\mathrm{d}S$ and $\mathrm{d}V$ in a more convenient way, as a function of T and P:

$$\mathrm{d}S = \left(\frac{\partial S}{\partial T}\right)_P \mathrm{d}T + \left(\frac{\partial S}{\partial P}\right)_T \mathrm{d}P \tag{1.63}$$

$$\mathrm{d}V = \left(\frac{\partial V}{\partial T}\right)_P \mathrm{d}T + \left(\frac{\partial V}{\partial P}\right)_T \mathrm{d}P \tag{1.64}$$

Now we have two extra equations, and three of these derivatives are actually the definitions

of three material properties, that can be measured and found in the literature:

$$C_P = \left(\frac{\partial Q}{\partial T}\right)_P = \left(\frac{\partial U}{\partial T}\right)_P = T\left(\frac{\partial S}{\partial T}\right)_P \tag{1.65}$$

$$\alpha = \frac{1}{V}\left(\frac{\partial V}{\partial T}\right)_P \tag{1.66}$$

$$\beta = -\frac{1}{V}\left(\frac{\partial V}{\partial P}\right)_T \tag{1.67}$$

On the use of specific and total quantities

We use S and V as specific quantities (per unit mass), although in classical thermodynamics the parameters α and β are usually expressed in terms of total volume ($V_{\text{tot}} = mV$). However, since these parameters are measured in closed system experiments, the mass is constant, thus α and β are the same both in total and specific volumes, e.g.:

$$\alpha = \frac{1}{V_{\text{tot}}}\left(\frac{\partial V_{\text{tot}}}{\partial T}\right)_P = \frac{1}{mV}\left(\frac{\partial mV}{\partial T}\right)_P = \frac{m}{mV}\left(\frac{\partial V}{\partial T}\right)_P = \frac{1}{V}\left(\frac{\partial V}{\partial T}\right)_P.$$

Using a similar argumentation, one can show that:

$$\frac{C_P^{\text{tot}}}{m} = \frac{T}{m}\left(\frac{\partial S_{\text{tot}}}{\partial T}\right)_P = \frac{T}{m}\left(\frac{\partial mS}{\partial T}\right)_P = \frac{mT}{m}\left(\frac{\partial S}{\partial T}\right)_P = T\left(\frac{\partial S}{\partial T}\right)_P = C_P.$$

Generally in continuum mechanics, it is better to use specific (intensive) quantities than total (extensive) quantities because mass is variable in most cases.

For the second term of equation 1.63 we can use a Maxwell relationship:

$$\left(\frac{\partial S}{\partial P}\right)_T = -\left(\frac{\partial V}{\partial T}\right)_P \tag{1.68}$$

If we substitute back to equations 1.63 and 1.65, we get (remember $V = \rho^{-1}$):

$$\frac{\mathrm{d}S}{\mathrm{d}t} = \frac{C_P}{T}\frac{\mathrm{d}T}{\mathrm{d}t} - \frac{\alpha}{\rho}\frac{\mathrm{d}P}{\mathrm{d}t} \tag{1.69}$$

$$\rho\frac{\mathrm{d}}{\mathrm{d}t}\left(\frac{1}{\rho}\right) = \alpha\frac{\mathrm{d}T}{\mathrm{d}t} - \beta\frac{\mathrm{d}P}{\mathrm{d}t} \tag{1.70}$$

Let us reorder them:

$$\rho C_P\frac{\mathrm{d}T}{\mathrm{d}t} = \alpha T\frac{\mathrm{d}P}{\mathrm{d}t} + T\rho\frac{\mathrm{d}S}{\mathrm{d}t} \tag{1.71}$$

$$\beta\frac{\mathrm{d}P}{\mathrm{d}t} = -\rho\frac{\mathrm{d}}{\mathrm{d}t}\left(\frac{1}{\rho}\right) + \alpha\frac{\mathrm{d}T}{\mathrm{d}t} \tag{1.72}$$

Now we have a closed system of equation in a convenient form. Notice, that there is a nonlinear dependence between P and T.

Step 11 - The final, self-consistent, closed system of equations

Usually, there is no need to track all the six variables:

$$\frac{1}{\rho}\frac{\mathrm{d}\rho}{\mathrm{d}t} = -\frac{\partial v_j}{\partial x_j} \tag{1.73}$$

$$\rho\frac{\mathrm{d}v_i}{\mathrm{d}t} = -\frac{\partial}{\partial x_j}\left(\delta_{ij}P - 2\eta\dot{\epsilon}^{ij}_{\mathrm{sym}} - \delta_{ij}\int_0^{x_j}\rho g_i \mathrm{d}x_j\right) \tag{1.74}$$

$$\rho\frac{\mathrm{d}E}{\mathrm{d}t} = -\frac{\partial}{\partial x_j}\left(-\lambda\frac{\partial T}{\partial x_j} - v_i\sigma_{ij}\right) \tag{1.75}$$

$$\rho\frac{\mathrm{d}S}{\mathrm{d}t} = \frac{1}{T}\frac{\partial}{\partial x_j}\left(-\lambda\frac{\partial T}{\partial x_j}\right) + \frac{\tau_{ij}\dot{\epsilon}^{ij}_{\mathrm{sym}}}{T} \tag{1.76}$$

$$\rho C_P\frac{\mathrm{d}T}{\mathrm{d}t} = \alpha T\frac{\mathrm{d}P}{\mathrm{d}t} + T\rho\frac{\mathrm{d}S}{\mathrm{d}t} \tag{1.77}$$

$$\beta\frac{\mathrm{d}P}{\mathrm{d}t} = \frac{1}{\rho}\frac{\mathrm{d}\rho}{\mathrm{d}t} + \alpha\frac{\mathrm{d}T}{\mathrm{d}t} \tag{1.78}$$

Instead we substitute the entropy term in the temperature evolution equation, plus the mass conservation into the pressure evolution equation, and solve for only ρ, P, v_i and T:

$$\frac{1}{\rho}\frac{\mathrm{d}\rho}{\mathrm{d}t} = -\frac{\partial v_j}{\partial x_j} \tag{1.79}$$

$$\rho\frac{\mathrm{d}v_i}{\mathrm{d}t} = -\frac{\partial}{\partial x_j}\left(\delta_{ij}P - 2\eta\dot{\epsilon}^{ij}_{\mathrm{sym}} - \delta_{ij}\int_0^{x_j}\rho g_i \mathrm{d}x_j\right) \tag{1.80}$$

$$\rho C_P\frac{\mathrm{d}T}{\mathrm{d}t} = \alpha T\frac{\mathrm{d}P}{\mathrm{d}t} - \frac{\partial}{\partial x_j}\left(-\lambda\frac{\partial T}{\partial x_j}\right) + \tau_{ij}\dot{\epsilon}^{ij}_{\mathrm{sym}} \tag{1.81}$$

$$\beta\frac{\mathrm{d}P}{\mathrm{d}t} = -\frac{\partial v_j}{\partial x_j} + \alpha\frac{\mathrm{d}T}{\mathrm{d}t} \tag{1.82}$$

Now we have a fully coupled thermo-mechanical model of viscous deformation.

1.2.7 Supplementary information - How angular momentum is conserved?

From mechanics of a material point we know that angular momentum is:

$$L_i = \epsilon_{ijk} r_j (mv)_k \tag{1.83}$$

Now let us take the conservation of linear momentum and take its cross product with r_j

$$\rho\epsilon_{ijk} r_j\frac{\mathrm{d}v_k}{\mathrm{d}t} + \epsilon_{ijk} r_j\frac{\partial q^{kl}_p}{\partial x_l} = 0 \tag{1.84}$$

Using the chain rule we can write:

$$\rho\left(\frac{\mathrm{d}\epsilon_{ijk} r_j v_k}{\mathrm{d}t} - \epsilon_{ijk}\frac{\mathrm{d}r_j}{\mathrm{d}t}v_k\right) + \frac{\partial\epsilon_{ijk} r_j q^{kl}_p}{\partial x_l} - \epsilon_{ijk}\frac{\partial r_j}{\partial x_l}q^{kl}_p = 0. \tag{1.85}$$

Notice that

$$\epsilon_{ijk}\frac{\mathrm{d}r_j}{\mathrm{d}t}v_k = \epsilon_{ijk} v_j v_k = 0, \tag{1.86}$$

so

$$\rho\frac{\mathrm{d}\epsilon_{ijk}r_j v_k}{\mathrm{d}t} + \frac{\partial \epsilon_{ijk} r_j q_p^{kl}}{\partial x_l} = \epsilon_{ijk}\frac{\partial r_j}{\partial x_l} q_p^{kl}. \tag{1.87}$$

Notice that the first term is the time derivative of the angular momentum, the second term looks like the divergence of the torque. By analogy to the linear momentum, we can say that

$$L_i = \epsilon_{ijk} r_j v_k \tag{1.88}$$

$$q_L^{ij} = \epsilon_{ijk} r_j q_p^{kl} \tag{1.89}$$

$$Q_L^i = \epsilon_{ijk}\frac{\partial r_j}{\partial x_l} q_p^{kl} \tag{1.90}$$

To conserve angular momentum we need zero source:

$$Q_L^i = \epsilon_{ijk}\frac{\partial r_j}{\partial x_l} q_p^{kl} = \epsilon_{ijk}\delta_{jl}\ q_p^{kl} = \epsilon_{ijk} q_p^{jk} = 0, \tag{1.91}$$

that is true if q_p^{jk} is symmetric. Since the only non-diagonal parts of q_p^{jk} come from the stress tensor (eq. 1.32), that is symmetric (eq. 1.43), the angular momentum is conserved.

1.3 Aim and structure of the thesis

The aim of this thesis is to provide some insights to the thermo-mechanics of ductile strain localization. The first aspect is to provide at least partial answers regarding the behavior of ductile shear zones spontaneously generated by thermal softening, and estimating the potential importance of such shear zones in nature. The second aspect is to investigate some thermo-mechanical processes that could control tectonic nappe formation. A special attention is paid on the application of the results for the Helvetic Nappe System, where detailed data of geometry, kinematic evolution, deformational mechanisms and thermal history is available as a constrain. For the following questions we provide either new answers or we show some new aspects:

- How the thickness of shear zones generated by thermal softening develops?
- How the temperature of shear zones generated by thermal softening develops?
- Under what conditions could shear zone form by thermal softening?
- Can shear heating result in subduction initiation?
- How tectonic nappes are detached from their original position?
- How thrust sheets are transported?
- How rootless nappes form?
- What conditions enable stacking of fold nappes and thrust sheets?

In Chapter 2 we provide a criteria for the spontaneous generation of ductile shear zones by thermal softening using thermo-mechanical numerical simulations for linear and power-law viscous flow in one-dimension (1D), 2D and 3D. We present scaling laws for the thickness and temperature of such shear zones, that require no *a priori* information about

the shear zone itself, and that is valid for 1D, 2D and 3D, in bulk pure and simple shear.

In Chapter 3 we show with numerical simulations that subduction initiation by thermal softening at a passive margin is feasible for reasonable conditions. The shear zone temperature can be estimated by the scaling formula from Chapter 2. The model results show similarities with geological data and reconstructions of subduction during closure of the Piemont-Liguria basin during the Alpine orogeny.

In Capter 4 we present results of two-dimensional numerical simulations of shortening of a passive margin, and show the detachment and horizontal transport of a thrust nappe and stacking of this thrust nappe above a fold nappe. The model results show considerable similarities to the geological data from the Helvetic nappe system in Western Switzerland.

The last chapter (Chapter 5) provides a summery of the most important results of the thesis and also provides some perspectives.

References

Bercovici, D. and Y. Ricard
2012. Mechanisms for the generation of plate tectonics by two-phase grain-damage and pinning. *Physics of the Earth and Planetary Interiors*, 202:27–55.

Burov, E., A. Watts, et al.
2006. The long-term strength of continental lithosphere:" jelly sandwich" or" crème brûlée"? *GSA today*, 16(1):4.

Carnot, S.
1824. Reflections on the motive power of fire, and on machines fitted to develop that power. *Paris: Bachelier*.

Cauchy, A.-L.
1827. De la pression ou tension dans un corps solide. *Ex. de math*, 2:42–56.

Chung, T.
1988. *Continuum mechanics*. Prentice-Hall Englewood Cliffs.

Clausius, R.
1854. Über eine veränderte form des zweiten hauptsatzes der mechanischen wärmetheorie. *Annalen der Physik*, 169(12):481–506.

De Groot, S. and P. Mazur
1984. Non-equilibrium thermodynamics dover publications. *Inc. New York*.

Euler, L.
1757. Principes généraux du mouvement des fluides. *Mémoires de l'Académie des Sciences de Berlin*, Pp. 274–315.

Fourier, J.
1822. *Theorie analytique de la chaleur, par M. Fourier*. Chez Firmin Didot, père et fils.

Joule, J. P.
1843. Xxxii. on the calorific effects of magneto-electricity, and on the mechanical value of heat. *The London, Edinburgh, and Dublin Philosophical Magazine and Journal of Science*, 23(152):263–276.

Joule, J. P.
1850. Iii. on the mechanical equivalent of heat. *Philosophical Transactions of the royal Society of London*, (140):61–82.

Lavoisier, A.
1773. Recherches de m. priestly sur les differentes especes d'air. *Opuscules Physiques et Chimiques*.

Lomonosov, M. V., H. M. Leicester, et al.
1970. Mikhail vasil'evich lomonosov on the corpuscular theory.

Müller, I. and W. H. Müller
2009. *Fundamentals of thermodynamics and applications: with historical annotations and many citations from Avogadro to Zermelo*. Springer Science & Business Media.

Newton, I.
1999. *The Principia: mathematical principles of natural philosophy*. Univ of California Press.

Poirier, J.
1980. Shear localization and shear instability in materials in the ductile field. *Journal of Structural Geology*, 2(1-2):135–142.

Regenauer-Lieb, K., D. A. Yuen, and J. Branlund
2001. The initiation of subduction: criticality by addition of water? *Science*, 294(5542):578–580.

Stokes, G. G.
1845. On the theories of the internal friction of fluids in motion. *Transactions of the Cambridge Philosophical Society*, 8:287–305.

Thielmann, M. and B. J. Kaus
2012. Shear heating induced lithospheric-scale localization: Does it result in subduction? *Earth and Planetary Science Letters*, 359:1–13.

CHAPTER 2

Spontaneous generation of ductile shear zones by thermal softening: localization criterion, 1D to 3D modelling and application to the lithosphere

Dániel Kiss, Yuri Podladchikov, Thibault Duretz
and Stefan M. Schmalholz

Published in *Earth and Planetary Science Letters*, 519 (2019) p. 284-296

Abstract

The generation of ductile shear zones is essential for the formation of tectonic plate boundaries, such as subduction or strike-slip zones. However, the primary mechanism of ductile strain localization is still contentious. We study here the spontaneous generation of ductile shear zones by thermal softening using thermo-mechanical numerical simulations for linear and power-law viscous flow in one-dimension (1D), 2D and 3D. All models are velocity-driven. The 1D model exhibits bulk simple shear whereas the 2D and 3D models exhibit bulk pure shear. The initial conditions include a small temperature perturbation in otherwise homogeneous material. We use a series of 1D simulations to determine a new analytical formula which predicts the temperature evolution inside the shear zone. This temperature prediction requires knowledge of only the boundary velocity, flow law and thermal parameters, but no *a priori* information about the shear zone itself, such as thickness, stress and strain rate. The prediction is valid for 1D, 2D and 3D shear zones in bulk pure and simple shear. The results show that shear heating dominates over conductive cooling if the relative temperature increase is > 50 °C. The temperature variation induced by the shear zone is nearly one order of magnitude wider than the corresponding finite strain variation so that no significant temperature variation occurs between shear zone and wall rock. Applying typical flow laws for lithospheric rocks shows that shear zone generation by thermal softening occurs for typical plate tectonic velocities of few cm.yr^{-1} or strain rates between 10^{-16} and 10^{-14} s^{-1}. Shear stresses larger than 200 MPa can already cause strain localization. The results indicate that thermal softening is a feasible mechanism for spontaneous ductile shear zone generation in the lithosphere and may be one of the primary mechanisms of lithospheric strain localization.

2.1 Introduction

The spontaneous generation of shear zones in ductile rocks is fundamental for the formation of tectonic plate boundaries, such as subduction and strike slip zones, or the generation of tectonic nappes during orogenic wedge formation. We refer here to spontaneous generation of a shear zone when the fundamental shear zone parameters, such as thickness, shear stress and strain rate, are not *a priori* prescribed by the natural or model configuration. We refer to ductile deformation when the deformation behaviour is described mathematically by a relation between stress and strain rate, such as by flow laws for diffusion, dislocation or Peierls creep (i.e. low temperature plasticity). The conversion of dissipative work into heat, the related local temperature increase and the associated decrease of temperature dependent rock viscosities has frequently been suggested as a cause of spontaneous strain localization and shear zone formation in the lithosphere (Yuen et al., 1978; Regenauer-Lieb and Yuen, 1998; Leloup et al., 1999; Kaus and Podladchikov, 2006; Takeuchi and Fialko, 2012; Thielmann and Kaus, 2012; Duretz et al., 2015; Jaquet et al., 2015; Moore and Parsons, 2015). We refer here to this thermally controlled strain localization mechanism as thermal softening. Despite its fundamental thermo-mechanical feasibility (Hersey, 1936; Brinkman, 1951; Gruntfest, 1963), shear heating and thermal softening is still contentious

as important softening mechanism causing strain localization in ductile rock (Regenauer-Lieb et al., 2001; Platt and Behr, 2011; Bercovici and Ricard, 2012; Ghazian and Buiter, 2013; Gueydan et al., 2014; Platt, 2015). This is, for example, different from physics-based models of friction in rock where essentially all potential processes causing significant friction weakening are considered to be related to shear heating, such as "flash heating", thermal pressurization or temperature controlled chemical/phase changes, including melting and formation of pseudotachylites (Sibson, 1975; Fialko and Khazan, 2005; Brown and Fialko, 2012; Aharonov and Scholz, 2018). For ductile strain localization, proposed alternative mechanisms not related to shear heating are, for example, grain size reduction (Bercovici and Ricard, 2012; Platt, 2015), reaction-weakening caused by infiltration of fluids along precursor brittle faults (White and Knipe, 1978; Mancktelow and Pennacchioni, 2005) or fabric development in rock with significant mechanical heterogeneities (Montési, 2013). Out of the different mechanisms proposed for ductile strain localization, shear heating and thermal softening (1) must occur in nature since dissipative deformation generates heat and rock viscosity is temperature dependent and (2) requires the least assumptions since no knowledge concerning grain size reduction and growth, fluid flow, reaction kinetics or mechanical heterogeneities required for fabric evolution is needed. Hence, thermal softening as mechanism itself is actually not contentious, but whether thermal softening alone can be significant enough to generate shear zones in ductile rock under natural conditions is debated, as well as its relative importance compared to other localization mechanisms.

A long-lived argument against the significance of thermal softening during ductile deformation in the lithosphere is that many natural shear zones with thickness ranging from hundreds of meters to several kilometers do not indicate a sharp change in temperature between the little-deformed wall rock and the highly-deformed shear zone. This argument persists, despite the fact that several thermo-mechanical studies have shown that even if a shear zone is caused by thermal softening, there are only small temperature gradients between the shear zone and the wall rock (e.g., Yuen et al. 1978; Takeuchi and Fialko 2012; Schmalholz and Duretz 2015; Mako and Caddick 2018). Another argument against the importance of thermal softening is that the required shear stresses or the required strain rates are too large for typical lithospheric deformation conditions (e.g. Platt, 2015).

To test the validity of the above arguments against thermal softening and to quantify thermal softening, we use a thermo-mechanical numerical model of ductile rock deformation based on the conservation equations of continuum mechanics and apply constitutive equations for ductile creep. We perform a scaling analysis with results of a one-dimensional (1D) model for which simple shearing is controlled by a boundary velocity and strain localization can be triggered by a temperature, hence viscosity, perturbation in the model center. We apply a temperature perturbation because such perturbation diffuses away if shear heating is not efficient. In contrast, a viscosity perturbation (i.e. perturbation of material properties) would remain even if shear heating is insufficient and would, hence, always generate a shear zone in the 1D model, with a thickness of the initial viscosity perturbation. The model configuration is based on the model of Yuen et al. (1978) because for this configuration "No a priori assumption about slip-zone width or shear-stress magnitude

Lithology	A [$\mathrm{Pa}^{-(n+r)}\mathrm{s}^{-1}$]	n	f_{H_2O} [Pa]	r	A_{eff} [$\mathrm{Pa}^{-n}\mathrm{s}^{-1}$]	Q [$\mathrm{J.mol}^{-1}$]	λ [$\mathrm{W.K}^{-1}.\mathrm{m}^{-1}$]	ρ [$\mathrm{kg.m}^{-3}$]
Wet quartzite[1]	6.31×10^{-42}	4.0	3.7×10^{7}	1	2.91×10^{-32}	1.35×10^{5}	2.5	2700
Westerly granite[2]	3.17×10^{-26}	3.3	-	0	1.67×10^{-24}	1.87×10^{5}	2.5	2700
Wet albite[3]	2.51×10^{-15}	3.0	-	0	9.04×10^{-14}	3.32×10^{5}	2.2	2900
Wet anorthite[3]	3.98×10^{-16}	3.0	-	0	1.43×10^{-14}	3.56×10^{5}	2.2	2900
Dry anorthite[3]	5.01×10^{-6}	3.0	-	0	1.80×10^{-4}	6.56×10^{5}	2.2	2900
Wet olivine[4]	5.68×10^{-27}	3.5	10^{9}	1.2	2.40×10^{-14}	4.80×10^{5}	3.0	3400
Dry olivine[4]	1.10×10^{-16}	3.5	-	0	7.37×10^{-15}	5.30×10^{5}	3.0	3400

Table 2.1 – Rheological and thermal parameters for the used lithologies. $A_{\mathrm{eff}} = FAf_{\mathrm{H_2O}}^{r}d^{-p}$ is an effective pre-exponential factor ('A' in the main text) that incorporates grain size (d) and water fugacity ($f_{\mathrm{H_2O}}$) dependence. In all cases we use dislocation creep therefore the grain size exponent is $p = 0$. All of these flow laws describe stress and strain rate relationship in uniaxial compression experiments. In order to convert them into strain rate dependent invariant forms we need to introduce a geometry factor, which is $F = 2^{n-1}3^{(n+1)/2}$ for all presented cases (see e.g. Gerya 2009). The rest of the parameters are: power law exponent (n), water fugacity exponent (r), activation energy (Q), thermal conductivity (λ), density (ρ) and finally heat capacity is constant for all (c_p = 1050 $\mathrm{J.kg}^{-1}\mathrm{K}^{-1}$). The sources of the rheological parameters are: [1]Hirth et al. 2001, [2]Carter and Tsenn 1987, [3]Rybacki and Dresen 2004,[4]Hirth and Kohlstedt 2003.

is necessary; the thermal-mechanical structure of the slip zone evolves in time and all its characteristics are self consistently determined" (Yuen et al., 1978). These model features are essential to study spontaneous generation of shear zones in a homogeneous material. Yuen et al. (1978) considered linear viscous flow laws only whereas we also consider power-law viscous flow laws to apply our results to lithospheric dislocation creep flow laws which exhibit power-law stress exponents typically between 3 and 4 (Table 1).

The aims of our study are to (1) quantify the temperature increase required for spontaneous shear zone generation, (2) quantify the relation between the width of the temperature variation across the shear zone and the width of the corresponding finite strain variation, (3) quantify stresses, velocities and strain rates required for shear zone generation, (4) derive an analytical formula which predicts the temperature inside a shear zone without *a priori* knowledge of the thickness, stress and strain rate of the shear zone, (5) compare the 1D model for bulk simple shear with 2D and 3D models for bulk pure shear and (6) evaluate the importance of thermal softening for ductile strain localization in the lithosphere.

2.2 Mathematical and numerical model

2.2.1 Governing system of equations

We assume incompressible viscous deformation in the absence of gravity and inertial forces. The governing system of equations is

$$\frac{\partial v_i}{\partial x_i} = 0 \tag{2.1}$$

$$-\delta_{ij}\frac{\partial P}{\partial x_i} + \frac{\partial \tau_{ij}}{\partial x_j} = 0 \tag{2.2}$$

$$\rho c_p \frac{\partial T}{\partial t} - \frac{\partial}{\partial x_i}\left(\lambda \frac{\partial T}{\partial x_i}\right) - \tau_{ij}\dot{\epsilon}_{ij} = 0 \tag{2.3}$$

$$\tau_{ij} = 2\mu_{\text{eff}}\dot{\epsilon}_{ij} \tag{2.4}$$

$$\mu_{\text{eff}}(\dot{\epsilon}_{\text{II}}, T) = A^{-\frac{1}{n}}\, \dot{\epsilon}_{\text{II}}^{\frac{1}{n}-1} \exp\left(\frac{Q}{nRT}\right) \tag{2.5}$$

where equation (2.1), (2.2) and (2.3) are the equations for conservation of mass, linear momentum and energy, respectively, equation (2.4) is the creep flow law (constitutive equation) and equation (2.5) states the effective viscosity. The indices i and j correspond to coordinate axes 1, 2 and 3 and repeated indices imply summation. In equation (2.3) we assume that all dissipative work is converted to heat (so-called Taylor-Quinney coefficient is 1.0) since we do not consider grain size reduction which consumes typically only a minor fraction of the dissipative work (Herwegh et al., 2014; Thielmann et al., 2015). x_i are the components of the spatial coordinates [m], t is the time [s], v_i are components of the velocity vector [m.s^{-1}], δ_{ij} is the Kronecker delta, τ_{ij} are components of the deviatoric stress tensor [Pa], ρ is density [kg.m^{-3}], c_p is heat capacity at constant pressure [J.K^{-1}], T is temperature [K], λ is thermal conductivity [W.K^{-1}.m^{-1}], μ_{eff} is effective viscosity [Pa.s], $\dot{\epsilon}_{ij}$ are components of the deviatoric strain rate tensor [s^{-1}], $\dot{\epsilon}_{\text{II}}$ is the square root of the second invariant of the strain rate tensor [s^{-1}], n is the power law exponent [ ], A is the pre-exponential factor [Pa^n.s^{-1}], Q is activation energy [J.mol^{-1}] and R is the universal gas constant [J.mol^{-1}.K^{-1}].

Initial and boundary conditions are

$$T(\sqrt{x_i x_i} > r, t = 0) = T_0 \quad \text{and} \quad T(\sqrt{x_i x_i} \leq r, t = 0) = T_0 + \Delta T_0 \tag{2.6}$$

$$q_i(x_i = [0 \text{ or } L_i], t) = 0 \tag{2.7}$$

$$v_i(x_j = 0, t) = 0 \quad \text{and} \quad v_i(x_j = L_j, t) = \Delta v_i \tag{2.8}$$

where T_0 is initial temperature [K], ΔT_0 is the value of the intial temperature perturbation [K], q_i are components of the heat flux vector [W.m^{-2}], L_i is the total size of the model domain [m] in the different spatial directions and Δv_i is the far-field velocity difference [m.s^{-1}] in the different spatial directions. The material parameters are homogenous and the initial temperature is constant except a small temperature perturbation, ΔT_0, in a

region around the model center, $x_i = 0$, whose size is specified with radius r (eq. 2.6, Fig. 2.1). This thermal perturbation mimics any kind of small variation of strength or thermal properties which are always present in natural rocks. The model is thermally insulated (eq. 2.7). For simple shear type deformation the model is kinematically driven by constant far-field boundary velocities (eq. 2.8). For pure shear type deformation in 2D and 3D only velocities normal to the boundaries are defined (i.e. $i = j$ for eq. 2.8), otherwise free slip boundary conditions are used, so shear stresses are zero at the boundaries.

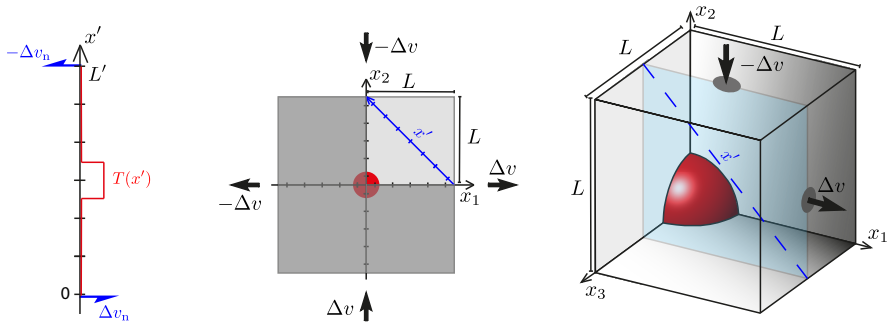

Figure 2.1 – Model configurations for 1D simple shear, and 2D and 3D pure shear bulk deformation. In all models a thermal perturbation (red) is in the model center. Due to the symmetry of the problem we solve the 2D and 3D models only for the positive coordinate region. To compare 1D results with 2D and 3D results, the results of the 1D model are rotated so that they correspond to the direction x′ in the 2D and 3D models which is orthogonal to the shear zone.

2.2.2 Numerical method

The system of non-linear equations (Eq. 2.1-2.5) is discretized on a regular Cartesian staggered grid. The problem is solved by a pseudo-transient iteration or relaxation scheme (Versteeg and Malalasekra, 2007; Duretz et al., 2019). The thermo-mechanical equations are recasted in the following form:

$$\begin{aligned}
\frac{\mathrm{d}P}{\mathrm{d}\omega} &= \frac{\partial v_i}{\partial x_i}, \\
\frac{\mathrm{d}v_i}{\mathrm{d}\omega} &= \frac{\partial \tau_{ij}}{\partial x_j} - \frac{\partial P}{\partial x_i}, \\
\frac{\mathrm{d}T}{\mathrm{d}\omega} &= \rho c_p \frac{\partial T}{\partial t} - \frac{\partial}{\partial x_i}\left(\lambda \frac{\partial T}{\partial x_i}\right) - \tau_{ij}\dot{\epsilon}_{ij}.
\end{aligned} \tag{2.9}$$

where $\frac{\mathrm{d}P}{\mathrm{d}\omega}$, $\frac{\mathrm{d}v_i}{\mathrm{d}\omega}$ and $\frac{\mathrm{d}T}{\mathrm{d}\omega}$ are derivatives of pressure, velocities and temperature with respect to pseudo time ω. We consider here incompressible deformation in the absence of inertia which corresponds to the equations when the pseudo-time derivatives have vanished. These pseudo-transient derivatives allow for an iterative solve of the non-linear system of equations. At each physical time step, an explicit integration of the non-linear equation is carried out until the pseudo time derivatives vanish and steady state is achieved. A fully implicit solution of the heat equation is obtained by evaluating the heat flux and shear heating term at each pseudo-transient iteration. The evaluation of temperature and strain rate dependent viscosity is embedded within the pseudo transient iteration cycle. The

pseudo transient algorithm is easily extendable to 2D and 3D configurations and is also well suited for vectorized parallel computations (see e.g. Omlin, 2016).

2.2.3 1D, 2D and 3D model configurations

The 1D model domain extends orthogonally across the shear zone and velocities are orthogonal to the model domain. The 1D model is driven by a velocity difference at the two model boundaries which imposes a bulk simple shear deformation (Fig. 2.1a). To test whether results of the 1D model are applicable to 2D and 3D shear zones, we perform also 2D and 3D numerical simulations for bulk pure shear. For the 3D model shortening occurs in one horizontal direction and extension in the vertical direction while the bulk extension in the second horizontal dimension is zero (Fig. 2.1c). The initial temperature perturbation has the shape of a quarter circle in the 2D model (Fig. 2.1b) and one eight of a sphere in the 3D model (Fig. 2.1c). To compare the 2D and 3D results with the 1D results we record the temperature and shear velocities along a profile line, with coordinates x', which is orthogonal to the 2D and 3D shear zones. These results are directly comparable with the results of the corresponding 1D model (Fig. 2.1).

2.3 Fundamental features of 1D shear zone evolution

There are two end-member solutions of the numerical model: (1) The velocity field converges to homogeneous simple shear in the entire model domain, there is no strain localization and the temperature increases homogeneously in the model domain due to bulk shear heating. (2) The temperature increases locally in the model center, which causes strain localization and the generation of a shear zone that is much thinner than the model domain. We show in the following fundamental features of solution (2) for representative simulations.

For simulations with linear viscosity the temperature increases in the shear zone during a transient stage and then reaches a constant temperature (Fig. 2a), in agreement with Fleitout and Froidevaux (1980). This temperature is independent on the initial temperature perturbation and model width (Fig. 2a). For simulations with power-law viscous flow laws the temperature also increases in the shear zone during a transient stage and then reaches a quasi-constant temperature (Fig. 2b). In contrast to the linear viscous model the temperature in the shear zone does not reach a strictly-constant value, but the temperature is slightly increasing with ongoing deformation, referred to here as quasi-constant (Fig. 2b). This quasi-constant temperature is also independent on the initial temperature perturbation and the model width (Fig. 2b). For such quasi-constant temperature in the shear zone center, shear heating must be locally balanced by thermal conduction (Eq. 2.3). Fleitout and Froidevaux (1980) showed that constant boundary velocities guarantee that this balance is always reached. Hence, velocity-driven shearing of a dominantly viscous medium does not lead to a thermal runaway for which temperatures would increase exponentially, in an unbounded way.

The presented model results correspond to simulations with significant shear localiza-

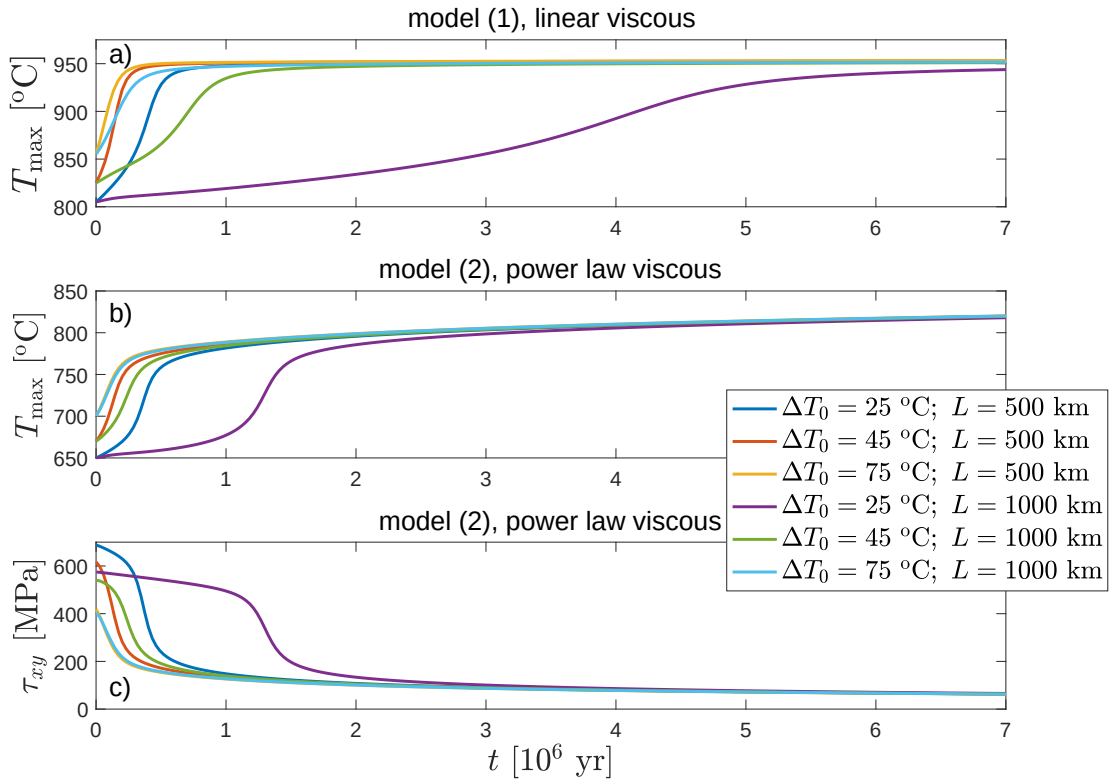

Figure 2.2 – Representative results of 1D shear zone models. Time evolution of maximum temperature at the shear zone center for linear viscous (a) and power-law viscous (b) flow. Model (1) is based on a dry anorthite diffusion creep flow law with $A_{\text{eff}} = 0.14$ Pa.s^{-1} ($d = 0.3$ mm) and $Q = 467$ kJ.mol^{-1}, model (2) is based on a dry peridotite flow law (see Table 1). In both models we applied 3 cm.yr^{-1} velocity difference. Different lines correspond to models with different model size and initial perturbation (see legend, which applies to all three panels). After a transient stage the maximum temperature converges to a constant (a) or (quasi-)constant (b) temperature. c) Shear stress evolution for power law simulations, shown in panel b). The shear stress always decreases with progressive shear zone evolution and converges to a quasi-constant value.

tion in the model center and show that a modest temperature rise of 100 °C can result in shear localization due to thermal softening (Fig. 2a and b).

The shear stress is spatially constant in the 1D model at each instant of time, it is largest at the onset of deformation and decreases with time as a result of progressive temperature increase due to shear heating (Fig. 2c). When the maximal temperature reaches a quasi-constant value then also the stress reaches a quasi-constant value.

The characteristic width of the temperature variation across the shear zone, referred to here as thermal thickness, is not prescribed *a priori* but controlled by the thermo-mechanical process (Duretz et al., 2014, 2015). After the maximal temperature has reached its (quasi-)constant value, the thermal thickness is increasing proportional with the square root of time due to thermal conduction (Fig. 3a). In the following, we distinguish between the thermal thickness and the finite strain thickness that is determined by the width of the finite strain profile (Fig. 4a). The thermal thickness is defined as the width of the temperature profile at this temperature, which is half between the maximal temperature in the shear zone center and the minimal ambient temperature far away from the shear zone (Fig. 3a). During the transient stage of temperature increase the thermal thickness

is typically decreasing (Fig. 3b). The thermal thickness evolution is essentially unaffected by the initial temperature perturbation and model size, similar to the evolution of the maximum temperature (Fig. 3b).

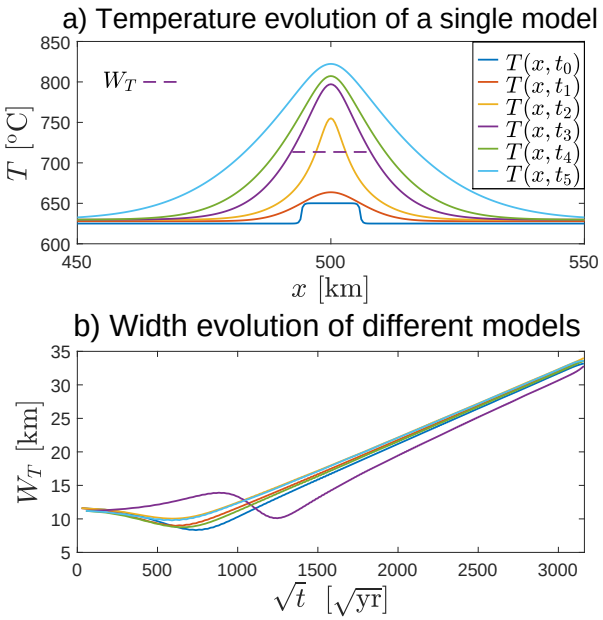

Figure 2.3 – a) Representative time evolution of a temperature profile during shear zone formation. The model setup is equivalent with the one of the ΔT_0 = 25 °C, and L = 1000 km from Fig. 2b and 2c. The dashed horizontal line indicates the thermal thickness which is measured at the temperature which is half between the maximum and minimum temperature of the corresponding profile. b) Evolution of thermal thickness for different representative simulations (same colors are used in Fig. 2b and 2c). Each line shows the result of a simulation with different initial temperature perturbation and model size. After a transient period, the thickness evolution for all simulations is linearly increasing with the square root of time.

The temperature profile is significantly wider than the corresponding finite strain (γ) profile across the shear zone (Fig. 4a), which agrees with results of Takeuchi and Fialko (2012) for strike slip zones and of Schmalholz and Duretz (2015) for thrust-type shear zones. γ is calculated by time integration of the shear strain rates. The finite strain thickness is measured in the same way as the thermal thickness, that is, the width of the γ-profile at the value of γ half between the maximum value and the far-field value at the model boundary (Fig. 4a). The ratio of thermal to finite strain thickness increases during the transient phase of temperature increase. Once the temperature has reached its (quasi-)constant value this ratio converges towards a constant value. This shows that the finite strain and thermal thickness are linked, both are controlled by thermal conduction. After the transient phase, the thermal thickness is nearly one order of magnitude (factor 6 to 8) larger than the finite strain thickness (Fig. 4b). The example presented in figure 4a shows that a significant decrease of γ from ca. 17, in the shear zone center, to 1 is associated with only a minor temperature decrease from ca. 800 °C to 760 °C (i.e. only a 20% decrease).

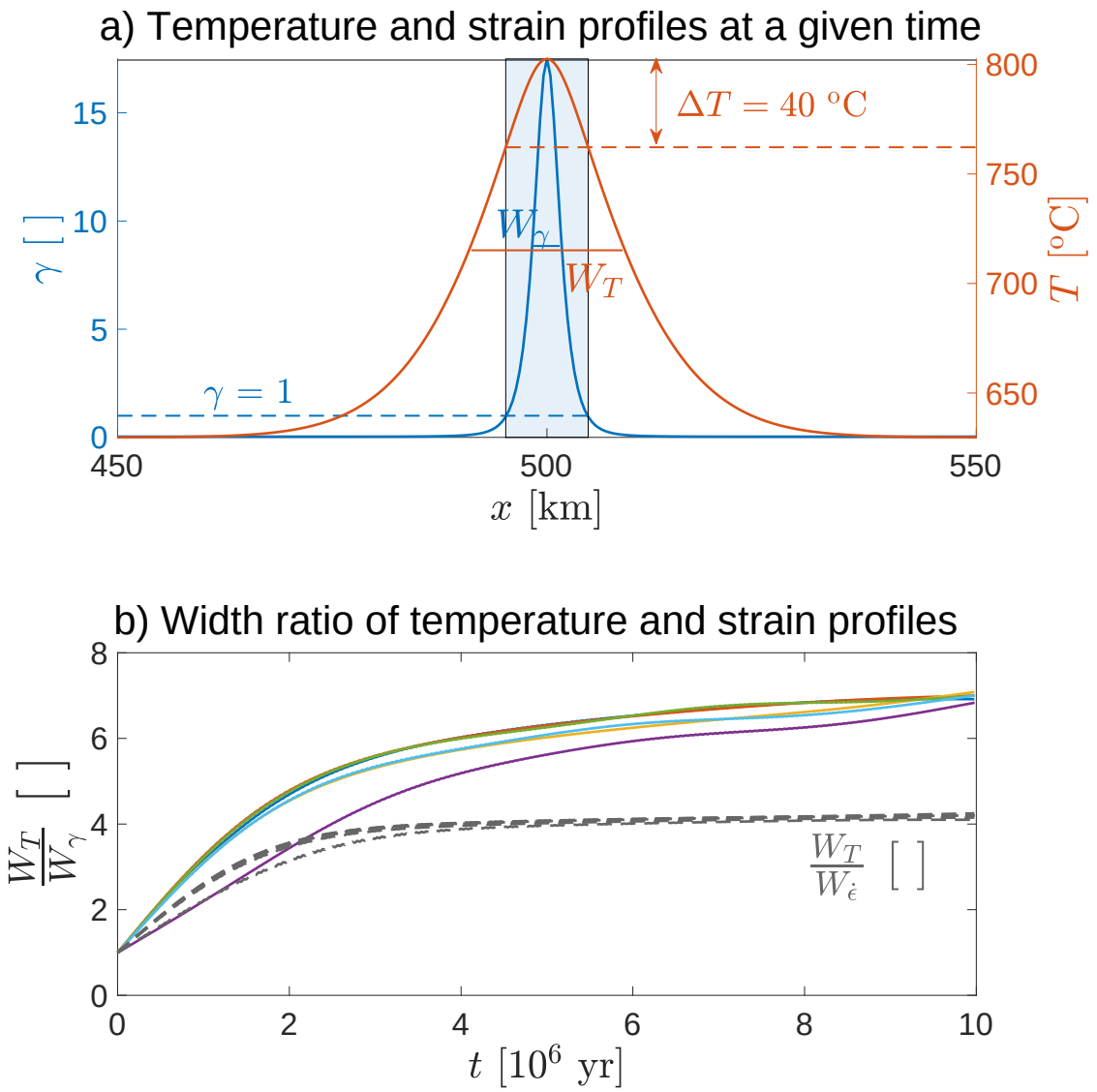

Figure 2.4 – a) Temperature and corresponding finite strain profile for a simulation with a dry olivine flow law after 3.5 Myr. The model setup is equivalent with the one of the $\Delta T_0 = 25$ °C, and L = 1000 km from Fig. 2b and 2c. The temperature profile is significantly wider than the finite strain profile. The thickness of both profiles is measured at the vertical value which is half between the maximum and minimum value of the profile. b) Evolution of the ratio of thermal thickness to corresponding finite strain thickness with progressive time for different model configurations (colors are corresponding to Fig. 2b and 2c). After a transient stage the ratios approach values between 6 and 8 showing that the temperature variation is nearly one order of magnitude wider than the corresponding finite strain variation. For comparison, also the ratio of thermal thickness to corresponding instantaneous strain rate thickness is displayed with gray dashed lines, because this thickness ratio is constant and ca. 4 for all shown simulations.

2.4 Predictive scaling relationships and localization criterion

We performed a series of 1D numerical simulations with a geologically applicable range for all independent model parameters: Δv, A, ρ, c_p, λ, T_0, n and Q. For each parameter we used several representative values which were evenly distributed within the chosen range (e.g.: n = {1, 2, 3, 5, 6}). To test the usefulness of several different sets of independent scales, we performed these simulations using the dimensional form of equations (2.4), (2.5) and (2.9). We run 1D simulations with all parameter combinations and recorded charac-

teristic parameter values (e.g.: $T_{\max}$, $\mu_{\min}$) in regular intervals during shear zone evolution. We recorded data from more than 45'000 simulation stages (i.e. at specific times) from ca. 2'000 simulations.

2.4.1 Thermal thickness of shear zones

All simulations show that shear zones are widening proportional to the square root of time (Fig. 3) and that widening is controlled by heat conduction. Two fundamental types of conductive heat transfer between shear zone and surrounding region can be distinguished: (1) If there is no significant shear heating, then the initially higher temperature in the model center is decreasing with respect to the far-field temperature during shearing and the temperature evolution in the model can be approximated with an analytical solution for Gaussian cooling of an initial Dirac delta temperature profile (Fig. 5a). The spatial and temporal evolution of temperature can then be described by the equation:

$$\Delta T(x,t) = \frac{1}{\sqrt{4\pi\kappa t}} \exp\left(-\frac{x^2}{4\kappa t}\right) \tag{2.10}$$

If the maximum temperature is in the model center, at $x = 0$, then the half width of the temperature profile is given by the value of x for which $\Delta T(x,t) = 0.5\ \Delta T_{\max}(t)$:

$$\frac{\Delta T_{\max}(t)}{2} = \frac{1}{2\sqrt{4\pi\kappa t}} = \frac{1}{\sqrt{4\pi\kappa t}} \exp\left(-\frac{x^2}{4\kappa t}\right) \rightarrow \tag{2.11}$$

$$0.5 = \exp\left(-\frac{x^2}{4\kappa t}\right) \quad \rightarrow \quad x = \sqrt{-4\ln(0.5)\kappa t} \approx 1.67\sqrt{\kappa t} \tag{2.12}$$

The corresponding full width of the Gaussian temperature profile, W_{G} is then:

$$W_{\mathrm{G}} \approx 3.34\sqrt{\kappa t} \Longleftrightarrow W_{\mathrm{G}}/\sqrt{\kappa t} \approx 3.34 \tag{2.13}$$

(2) If there is significant shear heating, then the temperature in the model center reaches a (quasi-)constant value after a transient period (Fig. 2a and b). The temperature evolution in model can then be described with a half space heating model in which the temperature is kept constant at one side, representing the shear zone center, and the far-field temperature is the initial temperature at the model boundary. The analytical solution for the temperature evolution for such scenario quantifies the heating of a half-space, representing the region adjacent to the shear zone and is given by an error function solution (Fig. 5a):

$$\Delta T(x,t) = \Delta T_{\max}\ \mathrm{erfc}\left(\frac{x}{2\sqrt{\kappa t}}\right) \tag{2.14}$$

If the maximum temperature is in the model center, at $x = 0$, then the half width of the temperature profile is given by the value of x for which $\Delta T(x,t) = 0.5\ \Delta T_{\max}(t)$:

$$\frac{\Delta T_{\max}}{2} = \Delta T_{\max}\ \mathrm{erfc}\left(\frac{x}{2\sqrt{\kappa t}}\right) \quad \rightarrow \quad 0.5 = \mathrm{erfc}\left(\frac{x}{2\sqrt{\kappa t}}\right) \tag{2.15}$$

Using the approximation erfc(0.48) ≈ 0.5 yields:

$$0.48 \approx \frac{x}{2\sqrt{\kappa t}} \quad \rightarrow \quad x \approx 0.96\sqrt{\kappa t} \tag{2.16}$$

The corresponding full width of such temperature profile, W_{E}, is then:

$$W_{\mathrm{E}} \approx 1.92\sqrt{\kappa t} \Longleftrightarrow W_{\mathrm{E}}/\sqrt{\kappa t} \approx 1.92 \tag{2.17}$$

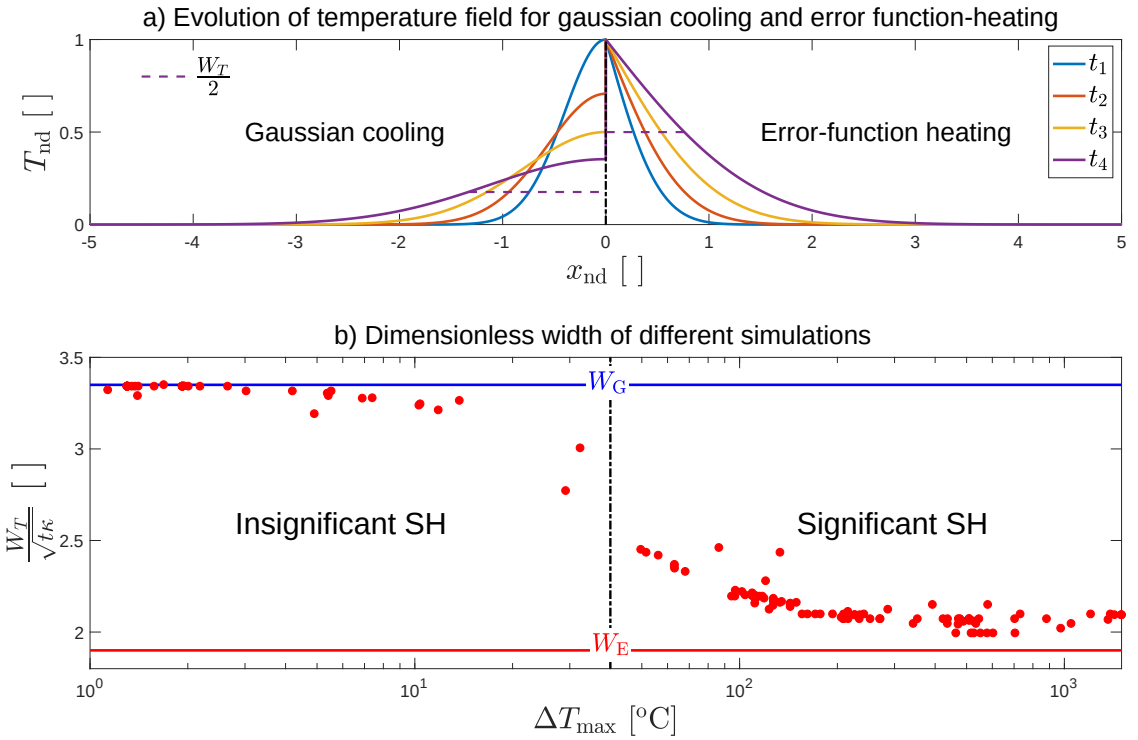

Figure 2.5 – a) Representative temperature evolution for cooling of an initial Gaussian temperature profile, left curves, and for heating for a constant temperature in the model center, right curves. Lines for t_1 to t_4 display temperature profiles at progressive times. The dashed horizontal lines indicate the half-width of a specific temperature profile. Horizontal x-coordinates and temperatures are dimensionless and temperatures have been scaled so that the initial temperature is identical. b) Plot of the dimensionless widths of temperature profiles determined from 1D numerical simulations versus the corresponding temperature increase in the shear zone center, ΔT_{max}. The blue and red horizontal lines indicate the theoretical dimensionless width for cooling of an initial Gaussian temperature profile (equation 2.13) and for heating for a constant temperature in the shear zone (equation 2.16), respectively. A value of $\Delta T_{\mathrm{max}} \approx 40$ °C indicates the transition between the two types of heat transfer and for $\Delta T_{\mathrm{max}} > 40$ °C shear heating (SH) is significant.

If thermal evolution during shearing is dominated by conductive cooling, then the width of the temperature across the shear zone will grow according to W_{G}, and according to W_{E} if thermal evolution is dominated by shear heating. We plotted the dimensionless widths, scaled by $\sqrt{\kappa t}$, of the numerically calculated temperature profiles versus the maximal temperature difference (i.e. maximum temperature in the shear zone center minus initial temperature, ΔT) recorded in the numerical simulations (Fig. 5b). For insignificant shear heating, $\Delta T <$ ca. 20 °C, the temperature profile is widening according to W_{G} (Fig. 5b). For significant shear heating, $\Delta T >$ ca. 100 °C, the temperature profile is widening

according to W_E (Fig. 5b). Between 20 and 100 °C for ΔT there is a transition zone where the thicknesses are in between W_E and W_G. The boundary between the two heat transfer domains occurs at $\Delta T \approx 40$ °C. The results, hence, indicate that a temperature increase of at least 40 °C in the shear zone is required so that shear heating dominates the heat transfer across the shear zone.

2.4.2 Maximum temperature of shear zones

After a transient phase the temperature in the shear zone is (quasi-)constant. For such quasi steady state, heat production and conduction are essentially balanced in the shear zone, that is:

$$0 \approx \rho c_p \left.\frac{\partial T}{\partial t}\right|_{x=0} = \lambda \left.\frac{\partial^2 T}{\partial x^2}\right|_{x=0} + \mu \left.\left(\frac{\partial v}{\partial x}\right)^2\right|_{x=0} . \tag{2.18}$$

For this quasi steady state, we want to determine a scaling relationship between the term representing diffusion (with λ in Eqn. 2.18) and the term representing shear heating (with μ). Such relationship can be of the form:

$$\lambda T_c \approx a\ \mu_c v_c^2 \tag{2.19}$$

where the subscripts c indicate a characteristic value of the corresponding parameter, and a is a proportionality constant. The characteristic length scale has been dropped because it has the same power in both terms for diffusion and heat production (right side of Eqn. 2.18). Because the quasi steady state occurs only in the shear zone center, it is reasonable to chose characteristic values that are representative for this location. There are several formally correct and reasonable choices for the characteristic values, but after testing the scaling relationship (2.19) with the numerical results, we found that $T_c = RT_{max}^2/Q$, $v_c = \Delta v$ and $\mu_c = \mu_{min}$ provides the best fit. T_{max} and μ_{min} are always the maximal temperature and minimum viscosity, respectively, in the shear zone center. Based on equation (2.19) and these characteristic values, T_{max} can be predicted with:

$$T_{max} \approx \frac{\Delta v}{e}\sqrt{\frac{\mu_{min} Q}{\lambda R}} \tag{2.20}$$

where $e \approx 2.72$ is the Euler number, and e^{-1} is the proportionality constant a (Fig. 6a). All parameters in this formula correspond to a specific time during shear zone evolution. Equation 2.20 is useful in applications where a shear zone viscosity (μ_{min} as a function of T_{max} and $\dot{\epsilon}_{II_{max}}$ or τ_{II}) can be constrained, for example, for rock deformation experiments. For most natural shear zones viscosities cannot be easily constrained. This is because, for example, for power-law viscous flow knowledge of the strain rate is required to determine the effective viscosity. We approximate the strain rate by the ratio of $\Delta v/\sqrt{\kappa t}$ assuming that $\sqrt{\kappa t}$ provides a representative value for the shear zone thickness. Using then the

dataset from all the 1D simulations we determine a formula to fit the shear zone viscosity:

$$\mu_{\min} \approx 1.28 \frac{e^2 \lambda Q}{\Delta v^2 n^2 R} \left[\ln \left(\frac{\Delta v^2 n R}{\lambda Q} A^{-\frac{1}{n}} \left\{ \frac{\Delta v}{\sqrt{\kappa t}} \right\}^{\frac{1}{n}-1} \right) + 1.1 \right]^{-2}. \tag{2.21}$$

For $n = 1$ the term with the approximate strain rate disappears. If we substitute the approximation of the shear zone viscosity in equation (2.20) we get:

$$T_{\max} \approx -1.13 \frac{Q}{nR} \left[\ln \left(\frac{\Delta v^2 n R}{\lambda Q} A^{-\frac{1}{n}} \left\{ \frac{\Delta v}{\sqrt{\kappa t}} \right\}^{\frac{1}{n}-1} \right) + 1.1 \right]^{-1} \tag{2.22}$$

Crosschecking with the numerical results provides the minus sign for taking the square root of $\mu_{\min}$ in Eqn. 2.20. Equation 3.1 predicts the maximum temperature in all numerically simulated shear zones with a maximal error of < 50 °C and with a root mean square error of only 20 °C (Fig. 6b). The prediction of $T_{\max}$ using equation (3.1) does not require any *a priori* knowledge of the shear zone thickness, the stress, the strain rate and the effective viscosity in the shear zone. The great advantage of equation (3.1) is, hence, that $T_{\max}$ inside a shear zone can be estimated exclusively with flow law parameters (n, A and Q), thermal parameters (λ and c_p), the density (ρ), the applied boundary velocity difference (Δv) and the duration (t) of shearing.

2.4.3 Localization criteria

A possible criterion for shear localization is that shear heating must dominate the heat transfer between shear zone and the surroundings. Based on the results discussed in the previous section we suggest $T_{\max} - T_0 > 50$ °C as localization criterion. An alternative criterion can be derived by separating the variables and the constant e in equation (2.20) and squaring both sides, which yields:

$$\frac{\Delta v^2 \mu_{\min} Q}{\lambda R T_{\max}^2} \approx e^2 \tag{2.23}$$

If the maximum temperature is replaced by the smaller initial temperature, T_0, and the minimum viscosity by the larger initial viscosity, μ_0, then a modified criterion for shear localization is:

$$Br_1 = \frac{\Delta v^2 \mu_0 Q}{\lambda R T_0^2} > e^2 \tag{2.24}$$

The dimensionless number on the left hand side is a particular version of the Brinkman number (Br_1). Several authors suggested different versions of the Brinkman number as criterion of shear localization, based on scaling analyses (e.g. Brinkman 1951; Gruntfest 1963; Yuen et al. 1978; Brun and Cobbold 1980). Another typical version of the Brinkman number (Br_2) is Br_1 divided by the Arrhenius exponent (Q/RT_0). The corresponding localization criterion is then:

$$Br_2 = \frac{\Delta v^2 \mu_0}{\lambda T_0} > 1 \tag{2.25}$$

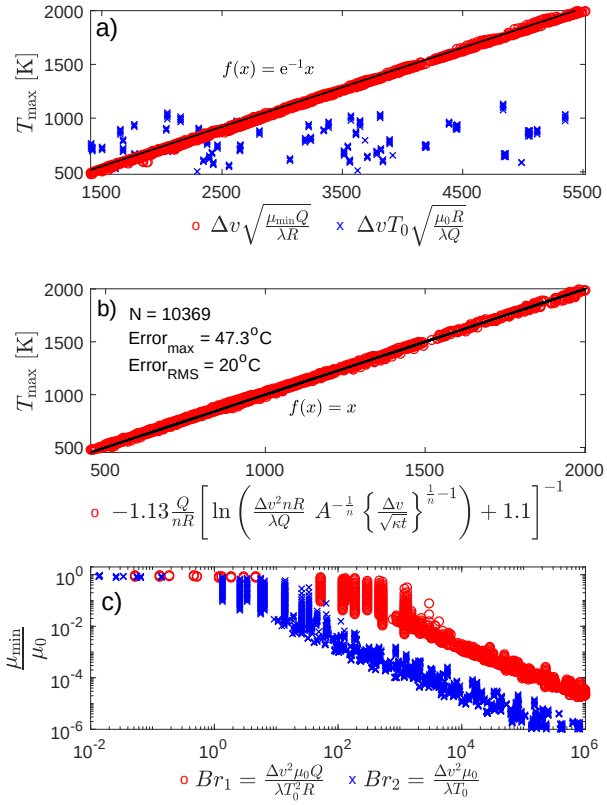

Figure 2.6 – a) Maximum temperature versus two different characteristic temperatures for all 1D simulations. Red circles represent a choice of scales which generates a data collaps and the blue crosses are an example of a scaling that generates a data scatter. The black line indicates a fit of the data (see equation in panel) where e is the Euler number. b) Maximum temperature in the shear zone from all numerical 1D simulations (T_{max}) versus the maximum temperature predicted with equation 3.1 (equation in label). c) Ratio of the minimum shear zone viscosity to the initial viscosity versus two versions of Brinkman number, Br_1 and Br_2.

We plotted the values of both Br_1 and Br_2 versus the viscosity decrease in the shear zone center (μ_{min}/μ_0) for all simulations. Both numbers are proportional to the viscosity decrease (Fig. 6c), hence they are useful criteria for strain localization. We prefer using the criterion $T_{max} - T_0 > 50$ °C due to its simplicity, or the criterion based on Br_1 because it has been directly derived from the analytical formula (eq. 2.20).

2.5 Comparison of 1D, 2D and 3D shear zones

Equations 2.20 and 3.1 for predicting the temperature in the shear zone are based on a 1D model, which is driven by far-field simple shear. We apply this prediction to shear zones that develop in 2D and 3D models, which are driven by far-field pure shear, in order to test the general applicability of the temperature prediction (Fig. 7). The rate of temperature increase in the shear zone is the largest for the 1D model and the smallest for the 3D model. This is because in the 1D model the initial thermal perturbation is at the position of the future shear zone whereas in the 2D (Fig. 7d to f) and 3D (Fig. 7a to c) models the initial thermal perturbation is present only in a fraction of the future shear zones. Also, the background temperature increase due to bulk shear heating of the model domain is the largest in the 3D and the smallest in the 1D model (Fig. 7g to i). Nevertheless, equation

3.1 (associated with the 1D results) accurately predicts the temperature inside the 2D and 3D shear zones after the transient stage of temperature increase. The results also confirm that the initial temperature perturbation applied in the 1D model has no impact on the maximum temperature in the shear zone because the temperature of the 2D and 3D shear zones are unaffected by the initial thermal perturbation. A comparison of profiles of the velocities parallel to the 1D, 2D and 3D shear zones shows that the thickness of the shear zones are essentially identical. Therefore, 1D, 2D and 3D shear zones caused by thermal softening under both far-field pure and simple shear exhibit the same thermo-mechanical characteristics.

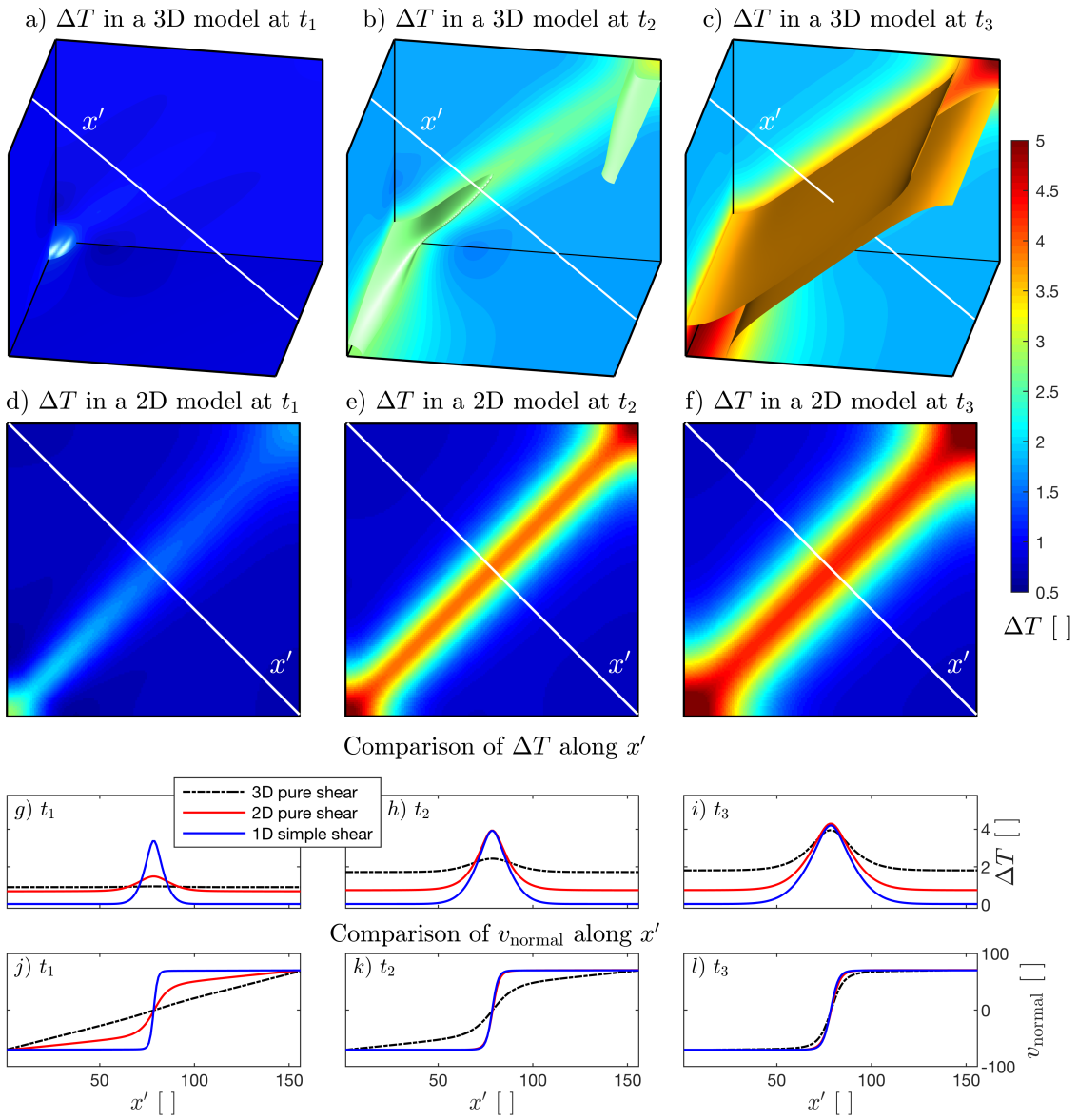

Figure 2.7 – Comparison of temperature and velocity profiles across 1D, 2D and 3D shear zones. a) to c) shows the temperature field for three stages of 3D shear zone formation. d) to f) shows the temperature field for three stages of 2D shear zone formation. The profile lines indicated with x' in both 2D and 3D models are used for the comparison with the 1D model. g) to i) show 1D temperature profile and the 2D and 3D profiles along the x' profile for three different times. j) to l) show the 1D velocity profile and the 2D and 3D profiles along the x'-profile for three different times. The displayed velocity magnitudes are normal to the profile orientation and, hence, parallel to the shear zone orientation.

2.6 Application to dislocation creep flow laws

We apply equation 3.1 to predict the maximum temperature in shear zones using typical flow laws for rock-forming minerals relevant to the lithosphere. Equation (3.1) depends on the duration of deformation. The typical, observed time scale of deformation varies as a function of shear velocity. To make the results for different velocities comparable we assume a characteristic shear strain of 20, which is the ratio of displacement and shear zone thickness (W_γ). As a first order estimate we use one tenth (Fig 4b) of the characteristic thermal width $W_T = 2\sqrt{\kappa t}$ (Fig. 5b) as a shear zone width. With these relationships we can determine a representative characteristic time of the deformation to reach a shear strain of 20:

$$20 = \gamma_c = \frac{t_c \Delta v}{0.2\sqrt{\kappa t_c}} \quad \rightarrow \quad t_c = \left(0.2\frac{\gamma_c\sqrt{\kappa}}{\Delta v}\right)^2 \tag{2.26}$$

which yields $t_c \approx 5$ Ma for a velocity of ≈ 1 cm.yr^{-1}.

For typical plate tectonic velocities in the order of few centimeters per year, the flow laws for wet and dry olivine, and dry plagioclase are associated with maximum temperatures between 500 and 700 °C (Fig. 8). Such temperatures correlate well with typical temperatures of highly sheared basement nappes outcropping in orogens such as the Alps. Typical metamorphic peak temperature ranges between 500 and 650 °C (Keller et al., 2005; Manzotti et al., 2018) and reach up to 800 °C in the Lepontine dome (Nagel, 2008). Takeuchi and Fialko (2012) provided a thorough study of the temperature anomalies around the San Andreas strike-slip fault. They used heat flow and surface deformation measurements to constrain their models. They conclude that a temperature increase of 160 to 375 °C, dependent on rheology, is expected at 20 km depth for a 4 cm.yr^{-1} long term average velocity difference. These values are in a good agreement with our prediction for dry anorthite and olivine and wet olivine flow laws. Flow laws for wet quartzite and Westerly granite provide maximal temperatures < 300 °C in the same velocity range (Fig. 8).

A recent study of Chu et al. (2017) provides well constrained information about the duration of deformation and maximal temperature of eclogite shear zones of the Taconic orogenic belt (New England). The eclogite bodies are hosted in feldspar rich felsic paragneiss. The authors conclude that the *P-T* history of the shear zones can be best explained by shear heating. Using the known displacement, related to the known deformation time, the shear velocities can be constrained to be between 25 - 70 cm.yr^{-1}. For the inferred velocity range the applicable flow law for dry anorthite yields a good fit (Fig. 8).

Rocks that are commonly considered to result from significant shear heating are pseudotachylites. They are often associated to earthquakes, having typically slip velocities on the order of a m.s^{-1} (Bizzarri, 2012). Such fast deformation processes are commonly considered to be dominated by frictional deformation and, hence, frictional heating. However, recent progress in understanding of the physics of friction suggests viscous creep on grain contacts and asperities as the mechanism for velocity weakening of the friction coefficient, reported at high shear-velocity (≈ 1 m.s^{-1}) rock deformation experiments for various rock types (Aharonov and Scholz, 2018). Moreover, a recent experimental study of high shear-velocity (≈ 1 m.s^{-1}) deformation of calcite reports that such fast shear deformation is

characterized by an initial frictional deformation followed by (quasi) steady-state viscous creep (Pozzi et al., 2018). In these experiments most of the strain is generated by (quasi) steady-state viscous creep. Since the (quasi) steady-state temperature developing in our models is path independent (Fig. 2), we can apply our viscous model result to estimate the temperatures in such small-scale and high-velocity shear zones regardless of which deformation mechanism dominates initially. To test the model-based temperature estimations we consider natural pseudotachylites from Corsica (Andersen et al., 2008). The reported peak metamorphic temperature is at least 1750 °C. There are no reported constraints on shear velocities and, therefore, we apply peak slip velocities of 4 m.s^{-1} (that is typical for seismic events with a displacement around 1 m), as an upper limit (Bizzarri, 2012). To estimate a lower bound, we use the width of the main pseudotachylite vein ($W = 1.23$ cm), the displacement ($d = 1$ m, yielding $\gamma_c = d/W \approx 80$) along it and the scaling relationship between characteristic width of shear zones and the duration of deformation (eq. 2.16). Reordering equation (2.16) yields $t = W^2/(1.92^2\kappa) \approx 41$ s (assuming $\kappa \approx 10^{-6}$ m^2.s^{-1}). Using this estimate of duration we can estimate the slip velocity $v = d/t \approx 0.02$ [m.s^{-1}]. As such estimates have typically an order of magnitude uncertainty we take a five times lower value as a lower velocity bound (i.e. 4 mm.s^{-1}). Within this wide velocity range, the predicted temperatures for most flow laws agree with the reported peak temperature (Fig. 8). Clearly, there are many uncertainties and simplifications related to this temperature estimate, but this estimate nevertheless indicates that peak temperatures reported for the considered pseudotachylites potentially could have been generated in viscous shear zones for typical slip velocities, in the order of 1 m.s^{-1}.

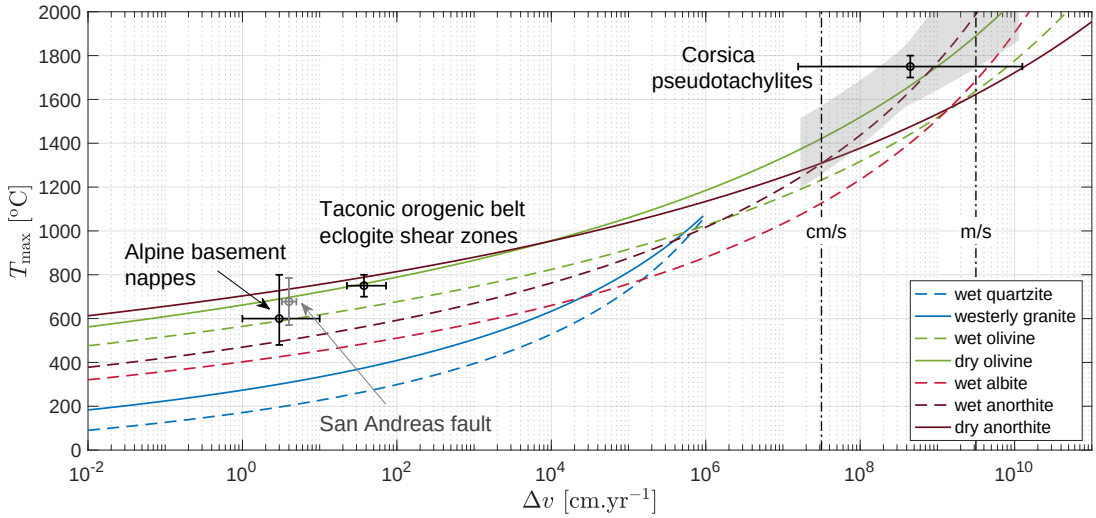

Figure 2.8 – Predicted maximum temperature in shear zones across the scales. Four data points are shown as possible applications. Three of them are direct observations, displayed with black, while the gray is an indirect observation (see in section 6). Equation 3.1 is used for temperature prediction versus the applied boundary velocities, Δv, for different flow laws (see legend and Table 1). The same constant finite shear strain, $\gamma_c = 20$, is assumed for all shear zones and the corresponding duration of the deformation is calculated with equation 2.26. For pseudotachylites the typical values of finite strain are higher. The expected temperature range for $\gamma_c = 80$ is indicated by the light gray area. The quartzite flow laws are not displayed for high velocities because for those the argument of the logarithm is approaching $\exp(-1.1) \approx 0.3$, where the prediction starts to significantly deviate from the solution.

Whether shear heating causes shear localization depends on the initial temperature of the rock because localization will not occur if the ambient rock temperature at the onset of shearing is larger than the predicted maximum temperature. We consider typical lithospheric geotherms and temperatures for the upper crust between 200 and 400 °C, for the lower crust between 400 and 600 °C and for the mantle lithosphere > 600 °C. For typical plate tectonic velocities, we calculate the predicted maximum temperature for different initial temperatures representing the ambient temperature at the onset of deformation (Fig. 9a). The temperature difference, ΔT, between predicted maximal temperature and initial, ambient, temperature indicates the intensity of shear heating and, hence, shear localization by thermal softening. Shear heating is significant for $\Delta T > 50$ °C since for such values of ΔT the heat transfer between shear zone and wall rock is dominated by shear heating (Fig. 5b). For plate tectonic velocities of a few cm.yr^{-1}, shear heating is always important in all three lithospheric units (Fig. 9a). As expected, for the same velocity shear heating is always more intense in the upper and colder regions of the lithospheric units. For example, for a velocity difference of 3 cm.yr^{-1} the expected temperature increase in a lower crust made of ca. 400 °C hot anorthite is between 100 and 150 °C (Fig. 9a).

Shear heating is even more important if we consider a thinned, thermally relaxed continental lithosphere, for example, at a passive continental margin. This is because the temperatures at the top of the lower crust and mantle lithosphere are colder than for a normal continental lithosphere (Fig. 9b).

We also analyze the initial stresses for configurations for which shear heating and strain localization is significant (Fig. 9c and d). We consider scenarios for which $\Delta T > 50$ °C and for which initial shear stresses, τ_{xy}, are < 1 GPa (Fig. 9c and d). The initial shear stresses are the largest stresses during shear zone formation since stress magnitudes decrease during shear zone formation due to thermal softening (Fig. 2c). We assume a velocity difference of 3 cm.yr^{-1} and vary initial bulk strain rates by varying the 1D model size, L. For flow laws of wet anorthite shear heating is significant for ambient temperatures between 380 and 470 °C and for strain rates, $\dot{\epsilon}$, between 10^{-16} and 10^{-13} s^{-1}. For example, for typical tectonic strain rates $\dot{\epsilon} = 10^{-15}$ s^{-1} shear localization by thermal softening is significant for shear stresses between 200 and 400 MPa for ambient temperature between 420 and 470 °C (Fig. 9c). For dry olivine and for $\dot{\epsilon} = 10^{-15}$ s^{-1} thermal softening is significant for shear stresses between 200 and 400 MPa for ambient temperature between 540 and 570 °C (Fig. 9d).

Our results indicate that the shortening of a tectonic plate, for example around a thinned passive continental margin, can likely generate significant shear heating and associated spontaneous shear zone generation by thermal softening. Such shear zone generation can take place in the ductile regime without reaching a brittle-plastic yield stress. Ductile strain localization by thermal softening could cause the generation of subduction zones, which is supported by numerical simulations (e.g. Thielmann and Kaus 2012).

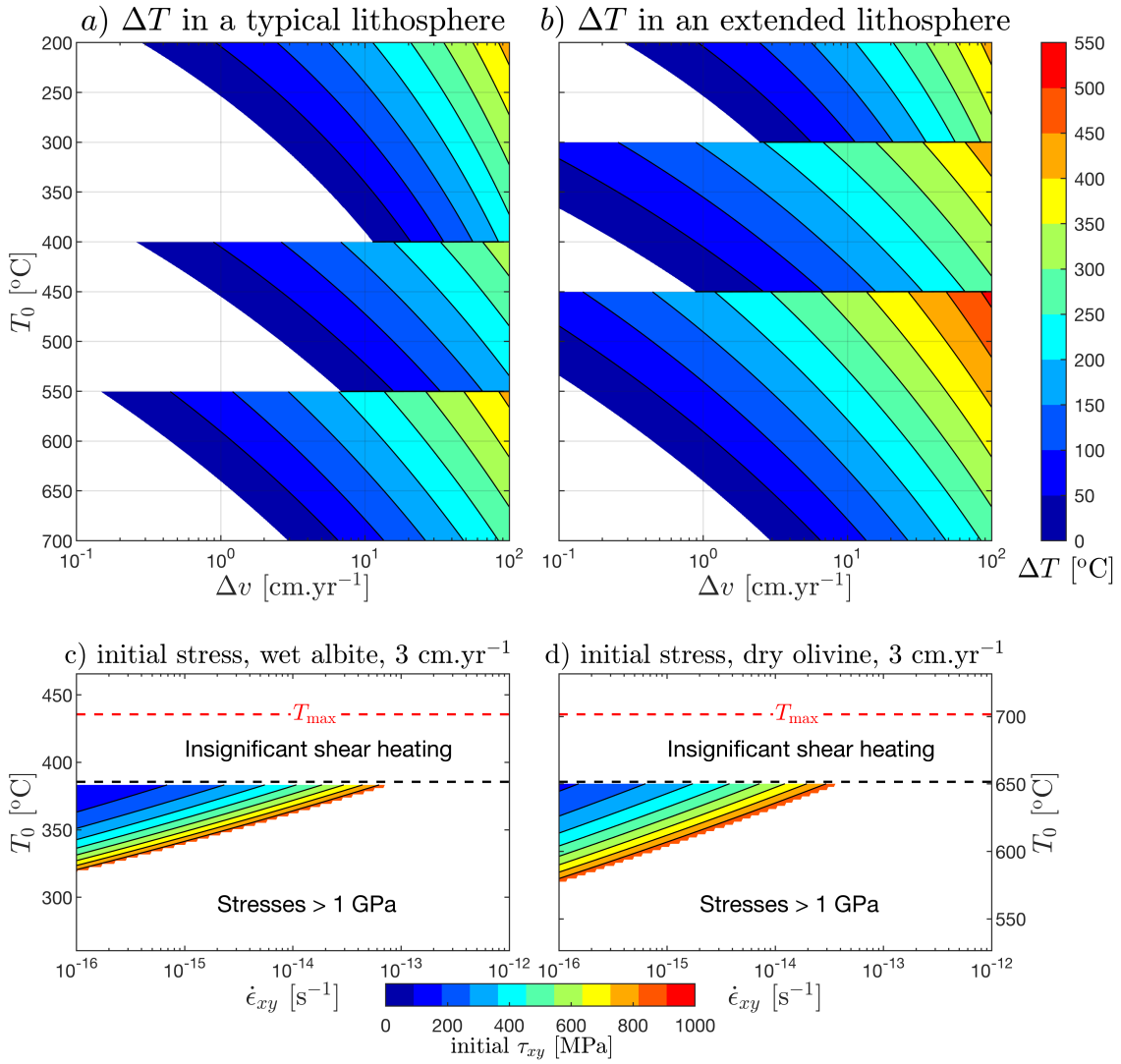

Figure 2.9 – a) and b) show color plots of the temperature difference, ΔT, between the maximum temperature predicted with equation (3.1) and the initial temperature, T_0, corresponding to the ambient temperature at a certain depth in the lithosphere. ΔT is contoured for different values of T_0 and ΔV. ΔT is calculated for a deformation time of 1 Ma. The three regions in the color plots correspond to three different flow laws, namely for Westerly granite (top region representing upper crust), wet anorthite (middle region representing lower crust) and wet olivine (lower region representing mantle lithosphere). c) and d) show color plots of the initial shear stress in 1D simulations as a function of T_0 and applied bulk strain rate, $\dot{\epsilon}_{xy}$. c) shows results for wet albite flow law and d) for dry olivine. The applied velocity difference is 3 cm.yr^{-1} and bulk strain rates are modified by changing the 1D model size. The red dashed horizontal line indicates the maximum temperature, $T_{\max}$, from equation (3.1). To have significant shear localization, T_0 must be at least 50 °C smaller than $T_{\max}$ (see Fig. 5b). Only shear stresses < 1 GPa are displayed. The colored regions in c) and d) indicate the "window" in which shear zone generation by thermal softening is feasible in the lower crust (c) and mantle lithosphere (d).

2.7 Discussion

2.7.1 Localization criterion and Brinkman number

We already suggested the use of $T_{\max} - T_0 > 50^o$C or $Br_1 > \mathrm{e}^2$ as localization criterion. Different versions of the Brinkman number (e.g. Brinkman 1951; Gruntfest 1963; Yuen et al. 1978; Brun and Cobbold 1980) have been proposed and are also known under different names, for example, Gruntfest number (Gr). Using the relations $\Delta v = \dot{\epsilon}_0 L$ and $\tau_0 = \mu_0 \dot{\epsilon}_0$, several Brinkman numbers can be formulated:

$$Br_2 = \frac{\Delta v^2 \mu_0}{\lambda T_0} = \frac{\Delta v^2 \mu_0}{\lambda T_0}\frac{L^2}{L^2} = \frac{\dot{\epsilon}_0^2 \mu_0 L^2}{\lambda T_0} = \frac{\dot{\epsilon}_0 \tau_0 L^2}{\lambda T_0} = \frac{\tau_0^2 L^2}{\mu_0 \lambda T_0} = Gr \tag{2.27}$$

The right-most version with the square of the stress is often termed Gruntfest number, Gr. All parameters with the subscript 0 are initial, bulk values before the occurrence of strain localization or shear zone formation. The parameter L is the model size and not the thickness of the shear zone. The same exercises can be repeated by dividing equation (2.27) with the dimensionless Arrhenius term Q/RT_0, and it would result in several forms of Br_1 (equation 2.24). A particular localization criterion would be

$$\frac{Q}{RT_0}\frac{L^2 \dot{\epsilon}_0 \tau_0}{\lambda T_0} > \mathrm{e}^2, \tag{2.28}$$

which is identical to the criterion of Karato (2008), if e^2 on the right hand side is replaced by 1. The different versions of the Brinkman number are useful for different deformation scenarios. For example, if the deformation is driven by an applied shear stress, then the version with the square of the stress, i.e. Gr, is useful. If the thickness of the shear zone is *a priori* defined by the model or experimental configuration, then a version including L is useful whereby L then represents the pre-defined shear zone thickness. In general, for kinematically driven models, we prefer versions without any length scale L, because the model size does not affect the shear zone evolution (Fig. 2a and 2b).

Our results show the applicability of three different localization criteria. As example, we use $Br_2 > 1$ (Fig. 6c). Applying a typical plate tectonic velocity of 3 cm.yr^{-1}, an effective viscosity of 2×10^{23} Pa.s, a thermal conductivity of 3 W.m^{-1}K^{-1} and an ambient temperature of 500 ^{o}C (773 K) yields $Br_2 \approx 78$. Our results show that for this value of Br_2 shear zone generation by thermal softening can occur (Fig. 6c). Using a typical tectonic strain rate of 10^{-15} s^{-1}, and the applied effective viscosity of 2×10^{23} Pa.s generates a shear stress of 400 MPa, which is a feasible flow stress for the upper and colder regions of the mantle lithosphere or the lower crust. Indeed, the spontaneous generation of km-scale shear zones by thermal softening was demonstrated in 2D thermo-mechanical simulations of lithospheric shortening for viscoelastoplastic rheology (Jaquet et al., 2017; Jaquet and Schmalholz, 2017).

Here, we do not consider viscoelastic effects. However, it was shown that elasticity can significantly impact thermally-induced strain localisation (Regenauer-Lieb and Yuen, 1998; Duretz et al., 2015; Jaquet et al., 2015) so that strain localization can be even more

significant than predicted by our localization criteria.

2.7.2 Shear zone thickness

A ductile shear zone is commonly observable in the field, or experiment, by the significant variation of finite strain across the shear zone. The width of the variation of finite strain across the shear zone is nearly one order of magnitude smaller than the corresponding width of the temperature variation (Fig. 4b). For significant shear heating the finite strain thickness, W_γ, is ca. $2\sqrt{\kappa t}/7$ (Figs. 4b and 5b). We assume that the observable width of a shear zone is determined by values of finite strain > 1. Based on Fig. 4a this observable thickness is approximately 2 to 3 times thicker than W_γ. Assuming a typical thermal diffusivity of 10^{-6} $m^2.s^{-1}$ yields W_γ = ca. 1.5 km and, hence, an observable thickness of 3 to 4.5 km for a shear zone which is active for 1 Ma. For a shear zone which is active for 4 Ma W_γ = ca. 3 km and the observable thickness is 6 to 9 km. Since W_γ only depends on time and is independent on the applied shear velocity it can be applied to any shear velocity and displacement. For example, a shear displacement of 100 km for a shear velocity of 2.5 $cm.yr^{-1}$ requires 4 Ma, for which the observable thickness is 6 to 9 km. A shear zone with such thickness, velocity and displacement is likely typical for major lithospheric shear zones related to subduction zones. Such thickness relation only applies to depth levels in the lithosphere for which thermal softening controls the strain localization. These durations of shear zone activity and corresponding predicted shear zone thicknesses agree also with those formed by thermal softening in 2D thermo-mechanical numerical simulations of lithospheric shortening (Jaquet and Schmalholz 2017; Jaquet et al. 2017). Based on the same relationship we expect sub-mm thickness for all shear zones that have been active for less than a few seconds.

If natural shear zones would have been formed by thermal softening with moderate temperature increase of 75 to 150 °C, then there would be no significant temperature variation between the shear zone and its wall rock because natural shear zones are observable due to the significant finite strain variation. This difference between finite strain and temperature variation explains why many ductile shear zones do not exhibit a significant observable temperature variation. The lack of a sharp and observable temperature variation, for example expressed by variation in metamorphic grade, is not a sufficient argument against the importance of shear heating and thermal softening.

2.7.3 Thermal softening and grain size reduction

There is still ongoing dispute concerning the primary mechanism of ductile strain localization in the lithosphere. Alternative to thermal softening, grain size reduction in combination with mechanisms, such as pinning, that prohibit grain growth (generally referred to as damage) is often proposed as primary strain localization mechanism. Clearly, in nature both mechanisms act simultaneously. We argue that thermal softening is a suitable mechanism for spontaneous strain localization in essentially homogeneous material whereby only minor heterogeneities can trigger strain localization. Grain size reduction can assist thermal softening and grain size reduction is likely a mechanism that is impor-

tant during progressive shear zone evolution and can decrease the widening rate of the finite strain profile due to heat conduction. For example, Thielmann et al. (2015) studied numerically the formation of shear zones by thermal runaway using a combined approach of thermal softening and grain size reduction. They showed that grain size reduction reduces the stress required for thermal runaway and hence assists ductile shear zone formation by thermal softening. Currently, different grain size evolution models are applied, for example, Thielmann et al. (2015) apply the so-called paleowattmeter model in which grain size is a function of flow stress, strain rate and temperature, whereas Platt (2015) applies a piezometer in which grain size depends on flow stress only. To reliably quantify the impact of grain size evolution better constrained grain size evolution models for various rock types are needed.

2.8 Conclusions

A ductile shear zone which is generated spontaneously by thermal softening during a velocity-driven bulk deformation exhibits the following fundamental features: (1) After a transient period of temperature increase the temperature in the shear zone remains constant for linear viscous flow and quasi-constant for power-law viscous flow. (2) The shear stress in the shear zone is largest at the onset of shear zone formation and subsequently decreases towards a (quasi-)constant value associated with the establishment of a (quasi-)constant temperature. (3) The width of temperature variation across the shear zone is 6 to 8 times wider than the variation of the corresponding finite strain. Therefore, the shear zone does not exhibit a sharp, and hence easily observable, temperature variation between highly-strained shear zone and little-strained wall rock. (4) The shear zone is continuously widening during shearing due to thermal conduction between shear zone and wall rock. (5) Shear heating starts to dominate the heat transfer between shear zone and wall rock once the temperature increase in the shear zone is $>$ ca. 50 ^{o}C.

Different versions of the Brinkman number can predict the onset of shear zone generation by thermal softening. However, the Brinkman number cannot quantify the temperature increase inside the shear zone and, hence, the intensity of thermal softening. We derived a new analytical formula that predicts the maximal temperature inside the shear zone. This temperature prediction requires only information on the bulk deformation, such as far-field velocity, flow law and thermal parameters, and, therefore, no *a priori* knowledge of the shear zone itself, such as thickness, flow stress and strain rate. Temperature predictions across the scales of geological velocities show first order agreement with several natural shear zones including Alpine basement nappes, eclogite shear zones and pseudotachylites. We show with 1D, 2D and 3D numerical simulations that this temperature prediction is valid for shear zone generation under both bulk simple and pure shear.

Our results indicate that shear zone generation by thermal softening likely occurs during lithosphere deformation in the continental lower crust and the mantle lithosphere for typical lithospheric velocities of few cm.yr^{-1} or bulk strain rates between 10^{-16} and 10^{-14} s^{-1}. For these deformation conditions, shear stresses of few hundred MPa can already cause shear zone generation by thermal softening.

Based on our results and their application to lithospheric flow laws and deformation conditions, we argue that spontaneous shear zone generation by thermal softening is a feasible and likely the primary mechanism for spontaneous lithospheric scale shear zone generation. Thermal softening is probably a key constituent of subduction initiation, for example, at a thinned passive continental margin. Additional processes, such as grain size reduction, fabric development or fluid-related reactions can cause additional softening during progressive shear zone evolution and likely intensify the strain localization.

Acknowledgements

We thank an anonymous reviewer for constructive and helpful comments. This work was supported by SNF grant No. 200020-149380 and the University of Lausanne. We thank Ludovic Räss for assistance in performing the 3D numerical simulations.

References

Aharonov, E. and C. H. Scholz
2018. A physics-based rock friction constitutive law: Steady state friction. *Journal of Geophysical Research: Solid Earth*, 123(2):1591–1614.

Andersen, T. B., K. Mair, H. Austrheim, Y. Y. Podladchikov, and J. C. Vrijmoed
2008. Stress release in exhumed intermediate and deep earthquakes determined from ultramafic pseudotachylyte. *Geology*, 36(12):995–998.

Bercovici, D. and Y. Ricard
2012. Mechanisms for the generation of plate tectonics by two-phase grain-damage and pinning. *Physics of the Earth and Planetary Interiors*, 202:27–55.

Bizzarri, A.
2012. Analytical representation of the fault slip velocity from spontaneous dynamic earthquake models. *Journal of Geophysical Research: Solid Earth*, 117(B6).

Brinkman, H.
1951. Heat effects in capillary flow i. *Applied Scientific Research*, 2(1):120–124.

Brown, K. M. and Y. Fialko
2012. 'melt welt'mechanism of extreme weakening of gabbro at seismic slip rates. *Nature*, 488(7413):638.

Brun, J. and P. Cobbold
1980. Strain heating and thermal softening in continental shear zones: a review. *Journal of Structural Geology*, 2(1-2):149–158.

Carter, N. L. and M. C. Tsenn
1987. Flow properties of continental lithosphere. *Tectonophysics*, 136(1-2):27–63.

Chu, X., J. J. Ague, Y. Y. Podladchikov, and M. Tian
2017. Ultrafast eclogite formation via melting-induced overpressure. *Earth and Planetary Science Letters*, 479:1–17.

Duretz, T., L. Räss, Y. Podladchikov, and S. Schmalholz
2019. Resolving thermomechanical coupling in two and three dimensions: spontaneous strain localization owing to shear heating. *Geophysical Journal International*, 216(1):365–379.

Duretz, T., S. Schmalholz, and Y. Podladchikov
2015. Shear heating-induced strain localization across the scales. *Philosophical Magazine*, 95(28-30):3192–3207.

Duretz, T., S. Schmalholz, Y. Podladchikov, and D. Yuen
2014. Physics-controlled thickness of shear zones caused by viscous heating: Implications for crustal shear localization. *Geophysical Research Letters*, 41(14):4904–4911.

Fialko, Y. and Y. Khazan
2005. Fusion by earthquake fault friction: Stick or slip? *Journal of Geophysical Research: Solid Earth*, 110(B12).

Fleitout, L. and C. Froidevaux
1980. Thermal and mechanical evolution of shear zones. *Journal of Structural Geology*, 2(1-2):159–164.

Gerya, T.
2009. *Introduction to numerical geodynamic modelling*. Cambridge University Press.

Ghazian, R. K. and S. J. Buiter
2013. A numerical investigation of continental collision styles. *Geophysical Journal International*, 193(3):1133–1152.

Gruntfest, I.
1963. Thermal feedback in liquid flow; plane shear at constant stress. *Transactions of the Society of Rheology*, 7(1):195–207.

Gueydan, F., J. Précigout, and L. G. Montési
2014. Strain weakening enables continental plate tectonics. *Tectonophysics*, 631:189 – 196. Observational and Modelling perspectives on the Mechanical properties of the Lithosphere.

Hersey, M. D.
1936. Note on heat effects in capillary flow. *Physics*, 7(11):403–407.

Herwegh, M., T. Poulet, A. Karrech, and K. Regenauer-Lieb
2014. From transient to steady state deformation and grain size: A thermodynamic approach using elasto-visco-plastic numerical modeling. *Journal of Geophysical Research: Solid Earth*, 119(2):900–918.

Hirth, G. and D. Kohlstedt
2003. Rheology of the upper mantle and the mantle wedge: A view from the experimentalists. *Inside the subduction Factory*, Pp. 83–105.

Hirth, G., C. Teyssier, and J. W. Dunlap
2001. An evaluation of quartzite flow laws based on comparisons between experimentally and naturally deformed rocks. *International Journal of Earth Sciences*, 90(1):77–87.

Jaquet, Y., T. Duretz, D. Grujic, H. Masson, and S. M. Schmalholz
2017. Formation of orogenic wedges and crustal shear zones by thermal softening, associated topographic evolution and application to natural orogens. *Tectonophysics*.

Jaquet, Y., T. Duretz, and S. M. Schmalholz
2015. Dramatic effect of elasticity on thermal softening and strain localization during lithospheric shortening. *Geophysical Journal International*, 204(2):780–784.

Jaquet, Y. and S. M. Schmalholz
2017. Spontaneous ductile crustal shear zone formation by thermal softening and related stress, temperature and strain rate evolution. *Tectonophysics*.

Karato, S.-i.
2008. *Deformation of Earth Materials: An Introduction to the Rheology of Solid Earth by Shun-ichiro Karato*. Cambridge University Press.

Kaus, B. J. and Y. Y. Podladchikov
2006. Initiation of localized shear zones in viscoelastoplastic rocks. *Journal of Geophysical Research: Solid Earth*, 111(B4).

Keller, L. M., M. Hess, B. Fügenschuh, and S. M. Schmid
2005. Structural and metamorphic evolution of the camughera–moncucco, antrona and monte rosa units southwest of the simplon line, western alps. *Eclogae Geologicae Helvetiae*, 98(1):19–49.

Leloup, P. H., Y. Ricard, J. Battaglia, and R. Lacassin
1999. Shear heating in continental strike-slip shear zones: model and field examples. *Geophysical Journal International*, 136(1):19–40.

Mako, C. A. and M. J. Caddick
2018. Quantifying magnitudes of shear heating in metamorphic systems. *Tectonophysics*, 744:499–517.

Mancktelow, N. S. and G. Pennacchioni
2005. The control of precursor brittle fracture and fluid–rock interaction on the development of single and paired ductile shear zones. *Journal of Structural Geology*, 27(4):645–661.

Manzotti, P., V. Bosse, P. Pitra, M. Robyr, F. Schiavi, and M. Ballèvre
2018. Exhumation rates in the gran paradiso massif (western alps) constrained by in situ

u–th–pb dating of accessory phases (monazite, allanite and xenotime). *Contributions to Mineralogy and Petrology*, 173(3):24.

Montési, L. G.
2013. Fabric development as the key for forming ductile shear zones and enabling plate tectonics. *Journal of Structural Geology*, 50:254–266.

Moore, J. D. and B. Parsons
2015. Scaling of viscous shear zones with depth-dependent viscosity and power-law stress–strain-rate dependence. *Geophysical Journal International*, 202(1):242–260.

Nagel, T. J.
2008. Tertiary subduction, collision and exhumation recorded in the adula nappe, central alps. *Geological Society, London, Special Publications*, 298(1):365–392.

Omlin, S.
2016. *Development of massively parallel near peak performance solvers for three-dimensional geodynamic modelling.* PhD thesis, University of Lausanne.

Platt, J. and W. Behr
2011. Grainsize evolution in ductile shear zones: Implications for strain localization and the strength of the lithosphere. *Journal of Structural Geology*, 33(4):537–550.

Platt, J. P.
2015. Influence of shear heating on microstructurally defined plate boundary shear zones. *Journal of Structural Geology*, 79:80–89.

Pozzi, G., N. De Paola, S. B. Nielsen, R. E. Holdsworth, and L. Bowen
2018. A new interpretation for the nature and significance of mirror-like surfaces in experimental carbonate-hosted seismic faults. *Geology*.

Regenauer-Lieb, K. and D. A. Yuen
1998. Rapid conversion of elastic energy into plastic shear heating during incipient necking of the lithosphere. *Geophysical Research Letters*, 25(14):2737–2740.

Regenauer-Lieb, K., D. A. Yuen, and J. Branlund
2001. The initiation of subduction: criticality by addition of water? *Science*, 294(5542):578–580.

Rybacki, E. and G. Dresen
2004. Deformation mechanism maps for feldspar rocks. *Tectonophysics*, 382(3):173–187.

Schmalholz, S. and T. Duretz
2015. Shear zone and nappe formation by thermal softening, related stress and temperature evolution, and application to the alps. *Journal of Metamorphic Geology*, 33(8):887–908.

Sibson, R. H.
1975. Generation of pseudotachylyte by ancient seismic faulting. *Geophysical Journal International*, 43(3):775–794.

Takeuchi, C. S. and Y. Fialko
2012. Dynamic models of interseismic deformation and stress transfer from plate motion to continental transform faults. *Journal of Geophysical Research: Solid Earth*, 117(B5).

Thielmann, M. and B. J. Kaus
2012. Shear heating induced lithospheric-scale localization: Does it result in subduction? *Earth and Planetary Science Letters*, 359:1–13.

Thielmann, M., A. Rozel, B. Kaus, and Y. Ricard
2015. Intermediate-depth earthquake generation and shear zone formation caused by grain size reduction and shear heating. *Geology*, 43(9):791–794.

Versteeg, H. and W. Malalasekra
2007. *An Introduction to Computational Fluid Dynamics: The Finite Volume Method (2nd Edition)*. Pearson.

White, S. t. and R. Knipe
1978. Transformation-and reaction-enhanced ductility in rocks. *Journal of the Geological Society*, 135(5):513–516.

Yuen, D., L. Fleitout, G. Schubert, and C. Froidevaux
1978. Shear deformation zones along major transform faults and subducting slabs. *Geophysical Journal International*, 54(1):93–119.

CHAPTER 3

Thermal softening induced subduction initiation at a passive margin

Dániel Kiss, Lorenzo G. Candioti, Thibault Duretz
and Stefan M. Schmalholz

Under review in *Geophysical Journal International*

Abstract

We present two-dimensional numerical simulations of convergence at a hyper-extended passive margin with exhumed sub-continental mantle. We consider visco-elasto-plastic deformation, heat transfer and thermo-mechanical coupling by shear heating and associated thermal softening due to temperature dependent viscosity. The simulations show subduction initiation for convergence velocities of 2 cm.yr^{-1}, initial Moho temperatures of 525 °C and reasonable maximal deviatoric stresses around the Moho of ca 800 MPa. Subduction initiates in the region with thinned continental crust and is controlled by a thermally-activated ductile shear zone in the mantle lithosphere. The shear zone temperature can be predicted with a recently published analytical expression. The criterion for subduction initiation is a temperature difference of at least 225 °C between predicted temperature and intial Moho temperature. The modelled forced subduction agrees with geological data and reconstructions of subduction during closure of the Piemont-Liguria basin, during convergence of the European and Adriatic plates, causing the Alpine orogeny.

3.1 Introduction

Subduction is an essential feature of plate tectonics, however, the processes controlling subduction initiation (SI) are still contentious (e.g. Vlaar and Wortel, 1976; Gurnis et al., 2004; Stern and Gerya, 2018). SI mechanisms are commonly classified as induced (i.e. caused by plate motions far away from the SI site) and spontaneous (i.e. caused by forces originating at the SI site; e.g. Stern, 2004). We focus here on induced SI at a passive margin with exhumed sub-continental mantle (e.g. Peron-Pinvidic and Manatschal, 2009). SI requires the formation of a major shear zone that transects the lithospheric mantle. Such shear zone could be pre-defined by inherited trans-lithospheric weak zones (e.g. Tommasi et al., 2009) or could be generated spontaneously by softening mechanisms (see recent review of Stern and Gerya, 2018), such as shear heating and associated thermal softening (e.g. Thielmann and Kaus, 2012), grain size reduction and microstructural damage (e.g. Bercovici and Ricard, 2012; Mulyukova and Bercovici, 2018) or softening due to increased water content along fluid pathways (e.g. Regenauer-Lieb et al., 2001). Out of the many softening mechanisms proposed to be important for SI, thermal softening is of particular interest because it (i) must occur due to energy conservation and temperature-dependent rock strength, and (ii) requires no additional assumptions about microscale processes such as grain size distribution and evolution or permeability structure and evolution. Recently, Kiss et al. (2019) presented a new analytical expression that predicts the quasi-constant temperature in a ductile shear zone that formed spontaneously by thermal softening. Their temperature prediction does not require any information of the shear zone itself, such as its thickness, stress or strain rate. The prediction was also validated with one-dimensional (1D), 2D and 3D numerical simulations, considering dislocation creep in homogeneous material having homogeneous ambient temperature. Kiss et al. (2019) speculated that their estimate is also applicable for visco-elasto-plastic deformation of the lithosphere, exhibiting heterogeneous material properties, due to crust and mantle, and considerable

ambient temperature variation across the lithosphere. Furthermore, Kiss et al. (2019) argue that thermal softening may likely trigger SI at passive margins for convergence velocities on the order of few centimeters per year. Here, we present 2D thermo-mechanical numerical simulations of convergence at a passive margin and show that (i) the expression of Kiss et al. (2019) indeed accurately predicts the temperature in lithospheric mantle shear zones caused by thermal softening and (ii) induced SI by thermal softening indeed occurs for laboratory-derived flow laws, natural convergence velocities and realistic temperatures. We argue that our model is applicable to SI during closure of the Piemont-Liguria basin, during convergence of the European and Adriatic plates, causing the Alpine orogeny.

3.2 Methods

3.2.1 Mathematical model

Our model for lithosphere deformation is based on continuum mechanics (e.g. Mase and Mase, 1970; Turcotte and Schubert, 2014). We assume slow, incompressible deformation under gravity, without inertial forces. We consider visco-elasto-plastic deformation assuming a Maxwell visco-elastic model and a Drucker-Prager brittle-plastic yield criterion. Heat transfer occurs by conduction, advection and production. Heat transfer and deformation are coupled by shear heating, because dissipative work is converted into heat, required by the conservation of energy. The heat source due to shear heating is determined by the sum of the products of deviatoric stress and visco-plastic strain rate tensor components, $\tau_{ij}\dot{\epsilon}_{ij}^{\mathrm{vp}}$, and is referred to here as dissipation. The applied equations are described in Schmalholz et al. (2019) and are also described in the supplementary material. The governing system of partial differential equations is solved numerically with a finite-difference/marker-in-cell method (e.g. Gerya and Yuen, 2003). The diffusive terms in the force balance and heat transfer equations are discretized on an Eulerian staggered grid while advection and rotation terms are treated explicitly using a set of Lagrangian markers and a 4th order in space / 1st order in time Runge-Kutta scheme. The model topography is a material interface defined by a Lagrangian marker chain which is displaced with the numerically calculated velocity field (Duretz et al., 2016). Surface evolution is mimicked by a linear diffusion of the topography. Where deposition occurs, the material parameters of sediments (Table S1) are assigned to the newly appearing material. Densities are calculated with an equation of state using compressibility and thermal expansion factors. Applied parameters are given in Table S1.

Considering dislocation creep and velocity driven shearing, Kiss et al. (2019) shows that the temperature in the shear zone, caused by thermal softening, always approaches a quasi-constant temperature that increases only slightly with progressive deformation time, t. This temperature, T_{SH}, is predicted by:

$$T_{\mathrm{SH}} \approx -1.13\,\frac{Q}{nR}\left[\ln\left(\frac{\Delta v^2 nR}{\lambda Q}A^{-\frac{1}{n}}\left\{\frac{\Delta v}{\sqrt{\kappa t}}\right\}^{\frac{1}{n}-1}\right)+1.1\right]^{-1}. \tag{3.1}$$

where Δv is the far-field velocity difference (either for pure or simple shear); all other flow law and thermal parameters are given in Table S1.

3.2.2 Model configuration

The model mimics a hyper-extended passive margin with exhumed sub-continental mantle (Fig. 3.1a). The model is 1500 km wide and 400 km deep. In the exhumed mantle domain (left model side), the lithosphere is 90 km thick. The mantle flow law in the entire model domain is for dry olivine with a combination of dislocation, diffusion and Peierls creep (Kameyama et al., 1999; Hirth and Kohlstedt, 2003) (Fig. 3.1a). The continental lithosphere has a 20 km thick upper crust with a flow law for westerly granite (Carter and Tsenn, 1987). The lower crust is 10 km thick with a flow law for Maryland diabase (Mackwell et al., 1998). In the middle of the model the crust thins gradually to zero thickness towards the exhumed mantle domain within a 100 km wide zone (Fig. 3.1a). The lithosphere is initially in isostatic equilibrium generating an initial topographic difference between regions of exhumed mantle and unthinned crust of 5 km. The depth of the lithosphere-asthenosphere boundary below the unthinned crust is 123 km.

We apply free slip boundary conditions at the bottom and at the right model sides. The top boundary is a free surface. At the left boundary we apply a constant horizontal inflow velocity in the upper 200 km and a constant outflow velocity in the lower 200 km, so that the vertically-integrated velocity is zero (e.g. Erdős et al., 2014). We apply constant temperature of 15 °C at the free surface, constant 1350 °C at the model bottom and zero heat flux on the two sides. The asthenosphere is initially set to $T = 1350$°C, while the initial lithospheric equilibrium temperature is calculated. During simulations, we use higher thermal conductivities in the asthenosphere to mimic the higher effective thermal conductivity due to mantle convection. We apply different thermal conductivities in the crust to vary slightly the initial Moho (i.e. crust-mantle boundary) temperature (Table S1).

We present three simulations: (1) with a 525 °C initial Moho temperature and 2 cm.yr^{-1} convergence velocity, (2) with a 550 °C initial Moho temperature and 2 cm.yr^{-1} convergence velocity, (3) with a 550 °C initial Moho temperature and 4 cm.yr^{-1} convergence velocity.

3.3 Results

In simulation (1) visco-elastic stresses build up during the initial stages of convergence to reach the brittle-plastic yield and steady-state viscous flow stress (Fig. 3.1b and d). The evolving stress field shows the highest deviatoric stress magnitudes of ca 800 MPa inside the lower crust and around the brittle-ductile transition (i.e. transition from Drucker-Prager yield to any of the the creep mechanisms) in the exhumed mantle region (Fig. 3.1b and d). Initially, convergence is characterized by distributed thickening and associated dissipative heating, resulting in a ca 75 °C temperature rise around the Moho during the first 7 Myr (see 500 and 600 °C isotherm of Fig. 3.1a and c). The lower crust is

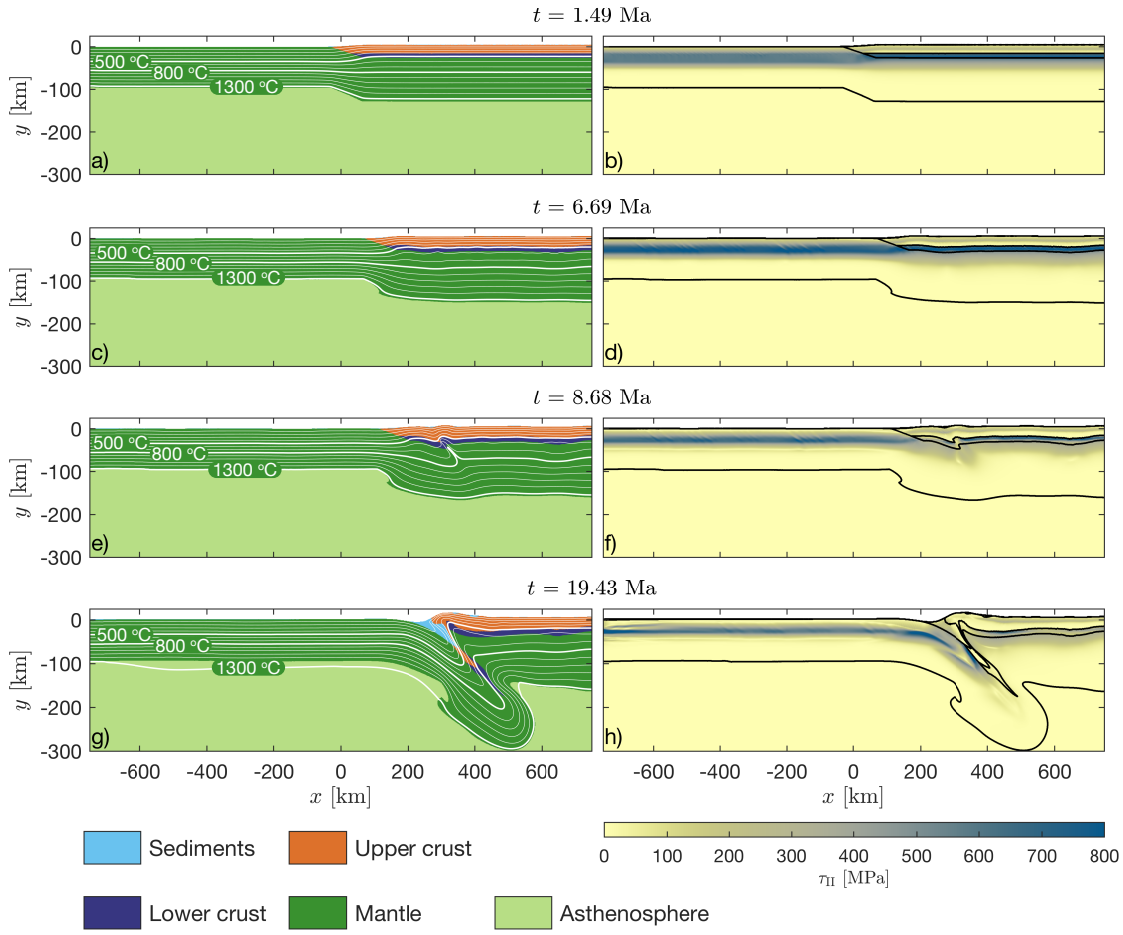

Figure 3.1 – Evolution of model geometry (left column) and stress field (right column) for simulation (1). Left column: White lines indicate isotherms every 100 °C and colored field indicate different model units; see legend below left column. Right column: Stress is quantified with second invariant of deviatoric stress tensor. Black lines indicate from bottom to top: lithosphere-asthenosphere boundary, Moho and upper-lower crust boundary. Colourmaps are from Crameri (2018).

slightly folding causing small lateral stress variations (Fig. 3.1d). Shear heating and thermal softening around the Moho is locally efficient enough to cause the spontaneous development of a ductile shear zone ca 150 km away from the transition between crust and exhumed mantle (at x-position 300 km in Fig. 3.1c, d, e and f). The temperature rise around the shear zone just below the Moho is ca 200 °C (Fig. 3.1e). Due to thermal softening and localization the stresses decrease by several hundred MPa (Fig. 3.1d and f). During progressive convergence, the shear zone remains localized and forms a subduction zone, which subducts the exhumed mantle and parts of the thinned crustal region below the continental lithosphere with normal crustal thickness (Fig. 3.1g and h). Upper crustal material and sediments, deposited in the trench region, are subducted and lubricate the subduction interface. Once crustal material is subducted to ca 90 km depth the small stresses, due to elevated temperatures and lubrication, do not generate significant shear heating and dissipation anymore (Fig. 3.2a).

For simulation (2) with initially only 25 °C higher Moho temperatures the dissipation is smaller due to the smaller stresses resulting from a smaller effective viscosity around the Moho. Thermal softening still impacts the deformation of the lithosphere, but causes

localized thickening of the crust because a localized shear zone could not develop (Fig. 3.2b). For simulation (3) the initial Moho temperature is identical to the one in simulation (2) but the convergence velocity is increased to 4 cm.yr^{-1}. For the higher convergence velocities, thermal softening causes again a localized shear zone and subduction similar to simulation (1) (Fig. 3.2c). For simulations (2) and (3) the initially 25 °C higher Moho temperatures result in considerably lower stresses, post-localisation (figures showing the detailed evolution of simulations (1), (2) and (3) are given in the supplementary material).

To test the temperature prediction of equation (3.1) we calculate T_{SH} for the mantle lithosphere for the applied parameters and specific times. Simulations (1) and (3) generated a localized ductile shear zone and corresponding values of T_{SH} are 754 °C and 786 °C, respectively (Fig. 3.2a and c). Different values of T_{SH} are due to different velocities and/or simulation times corresponding to the displayed results (Fig. 3.2). We plot the dissipation together with the isotherms for the corresponding value of T_{SH}, $T_{SH} \pm 50$°C and $T_{SH} \pm 100$°C. For the temperature comparison, we chose a time step for which the dissipation in the mantle was highest. Maximal dissipation in simulations (1) and (3) is on the order of 100 μWm^{-3} which is approximately two orders of magnitude larger than heat production due to radioactive decay (Table S1). The isotherms of T_{SH} follow closely the orientation of the ductile shear zones indicated by the band of high dissipation in the mantle lithosphere (Fig. 3.2a and c). Therefore, equation (3.1) can predict ductile shear zone temperature in models of visco-elasto-plastic lithosphere deformation.

3.4 Discussion

The equation for T_{SH} was tested by Kiss et al. (2019) with 1D, 2D and 3D numerical simulations for dislocation creep, homogeneous material properties and homogeneous ambient temperature. For these conditions, Kiss et al. (2019) proposed that T_{SH} should be at least 50 °C higher than the ambient temperature to cause shear zone formation. The conditions in the presented lithosphere models are far more complex due to the visco-elasto-plastic rheological model, the heterogeneous material properties in upper crust, lower crust and mantle lithosphere and the significant temperature gradients across the lithosphere. To initiate a subduction zone, a significant shear zone, associated with decreased deviatoric stress (Fig. 3.1f and h), must form in the mantle lithosphere (Fig. 3.2). Hence, we use the dislocation creep flow law parameters for the mantle to calculate T_{SH} representative for the mantle lithosphere. To illustrate the slight time dependence of T_{SH}: a time interval of 2.6 Myr generates an increase of T_{SH} of only 5 °C (Fig. 3.2a and b). We propose to use the initial Moho temperature as representative ambient temperature, because spontaneous ductile shear zone formation by thermal softening occurs most likely around the Moho where deviatoric stress in mantle lithosphere and/or lower crust are highest. For our model configuration, the predicted T_{SH} of ca 750 °C is ca 225 °C higher than the initial Moho temperature of 525 °C in simulation (1). For simulation (2) with an initial Moho temperature of 550 °C a localized shear zone did not form. Hence, for the presented configuration, a temperature difference, ΔT, between T_{SH} and the initial Moho temperature, of at least 225 °C is required to generate a localized ductile mantle shear zone and to ini-

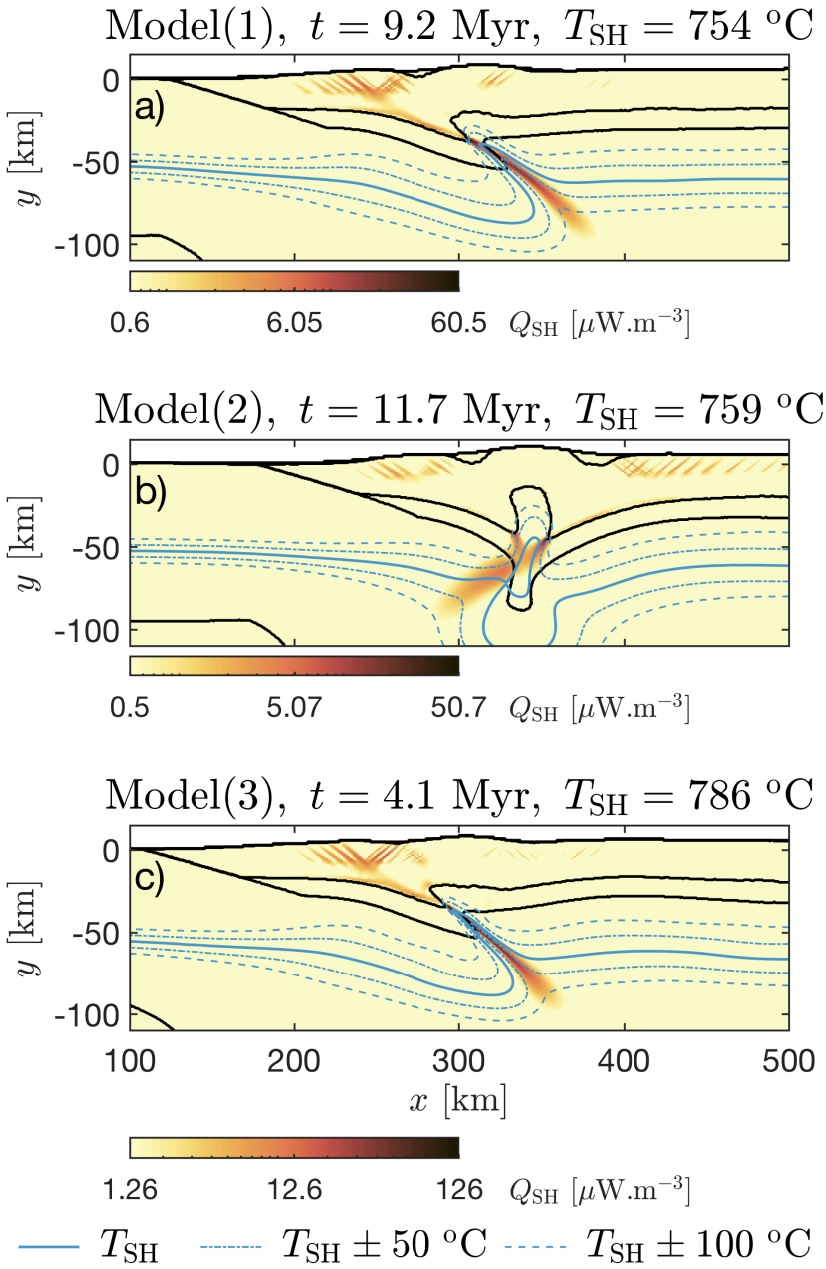

Figure 3.2 – Colourplot of visco-plastic dissipation, Q_{SH}, for models (1, a) to (3, c) at specific simulation times, t. Values of T_{SH} are calculated with equation (3.1) for parameters of mantle dislocation creep (Table S1), corresponding convergence velocity and simulation time. Isotherms are plotted for corresponding T_{SH}, $T_{SH} \pm 50$°C and $T_{SH} \pm 100$°C (see legend).

tiate subduction. In the lithospheric scale model, a larger ΔT is needed to initiate a shear zone than for homogeneous material ($\Delta T >$ ca 50 °C). The higher values of ΔT for the lithospheric scale shear zone formation are likely due to the fact that during lithospheric deformation additional modes of localized deformation are possible, such as localized folding or thickening. For values of $\Delta T <$ ca 225 °C localized thickening dominates in our simulation (Fig. 3.2b). However, the localized thickening is also associated with dissipation and thermal softening so that thermal softening also strongly affects lithosphere deformation even if it does not result in localized shear zone formation.

The calculated temperatures of the mantle shear zones are between ca 750 to 900 °C at

depth between ca 40 and 100 km, and are in broad agreement with temperature estimates for natural mantle shear zones (e.g. Vauchez et al., 2012).

We argue that thermal softening is an important mechanism to trigger the spontaneous formation of ductile shear zones in the mantle lithosphere and to initiate subduction during plate convergence. In nature, additional processes such as grain size reduction or anisotropy development will most likely intensify the localization and stabilize the shear zone. For example, fundamental 0D and 1D models of thermal softening coupled with grain size reduction show that grain size reduction can decrease the critical stress required to initiated shear zones by thermal softening (Thielmann et al., 2015). For other mantle flow laws (e.g. Gouriet et al., 2019), that might provide smaller deviatoric stress than the applied dislocation and Peierls flow laws, slightly higher convergence velocities and/or smaller initial Moho temperatures can compensate the smaller stresses so that thermal softening can be significant for "weaker" mantle flow laws for typical convergence velocities of a few $cm.yr^{-1}$.

Our model configuration mimics an idealized hyper-extended magma-poor passive margin with exhumed sub-continental mantle. Such margin structure was observed at the Iberia-Newfoundland margins and geologically reconstructed for the margins of the Jurassic Piemont-Liguria basin between the European and Adriatic plates (e.g. Peron-Pinvidic and Manatschal, 2009; Mohn et al., 2010). Several studies argue that forced, convergence induced, subduction initiation was the likely mechanism to initiate subduction in the Piemont-Liguria basin, related to the northward migration of Africa (e.g. De Graciansky et al., 2010; McCarthy et al., 2018). Furthermore, subduction in the Western Alps started in the continental region of the distal Adriatic margin, because the earliest Alpine high-pressure units are the Sesia-Dent Blanche crustal units, which are attributed to the former Adriatic margin (e.g. Manzotti et al., 2014). Forced subduction, with (i) subduction initiation in the continental crustal region of a passive margin and (ii) earliest subduction of crustal margin units followed by subduction of exhumed mantle, was proposed for the Western Alps and is in agreement with our model results. We, hence, argue that subduction initiation in the Piemont-Liguria basin was presumably forced by the convergence between Africa and Europe and was likely triggered by thermal softening.

We present here simulations of subduction initiation for a possible configuration of a hyper-extended margin. A systematic study with different initial geometries, temperature fields and combination of flow laws is beyond the scope of our study.

3.5 Conclusions

We show with 2D thermo-mechanical numerical simulations that induced SI occurs due to thermal softening at passive margins with exhumed sub-continental mantle. SI occurs for convergence velocities of 2 $cm.yr^{-1}$, Moho temperatures below 550 °C and maximal deviatoric stresses around the Moho of ca 800 MPa. Such maximal stresses are in agreement with stress estimates based on experimentally determined Peierls creep flow laws of peridotites Jain et al. 2017. Subduction initiates in the margin region of thinned continental crust. The modelled SI agrees with subduction scenarios that are geologically reconstructed for

the closure of the Piemont-Liguria basin.

The maximal temperature in the ductile mantle shear zone can be predicted with an analytical expression (eq. 3.1). If the predicted temperature is at least 225 °C higher than the initial Moho temperature, then subduction initiation triggered by thermal softening is most likely to occur. The analytical solution can, hence, in principle be used as criterion for forced subduction initiation by thermal softening. More simulations for different model configurations and 3D scenarios are required to test the general applicability of the proposed SI criterion.

Thermal softening is an important macroscale mechanism that affects lithosphere deformation and can initiate kilometre-scale lithospheric shear zones. In combination with microscale softening processes, such as grain size reduction, thermal softening is likely a key process for the initiation of natural subduction zones.

Acknowledgement

This work is supported by SNF project 200020-149380 and the University of Lausanne.

References

Bercovici, D. and Y. Ricard
2012. Mechanisms for the generation of plate tectonics by two-phase grain-damage and pinning. *Physics of the Earth and Planetary Interiors*, 202:27–55.

Carter, N. L. and M. C. Tsenn
1987. Flow properties of continental lithosphere. *Tectonophysics*, 136(1-2):27–63.

Crameri, F.
2018. Scientific colour-maps.

De Graciansky, P.-C., D. G. Roberts, and P. Tricart
2010. *The Western Alps, from rift to passive margin to orogenic belt: an integrated geoscience overview*, volume 14. Elsevier.

Duretz, T., D. A. May, and P. Yamato
2016. A free surface capturing discretization for the staggered grid finite difference scheme. *Geophysical Journal International*, 204(3):1518–1530.

Erdős, Z., R. S. Huismans, P. van der Beek, and C. Thieulot
2014. Extensional inheritance and surface processes as controlling factors of mountain belt structure. *Journal of Geophysical Research: Solid Earth*, 119(12):9042–9061.

Gerya, T. V. and D. A. Yuen
2003. Characteristics-based marker-in-cell method with conservative finite-differences schemes for modeling geological flows with strongly variable transport properties. *Physics of the Earth and Planetary Interiors*, 140(4):293–318.

Gouriet, K., P. Cordier, F. Garel, C. Thoraval, S. Demouchy, A. Tommasi, and P. Carrez
2019. Dislocation dynamics modelling of the power-law breakdown in olivine single crystals: Toward a unified creep law for the upper mantle. *Earth and Planetary Science Letters*, 506:282–291.

Gurnis, M., C. Hall, and L. Lavier
2004. Evolving force balance during incipient subduction. *Geochemistry, Geophysics, Geosystems*, 5(7).

Hirth, G. and D. Kohlstedt
2003. Rheology of the upper mantle and the mantle wedge: A view from the experimentalists. *Inside the subduction Factory*, Pp. 83–105.

Jain, C., J. Korenaga, and S.-i. Karato
2017. On the yield strength of oceanic lithosphere. *Geophysical Research Letters*, 44(19):9716–9722.

Kameyama, M., D. A. Yuen, and S.-I. Karato
1999. Thermal-mechanical effects of low-temperature plasticity (the peierls mechanism) on the deformation of a viscoelastic shear zone. *Earth and Planetary Science Letters*, 168(1-2):159–172.

Kiss, D., Y. Podladchikov, T. Duretz, and S. M. Schmalholz
2019. Spontaneous generation of ductile shear zones by thermal softening: Localization criterion, 1d to 3d modelling and application to the lithosphere. *Earth and Planetary Science Letters*, 519:284–296.

Mackwell, S., M. Zimmerman, and D. Kohlstedt
1998. High-temperature deformation of dry diabase with application to tectonics on venus. *Journal of Geophysical Research: Solid Earth*, 103(B1):975–984.

Manzotti, P., M. Ballevre, M. Zucali, M. Robyr, and M. Engi
2014. The tectonometamorphic evolution of the sesia–dent blanche nappes (internal western alps): review and synthesis. *Swiss Journal of Geosciences*, 107(2-3):309–336.

Mase, G. E. and G. Mase
1970. *Continuum mechanics*, volume 970. McGraw-Hill New York.

McCarthy, A., C. Chelle-Michou, O. Müntener, R. Arculus, and J. Blundy
2018. Subduction initiation without magmatism: The case of the missing alpine magmatic arc. *Geology*, 46(12):1059–1062.

Mohn, G., G. Manatschal, O. Müntener, M. Beltrando, and E. Masini
2010. Unravelling the interaction between tectonic and sedimentary processes during lithospheric thinning in the alpine tethys margins. *International Journal of Earth Sciences*, 99(1):75–101.

Mulyukova, E. and D. Bercovici
2018. A theoretical model for the evolution of microstructure in lithospheric shear zones. *Geophysical Journal International*, 216(2):803–819.

Peron-Pinvidic, G. and G. Manatschal
2009. The final rifting evolution at deep magma-poor passive margins from iberia-newfoundland: a new point of view. *International Journal of Earth Sciences*, 98:1581–1597.

Regenauer-Lieb, K., D. A. Yuen, and J. Branlund
2001. The initiation of subduction: criticality by addition of water? *Science*, 294(5542):578–580.

Schmalholz, S. M., T. Duretz, G. Hetényi, and S. Medvedev
2019. Distribution and magnitude of stress due to lateral variation of gravitational potential energy between indian lowland and tibetan plateau. *Geophysical Journal International*, 216(2):1313–1333.

Stern, R. J.
2004. Subduction initiation: spontaneous and induced. *Earth and Planetary Science Letters*, 226(3-4):275–292.

Stern, R. J. and T. Gerya
2018. Subduction initiation in nature and models: A review. *Tectonophysics*, 746:173–198.

Thielmann, M. and B. J. Kaus
2012. Shear heating induced lithospheric-scale localization: Does it result in subduction? *Earth and Planetary Science Letters*, 359:1–13.

Thielmann, M., A. Rozel, B. Kaus, and Y. Ricard
2015. Intermediate-depth earthquake generation and shear zone formation caused by grain size reduction and shear heating. *Geology*, 43(9):791–794.

Tommasi, A., M. Knoll, A. Vauchez, J. W. Signorelli, C. Thoraval, and R. Logé
2009. Structural reactivation in plate tectonics controlled by olivine crystal anisotropy. *Nature Geoscience*, 2(6):423.

Turcotte, D. and G. Schubert
2014. *Geodynamics*. Cambridge university press.

Vauchez, A., A. Tommasi, and D. Mainprice
2012. Faults (shear zones) in the earth's mantle. *Tectonophysics*, 558:1–27.

Vlaar, N. and M. Wortel
1976. Lithospheric aging, instability and subduction. *Tectonophysics*, 32(3-4):331–351.

3.6 Supplementary material

Contents of this file

1. Governing equations
2. Table S1
3. Figures S1, S2 and S3

Introduction

This supporting material provides the description of the equations used in the numerical model, three additional figures and a table with the applied model parameters. Table S1 shows the parameters used for the simulations shown in the main article and also the parameters which have been used for simulations shown in Figures S1 to S3. Figure S1, S2 and S3 show the structural, thermal and stress evolution of models (1), (2) and (3), respectively.

Governing equations (Schmalholz et al., 2018)

The applied numerical algorithm solves the partial differential equations of continuum mechanics for 2D slow deformations (no inertia) coupled with heat transfer under gravity. The force balance equations are:

$$\frac{\partial \sigma_{ij}}{\partial x_j} = -\rho b_i, \tag{3.2}$$

where i and j are indexes of either 1 or 2 and represent the horizontal x-direction ($i, j = 1$) and vertical y-direction ($i, j = 2$), $b_1 = 0$ and $b_2 = g$. σ_{ij} are the total Maxwell-visco-elastic stress tensor components, which are expressed using a backward-Euler rule (e.g. Schmalholz et al., 2001) by

$$\partial \sigma_{ij} = -P + 2\left(\frac{1}{\eta} + \frac{1}{G\Delta t}\right)^{-1} \dot{\varepsilon}_{ij} + \left(1 + \frac{G\Delta t}{\eta}\right)^{-1} \sigma_{ij}^{\mathrm{o}} + J_{ij}, \tag{3.3}$$

where P corresponds to the pressure, $\dot{\varepsilon}_{ij}$ are the components of the deviatoric strain rate tensor, G is the shear modulus, η is the effective viscosity, t is the numerical time step, σ_{ij}^{o} are the stress tensor components from the previous time step and J_{ij} includes all the corresponding terms resulting from the Jaumann rate of the stress tensor (e.g. Beuchert and Podladchikov, 2010).

The rheological model is based on the additive decomposition of the deviatoric strain rate tensor $\dot{\varepsilon}_{ij}$:

$$\dot{\varepsilon}_{ij} = \dot{\varepsilon}_{ij}^{\mathrm{el}} + \dot{\varepsilon}_{ij}^{\mathrm{pl}} + \dot{\varepsilon}_{ij}^{\mathrm{dis}} + \dot{\varepsilon}_{ij}^{\mathrm{dif}} + \dot{\varepsilon}_{ij}^{\mathrm{Pei}}. \tag{3.4}$$

where $\dot{\varepsilon}_{ij}^{\mathrm{el}}$, $\dot{\varepsilon}_{ij}^{\mathrm{pl}}$, $\dot{\varepsilon}_{ij}^{\mathrm{dis}}$, $\dot{\varepsilon}_{ij}^{\mathrm{dif}}$ and $\dot{\varepsilon}_{ij}^{\mathrm{Pei}}$ correspond to the strain rate contributions arising from elasticity, plasticity and viscous creep (dislocation, diffusion and Peierls), respectively. This strain rate equation is nonlinear and solved locally on cell centroids and vertices in order to define the current effective viscosity and stress (e.g. Popov and Sobolev, 2008). The viscosity, for any kind of creep, is formulated as a function of the corresponding strain rate invariant.

The viscosity for diffusion and dislocation creep is

$$\eta^{\mathrm{X}} = (FAd^m)^{-\frac{1}{n}} \left(\dot{\varepsilon}_{\mathrm{II}}^{\mathrm{X}}\right)^{\frac{1}{n}-1} \exp\left(\frac{Q}{nRT}\right) \tag{3.5}$$

where either X = dif or X = dis.

$$F = 2^{n-1} 3^{\frac{n+1}{2}} \tag{3.6}$$

is a geometry factor, needed to convert flow law parameters from axial compression experiments into an invariant form (e.g. Gerya, 2009). The other parameters are displayed and explained in Table S1.

Peierls creep (i.e. low-temperature plasticity) is applied in both the lithospheric and asthenospheric mantle, using the approach from Kameyama et al. (1999):

$$\eta^{\mathrm{Pei}} = F_{\mathrm{Pei}} A \left(\dot{\varepsilon}_{\mathrm{II}}^{\mathrm{Pei}}\right)^{\frac{1}{S_{(T)}}-1} \exp\left(\frac{Q}{RT}\frac{(1-\gamma)^q}{S_{(T)}}\right)\gamma\sigma_{\mathrm{P}}, \tag{3.7}$$

where an effective stress exponent that depends on the temperature is

$$S_{(T)} = 2\gamma\frac{Q}{RT}(1-\gamma), \tag{3.8}$$

and

$$F_{\mathrm{Pei}} = 2^{\frac{1-S_{(T)}}{S_{(T)}}} 3^{-\frac{1+S_{(T)}}{2S_{(T)}}} \tag{3.9}$$

is the geometry factor, specific for the presented Peierls formulation. For the rest of the parameters see Table S1.

The stress of all material phases is limited by a yield stress, τ_{y}, defined by the Drücker–Prager criterion:

$$\tau_{\mathrm{y}} = C\cos(\phi) + P\sin(\phi). \tag{3.10}$$

In case of yielding, the effective viscosity is iteratively reduced until the corresponding stress invariant equals the yield stress (e.g. Lemiale et al., 2008; Schmalholz and Maeder, 2012). Therefore, the effective viscosity for plasticity is computed only for $\tau_{\mathrm{II}} \geq \tau_{\mathrm{y}}$ and takes the form of:

$$\eta^{\mathrm{pl}} = \frac{\tau_{\mathrm{y}}}{2\dot{\varepsilon}_{\mathrm{II}}^{\mathrm{pl}}}. \tag{3.11}$$

At the end of the local iteration cycle, the effective viscosity is equal to the quasi-harmonic mean of the viscosities of each dissipative deformation mechanism:

$$\eta_{\mathrm{eff}} = \left(\frac{1}{\eta^{\mathrm{dis}}} + \frac{1}{\eta^{\mathrm{dif}}} + \frac{1}{\eta^{\mathrm{Pei}}} + \frac{1}{\eta^{\mathrm{pl}}}\right)^{-1} \tag{3.12}$$

The applied 2-D equation for heat transfer is:

$$\rho C_p \frac{dT}{dt} = \frac{\partial}{\partial x_i}\left(k\frac{\partial T}{\partial x_i}\right) + Q_{\mathrm{SH}} + Q_{\mathrm{R}}, \tag{3.13}$$

where Q_{R} is the radiogenic heat production and $Q_{\mathrm{SH}} = (\tau_{11}^2 + \tau_{22}^2 + 2\tau_{12}^2)/2\eta$ is the heat production due to viscous and plastic dissipative work. In this study we assume that all dissipative work is converted into heat (i.e. the so-called Taylor–Quinney coefficient is 1).

References

Beuchert, M. J. and Y. Y. Podladchikov
2010. Viscoelastic mantle convection and lithospheric stresses. *geophysical Journal international*, 183(1):35–63.

Carter, N. L. and M. C. Tsenn
1987. Flow properties of continental lithosphere. *Tectonophysics*, 136(1-2):27–63.

Gerya, T.
2009. *Introduction to numerical geodynamic modelling.* Cambridge University Press.

Hirth, G. and D. Kohlstedt
2003. Rheology of the upper mantle and the mantle wedge: A view from the experimentalists. *Inside the subduction Factory*, Pp. 83–105.

Kameyama, M., D. A. Yuen, and S.-I. Karato
1999. Thermal-mechanical effects of low-temperature plasticity (the peierls mechanism) on the deformation of a viscoelastic shear zone. *Earth and Planetary Science Letters*, 168(1-2):159–172.

Lemiale, V., H.-B. Mühlhaus, L. Moresi, and J. Stafford
2008. Shear banding analysis of plastic models formulated for incompressible viscous flows. *Physics of the Earth and Planetary Interiors*, 171(1-4):177–186.

Mackwell, S., M. Zimmerman, and D. Kohlstedt
1998. High-temperature deformation of dry diabase with application to tectonics on venus. *Journal of Geophysical Research: Solid Earth*, 103(B1):975–984.

Popov, A. and S. Sobolev
2008. Slim3d: A tool for three-dimensional thermomechanical modeling of lithospheric deformation with elasto-visco-plastic rheology. *Physics of the Earth and Planetary Interiors*, 171(1-4):55–75.

Ranalli, G.
1995. *Rheology of the Earth*. Springer Science & Business Media.

Schmalholz, S., Y. Podladchikov, and D. Schmid
2001. A spectral/finite difference method for simulating large deformations of heterogeneous, viscoelastic materials. *Geophysical Journal International*, 145(1):199–208.

Schmalholz, S. M., T. Duretz, G. Hetényi, and S. Medvedev
2018. Distribution and magnitude of stress due to lateral variation of gravitational potential energy between indian lowland and tibetan plateau. *Geophysical Journal International*, 216(2):1313–1333.

Schmalholz, S. M. and X. Maeder
2012. Pinch-and-swell structure and shear zones in viscoplastic layers. *Journal of Structural Geology*, 37:75–88.

Table S1 – Table and list of model parameters, where A is the pre-exponential factor, n is the power-law exponent, Q is the activation energy, V is the activation volume, λ is the thermal conductivity, d is the grain size, m is the grain-size exponent, σ_{P} is Peierls stress, q is the Peierls exponent, ρ_{ref} is the density at reference pressure ($P_{\mathrm{ref}} = 0$ Pa) and temperature ($T_{\mathrm{ref}} = 0$ °C), Q_{R} is the radioactive heat production. Some parameters have constant values: $C_p = 1050$ J.K^{-1} is the heat capacity, $G = 2 \times 10^{10}$ Pa is the shear modulus, $\alpha = 3 \times 10^{5}$ K^{-1} is the thermal expansion coefficient, $\beta = 10^{-11}$ Pa^{-1} is the compressibility, $C = 10^{7}$ [Pa] is the cohesion, $\phi = 30^{\mathrm{o}}$ is the friction angle, and $\gamma = 0.1$ is an adjustable constant. The effective pre-exponent ($A_{\mathrm{eff}} = FAd^{m}$) is used for the temperature prediction ('A' in equation 1 of the main text). For the crust, the conductivities (λ), used for model (1) are displayed and the conductivities used for models (2) and (3) are in the parentheses. For the mantle, the lithospheric conductivities are displayed and the asthenospheric conductivities are in the parentheses. Sources of rheological parameters: [1] wet quartzite (Ranalli, 1995), [2] westerly granite (Carter and Tsenn, 1987), [3] Maryland diabase (Mackwell et al., 1998), [4] dry olivine (Hirth and Kohlstedt, 2003), [5] dry olivine (Kameyama et al., 1999). The erosional diffusivity for modelling the surface evolution with a linear diffusion equation is $D = 3 \times 10^{-5}$ m^2.s^{-1}.

Lithology	A [Pa$^{-\mathrm{n}}$m^{-m}s^{-1}]	n	Q [J.mol^{-1}]	V [m^3.mol^{-1}]	λ [W.m^{-1}K^{-1}]	d [m]	m	σ_{P} [Pa]	q	ρ_{ref} [kg.m^{-3}]	Q_{R} [W.m^{-3}]
Sediments[1]	5.07×10^{-18}	2.3	1.54×10^{5}	0	2.40	-	0	-	0	2800	0.8×10^{-6}
Upper crust[2]	3.16×10^{-26}	3.3	1.87×10^{5}	0	2.40 (2.25)	-	0	-	0	2800	1.47×10^{-6}
Lower crust[3]	5.05×10^{-28}	4.7	4.85×10^{5}	0	2.40 (2.25)	-	0	-	0	2900	1.47×10^{-6}
Mantle$_{\mathrm{dis}}$ [4]	1.10×10^{-16}	3.5	5.30×10^{5}	1.4×10^{-5}	2.25 (41.25)	-	0	-	0	3350	2.11×10^{-10}
Mantle$_{\mathrm{dif}}$ [4]	1.50×10^{21}	1.0	3.75×10^{5}	8.0×10^{-6}	2.25 (41.25)	10^{-3}	-3	-	0	3350	2.11×10^{-10}
Mantle$_{\mathrm{Pei}}$ [5]	5.7×10^{11}	-	5.36×10^{5}	0	2.25 (41.25)	-	0	8.5×10^{9}	2	3350	2.11×10^{-10}

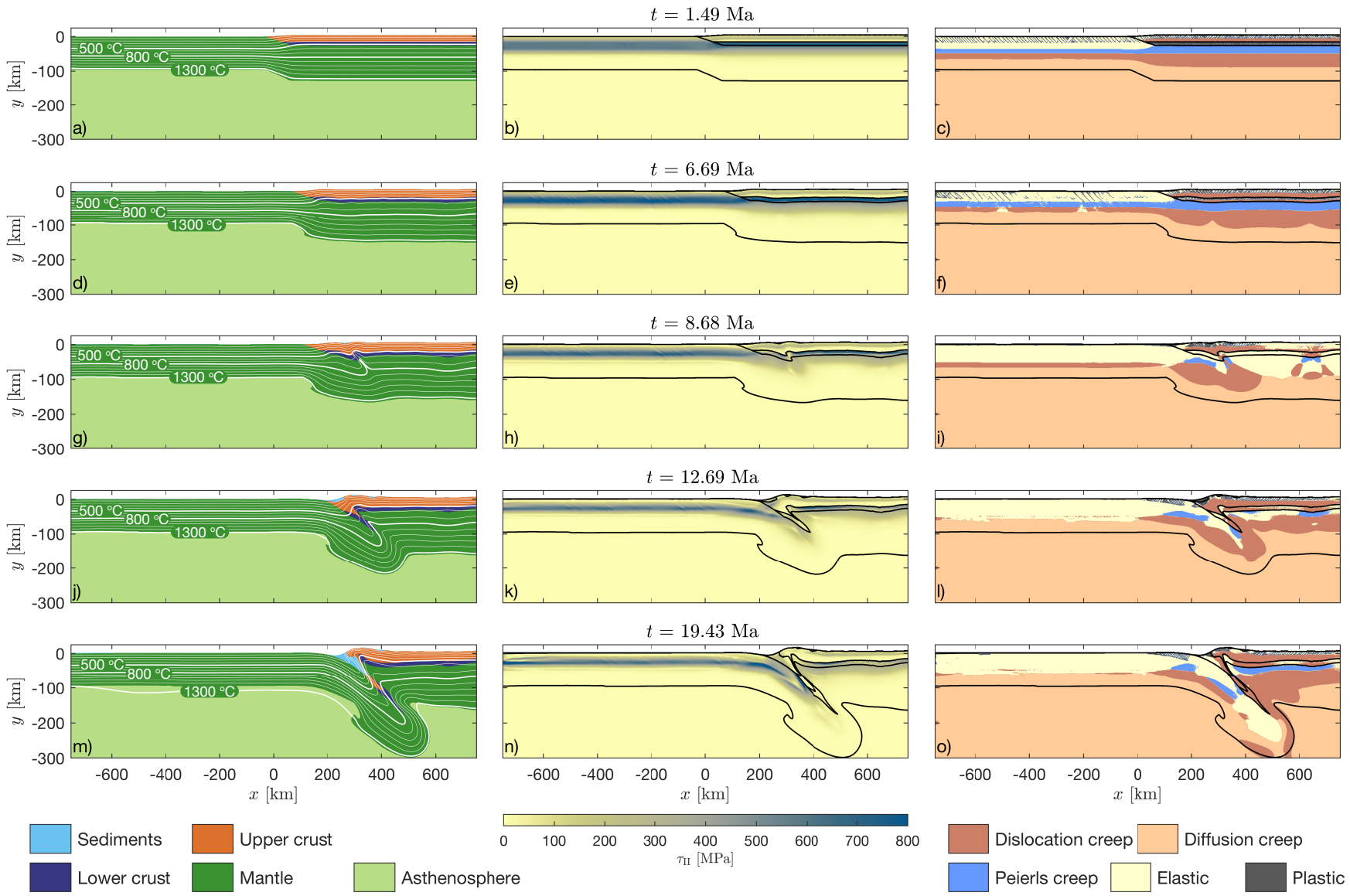

Figure S1 – Evolution of model geometry (left column), stress field (middle column) and distribution of dominant deformation mechanism (right column) for simulation (1). Left column: White lines indicate isotherms every 100 °C and colored field indicate different model units; see legend below left column. Middle column: Stress is quantified with the second invariant of deviatoric stress tensor. Black lines indicate from bottom to top: lithosphere-asthenosphere boundary, Moho and upper-lower crust boundary. Right column: The dominant deformation mechanism is the one corresponding to the largest strain rate contribution (see equation 3).

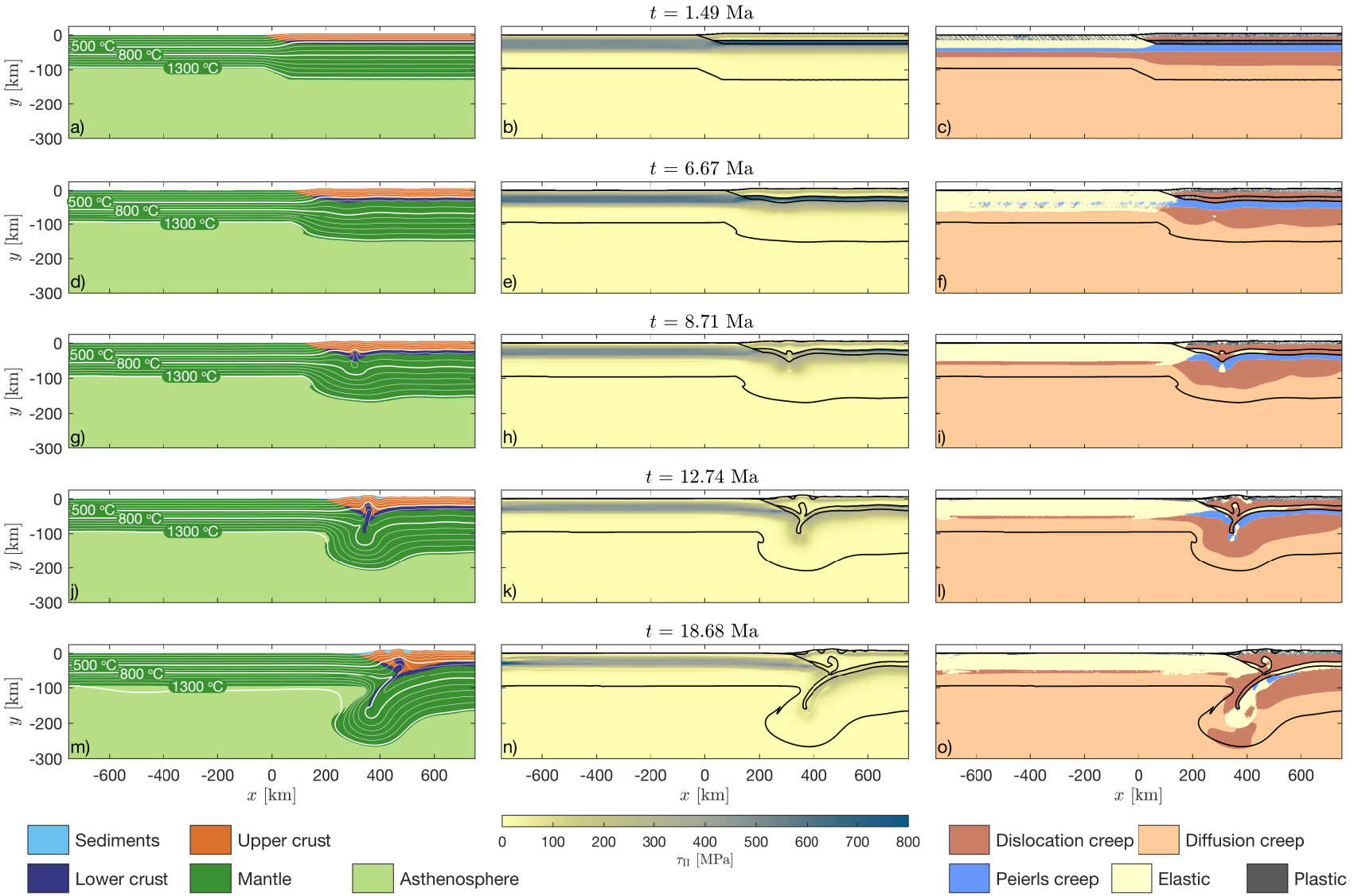

Figure S2 – Evolution of model geometry (left column), stress field (middle column) and distribution of dominant deformation mechanism (right column) for simulation (2). Left column: White lines indicate isotherms every 100 °C and colored field indicate different model units; see legend below left column. Middle column: Stress is quantified with the second invariant of deviatoric stress tensor. Black lines indicate from bottom to top: lithosphere-asthenosphere boundary, Moho and upper-lower crust boundary. Right column: The dominant deformation mechanism is the one corresponding to the largest strain rate contribution (see equation 3).

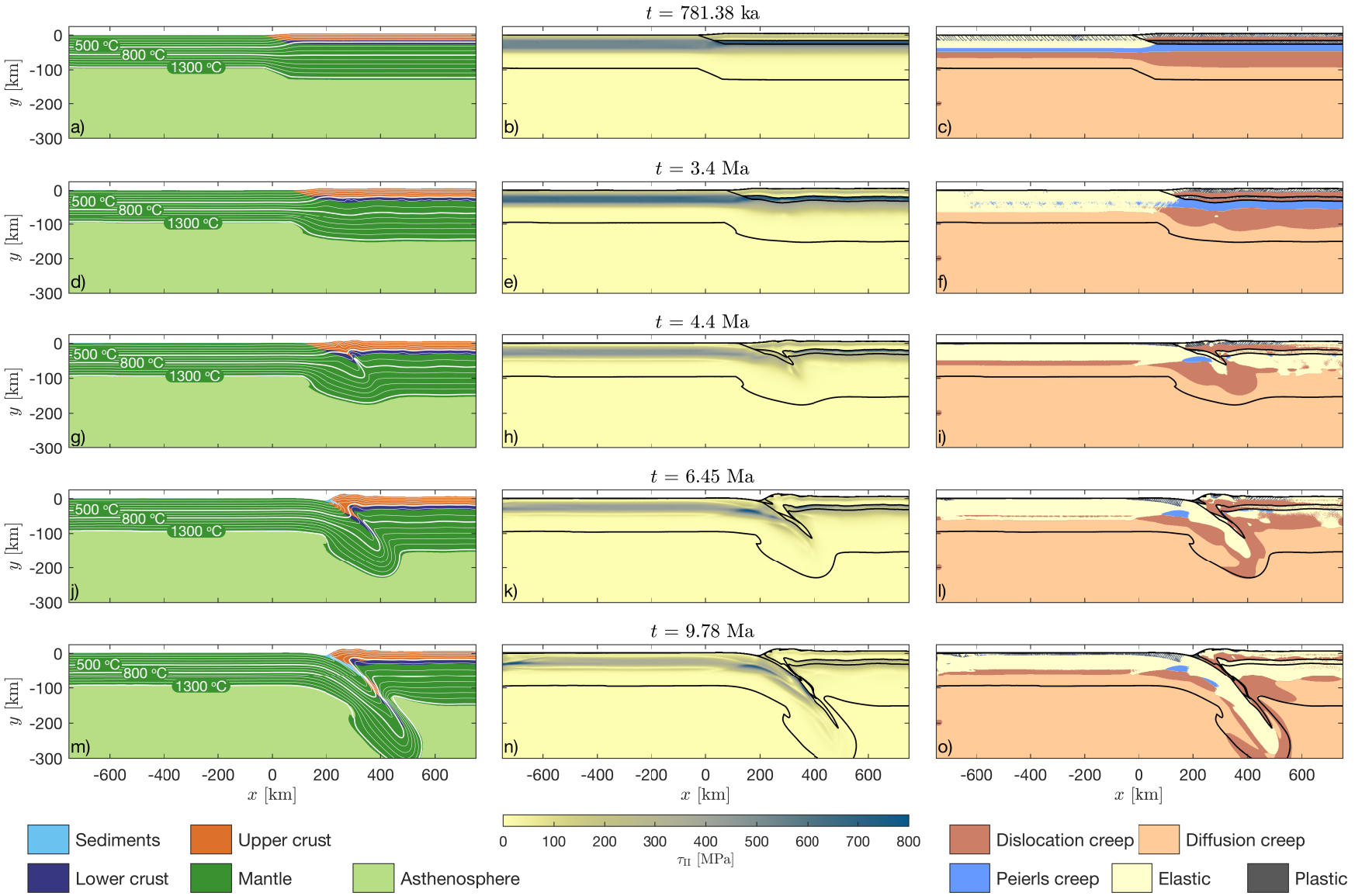

Figure S3 – Evolution of model geometry (left column), stress field (middle column) and distribution of dominant deformation mechanism (right column) for simulation (3). Left column: White lines indicate isotherms every 100 °C and colored field indicate different model units; see legend below left column. Middle column: Stress is quantified with the second invariant of deviatoric stress tensor. Black lines indicate from bottom to top: lithosphere-asthenosphere boundary, Moho and upper-lower crust boundary. Right column: The dominant deformation mechanism is the one corresponding to the largest strain rate contribution (see equation 3).

CHAPTER 4

Towards a nappe theory: Thermo-mechanical simulations of nappe detachment, transport and stacking in the Helvetic Nappe System, Switzerland

Dániel Kiss, Thibault Duretz and Stefan M. Schmalholz

Under review in *Solid Earth Discussions*, se-2019-130

Abstract

Tectonic nappes are observed for more than a hundred years. Although geological studies often refer to a "nappe theory", the physical mechanisms of nappe formation are still incompletely understood. We apply two-dimensional numerical simulations of shortening of a passive margin, to investigate the thermo-mechanical processes of detachment, transport and stacking of nappes. We use a visco-elasto-plastic model with standard creep flow laws and Drucker-Prager yield criterion. We consider tectonic inheritance with two initial mechanical heterogeneities: (1) lateral heterogeneity of the basement-cover interface due to half-grabens and horsts and (2) vertical heterogeneities due to layering of mechanically strong and weak sedimentary units. The model shows detachment and horizontal transport of a thrust nappe and stacking of this thrust nappe above a fold nappe. The detachment of the thrust sheet is triggered by stress concentrations around the sediment-basement contact and the resulting brittle-plastic shear band formation. The horizontal transport is facilitated by a basal shear zone just above the basement-cover contact, composed of thin, weak sediments. Fold nappe formation occurs by a dominantly ductile closure of a half-graben and the associated extrusion of the half-graben fill. We apply our model to the Helvetic nappe system in Western Switzerland, which is characterized by stacking of the Wildhorn thrust nappe above the Morcles fold nappe. The modeled structures and temperature field agree with data from the Helvetic nappe system. The mechanical heterogeneities must generate contrasts in effective viscosity (i.e. ratio of stress to strain rate) of four orders of magnitude to model nappe structures similar to the ones of the Helvetic nappe system.

4.1 Introduction

Tectonic nappes were discovered more than a hundred years ago and are considered as typical tectonic features of orogenic belts (e.g. Price and McClay, 1981), particularly in the Alps (e.g. Lugeon, 1902; Termier, 1906; Argand, 1916; Tollmann, 1973; Trümpy, 1980; Escher et al., 1993; Pfiffner, 2014). Several definitions of a nappe have been proposed (see discussion in Price and McClay, 1981), for example, a basic definition modified after Termier (1922) is: "A nappe is a rock packet not in its place, resting on a substratum that is not its original one". Two end-member types of nappes are commonly distinguished, namely fold nappes and thrust nappes, or thrust sheets (e.g. Termier, 1906; Price and McClay, 1981; Epard and Escher, 1996). Fold nappes are recumbent folds exhibiting large-scale stratigraphic inversion, typically with amplitudes that are exceeding several kilometers. In contrast, thrust sheets are allochtonous sheets with a prominent shear zone or thrust at their base, but without a prominent overturned limb. The importance of tectonic nappes for orogeny, especially for collisional orogens, is nowadays well established and many geological studies refer to a "nappe theory" when mentioning tectonic nappes. However, the physical mechanisms of nappe detachment, transport and stacking are still incompletely understood.

We focus here on the Helvetic nappe system in Western Switzerland (see next section for a geological overview), which is one of the birthplaces of the concept of tectonic nappes. Arnold Escher mentioned a nappe (he used "Decke" in german) and a colossal overthrust ("colossale Überschiebung") in 1841 during the presentation of a geological map of the

canton Glarus, Eastern Switzerland (Escher von der Linth, 1841). Escher did not dare to publish his interpretation, but explained it in the field to Roderick Murchinson, who published the overthrust interpretation in 1849 (Murchison, 1849), crediting Escher for the original observation. Bertrand (1884) argued also convincingly for an overthrust nappe (he used "masse de recouvrement" and "lambeaux de recouvrement" instead of nappe) in the Glarus region so that finally also Heim (1906) accepted the overthrust interpretation instead of the earlier preferred double-fold interpretation ("Überschiebungsfalte" instead of "Doppelfalte"). Although the important controversies and observations supporting tectonic nappes are related to the Glarus region, which is part of the Helvetic nappe system, the true birth date of the nappe concept in the Alps, according to Trümpy (1991), is the publication by Schardt (1893) who worked in the Prealps, belonging to the Penninic domain (e.g. Escher et al., 1993). Schardt (1893) realized that Jurassic breccias have been thrust over Tertiary flysch and that large regions of the Prealps have been actually emplaced as a major overthrust. After decades of controversy, the existence of nappes got generally accepted approximately a century ago, revolutionizing Tectonics, Alpine Geology and orogeny in general (for historical reviews see Bailey 1935; Masson 1976; Merle 1998; Trumpy 1991; Dal Piaz 2001; Schaer 2010).

Since then, a considerable effort has been made in mapping the present-day structure of the Helvetic nappe system (e.g. Steck, 1999; Pfiffner et al., 2011). Structural and paleogeographic reconstructions have provided a valuable insight into the kinematics of nappe formation (e.g. Gillcrist et al., 1987; Epard and Escher, 1996; Herwegh and Pfiffner, 2005; Bellahsen et al., 2012; Boutoux et al., 2014). Therefore, the geometrical structure and kinematic evolution of the Helvetic nappe system is reasonably well understood. There are also theoretical and analogue modeling studies investigating the formation of fold-and-thrust belts and nappes (e.g. Bucher, 1956; Rubey and King Hubbert, 1959; Dietrich and Casey, 1989; Merle, 1989; Casey and Dietrich, 1997; Wissing and Pfiffner, 2003; Bauville et al., 2013; Poulet et al., 2014; Erdős et al., 2014; Jaquet et al., 2014; Ruh et al., 2014; Bauville and Schmalholz, 2017). However, the controlling physical processes of nappe detachment, transport and stacking, and the associated dominant rock deformation mechanism are still incompletely understood and, therefore, the frequently mentioned "nappe theory" is not complete. For example, for fold nappes, many interpretations favor distributed shearing and dominantly ductile deformation mechanisms, such as dislocation or grain-size sensitive diffusion creep (e.g. Ramsay et al., 1983; Gillcrist et al., 1987; Ebert et al., 2008; Bauville et al., 2013). However, there are also interpretations arguing for localized thrusting and dominantly brittle-plastic deformation mechanisms, such as fracturing related to fluid pressure (e.g. Boyer and Elliott, 1982; Granado and Ruh, 2019). Furthermore, the presumed driving forces of nappe transport are either external surface forces, due to tectonic compression, or internal body forces, due to gravity. Heterogeneous shearing due to buttressing in a general compressional regime is an example of deformation driven by external forces (e.g. Ramsay et al., 1983; Epard, 1990; Bauville et al., 2013; Boutoux et al., 2014). Gravity gliding and spreading is an example of deformation driven by body forces (e.g. Durney, 1982; Merle, 1989; Merle and Guillier, 1989).

For thrust sheets, the variety of the proposed emplacement mechanisms is even larger than for fold nappes (see for an overview Merle, 1998). The apparently straightforward interpretation that thrust sheet transport is controlled by frictional sliding is problematic, because stresses required to move a long sheet over a frictional surface exceed the strength of the rock sheet so that the sheet would break into smaller pieces (e.g. Smoluchowski, 1909; King Hubbert and Rubey, 1959; Price and Cosgrove, 1990). This problem is known as the overthrust paradox (e.g. Smoluchowski, 1909; King Hubbert and Rubey, 1959). Several solutions for this paradox were proposed, such as (1) reduction of the effective stress due to pore fluid pressure causing a reduction of the effective friction angle (e.g. King Hubbert and Rubey, 1959; Rubey and King Hubbert, 1959), (2) if the majority of the displacement happens during fast slip events, like on the Main Frontal Thrust of the Himalayas, (e.g. Avouac et al., 2015; Wang and Fialko, 2015), dynamic frictional weakening can reduce significantly the shear stresses (e.g. Scholz, 1998; Aharonov and Scholz, 2018; Di Toro et al., 2011), or (3) a dominantly ductile deformation mechanism (e.g. Smoluchowski, 1909; Goguel, 1948; Voight, 1976), presumably in combination with thermally-, chemically- or mechanically-activated softening mechanisms (e.g. Poirier, 1980; Ebert et al., 2008; Poulet et al., 2014). Another problem of purely brittle-frictional interpretations, assuming homogeneous material properties, is that thrust sheets have often been displaced over tens of kilometers on sub-horizontal thrust planes or shear zones. However, according to Anderson's theory of faulting (e.g. Turcotte and Schubert, 2014) thrust planes for friction angles of ca 30 degrees should dip with ca 30 degrees with respect to the horizontal, if the smallest principal stress, σ_3, is approximately vertical. Smaller friction angles would increase the dip angle. For example, for zero friction angle, corresponding to a constant, pressure-insensitive yield stress, the dip angle would be 45 degrees. Therefore, prominent low-angle thrust planes are likely controlled by mechanical heterogeneities, such as the orientation of the basement-cover interface and of mechanically weak shale-rich or evaporite layers, as has been suggested for the Hevetic nappe system (e.g. Pfiffner, 1993; Steck, 1999; Pfiffner et al., 2011; Bauville and Schmalholz, 2017).

To make another step towards a "nappe theory" that explains the physical process of nappe formation, we investigate the detachment, transport and stacking of nappes with two-dimensional (2D) numerical simulations based on continuum mechanics. To keep the model relatively simple and transparent, we focus here on thermo-mechanical processes on the macro-scale, larger than the typical size of mineral grains. Hence, we do not consider hydro-chemical couplings, such as fluid release by carbonate decomposition (e.g. Poulet et al., 2014), and micro-scale processes, such as micro-structural evolution with secondary phases (e.g. Herwegh et al., 2011). The numerical algorithm is based on the finite difference method. We consider a standard visco-elasto-plastic deformation behavior, heat transfer and thermo-mechanical coupling by shear heating and temperature-dependent viscosities. We also apply velocity boundary conditions that are standard for modeling accretionary or orogenic wedges (e.g. Buiter et al., 2006). For the comparison between model results and natural observations, we consider a geological section across the Helvetic Nappe System in Western Switzerland. This section is characterized by two deformed basement mas-

sifs, the Aiguilles-Rouges and Mont-Blanc massifs, a fold nappe, the Morcles nappe, and a thrust nappe, the Wildhorn super-nappe, that has been overthrust, or stacked, above the underlying fold nappe (Fig. 4.1). In our models, we consider the tectonic inheritance of the Mesozoic passive margin formation in the form of simple half-grabens and horsts, because the Helvetic nappe system resulted from the inversion of the pre-Alpine European passive margin (e.g. Trümpy, 1980). We consider two main orientations of inherited mechanical heterogeneities: (1) a lateral variation of mechanical strength due to the lateral alternation of basement and sediments associated with the half-graben structure and (2) a vertical variation of strength due to (i) the basement-cover interface, (ii) the alternation of strong carbonate with weak shale-rich units (so-called mechanical stratigraphy after Pfiffner (1993)) and (iii) the pressure and temperature sensitivity of rock strength and effective viscosity, respectively.

The main aim of this study is to show that a thermo-mechanical model based on the theory of continuum mechanics (i) with a well established visco-elasto-plastic deformation behaviour using standard flow laws, (ii) with mechanical heterogeneities mimicking pre-Alpine extensional heritage and stratigraphic layering and (iii) with a wedge-type compressional configuration can self-consistently explain the first-order features of nappe detachment, transport and stacking in the Helvetic nappe system.

4.2 Short overview of the Helvetic Nappe System in Western Switzerland

The Helvetic nappe system is commonly subdivided into Infrahelvetic, Helvetic and Ultrahelvetic units (Fig. 4.1c) (e.g. Masson et al., 1980; Escher et al., 1993; Pfiffner et al., 2011). The nappes consist mainly of Jurrasic to Paleogen sediments that were deposited on the Mesozoic European passive margin before the Alpine orogeny (Fig. 4.1a). This passive margin inherited half-grabens and horsts from the Mesozoic, pre-Alpine extensional phase (e.g. Masson et al., 1980; Escher et al., 1993). The stratigraphy of the nappes is generally characterized by shale-rich units, totaling several kilometers in thickness, and two major units of massive platform carbonates, the so-called Quinten (Malm) and Urgonian (Lower Cretaceous) limestones, with a thickness of several hundred meters (e.g. Masson et al., 1980; Pfiffner, 1993; Pfiffner et al., 2011).

In the studied section, along the Rhone-valley near Martigny (Switzerland), the Infrahelvetic units form the Morcles fold nappe (e.g. Steck, 1999). This recumbent fold nappe is strongly deformed, but is still connected to its original position of deposition, the Mesozoic half-graben between the Aiguilles-Rouges and the Mont-Blanc massifs (Fig. 4.1a). Therefore, the Morcles nappe is considered as a parautochtonous unit and its root zone, between the Aiguilles-Rouges and the Mont-Blanc massifs, is termed the Chamonix zone (Fig. 4.1c). The sediments forming the Helvetic nappes have been deposited on more distal regions of the European passive margin than the units forming the Morcles nappe. The original regions of deposition of the Infrahelvetic and the Helvetic units have been separated by a horst, or basement high (Fig. 4.1a). The Helvetic nappes have been

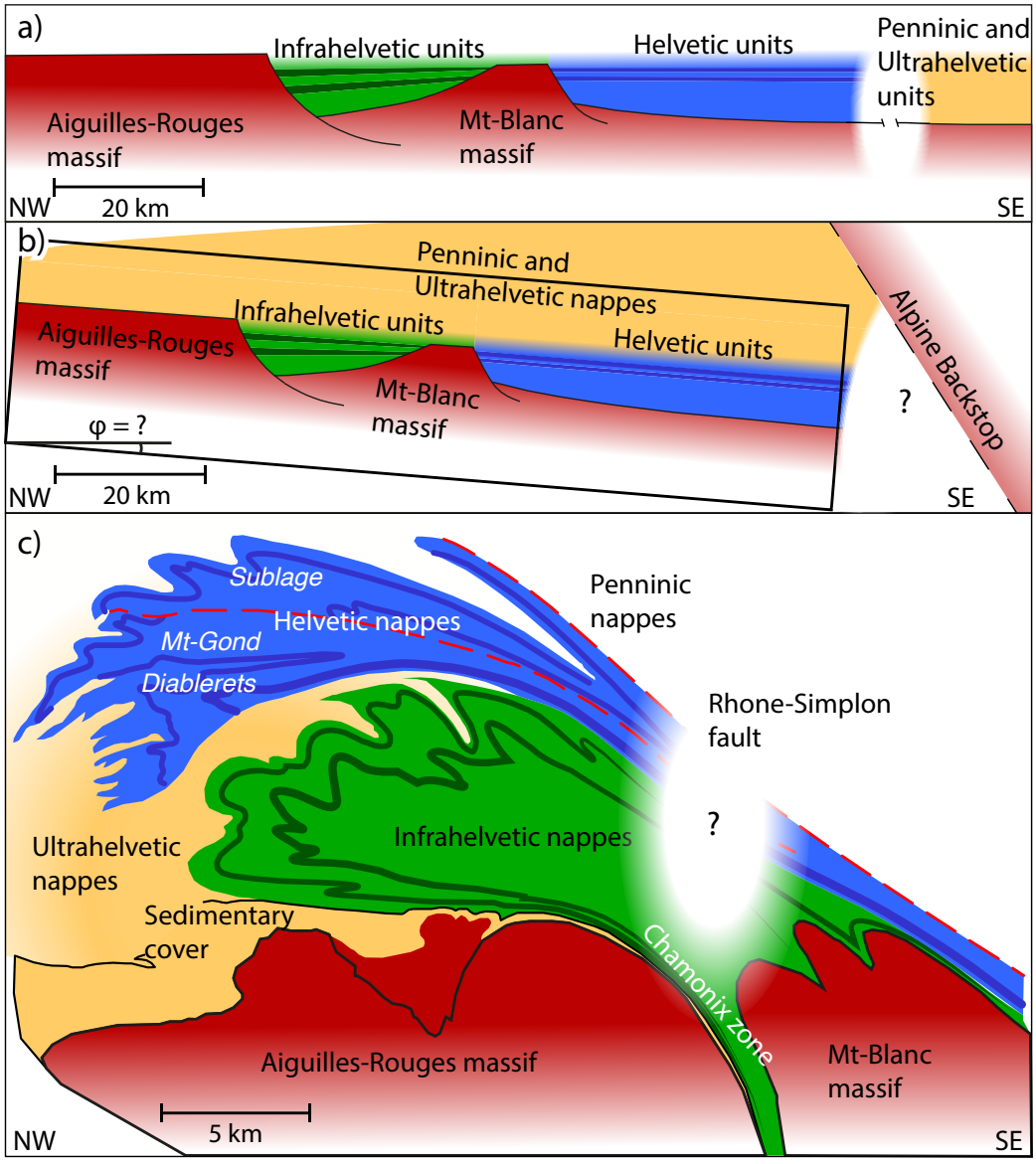

Figure 4.1 – a) Simplified geological reconstruction of the Mesozoic, pre-Alpine European passive margin. b) Simplified geological reconstruction of the Alpine orogenic wedge, after emplacement of the Penninic and Ultrahelvetic units and before the Helvetic nappe stacking. The black rectangle represents the model domain of the numerical simulations. c) Simplified geological reconstruction of the present day structure of the Helvetic Nappe System.

thrust above the Infrahelvetic units. In the studied region, the Helvetic nappe is termed the Wildhorn super-nappe that can be subdivided into the Diablerets, Mont Gond and Sublage nappes (Fig. 4.1c; Escher et al. (1993)). Due to the Rhone valley associated with the Rhone-Simplon fault, the Helvetic nappes cannot be continuously traced back to their original position of deposition (Fig. 4.1c). The Ultrahelvetic units have been depositied on more distal regions than the Helvetic units (Fig. 4.1a). Today, the Ultrahelvetic units are found in front and between the Morcles and Wildhorn nappes (Fig. 4.1c).

During the Alpine continental collision, the Ultrahevetic units and the Penninic nappes, originating from more distal positions, have been thrust above the original deposition regions of the sediments forming today the Morcles and Wildhorn nappes (Fig. 4.1b)

(e.g. Epard and Escher, 1996). These sediments were subsequently sheared off from their original position of deposition and were transported several tens of kilometers towards the foreland, i.e. top to the northwest transport direction (e.g. Epard and Escher, 1996; Ebert et al., 2007). The present day nappe structure represents a thick-skinned tectonic style because the crystalline basement of the Aiguilles-Rouges and Mont-Blanc massifs exhibits significant deformation (Fig. 4.1c).

The above tectonic scenario is supported by peak metamorphic temperatures of the Helvetic nappe system, which range between 250-385 °C (Kirschner et al., 1996, 1995; Ebert et al., 2007, 2008) increasing structurally downwards and towards the root zone. The maximal depth of burial of the Morcles nappe has most likely exceeded 10 km and was achieved between 29 Ma and 24 Ma (Fig. 4.1b) (Kirschner et al., 1996, 1995). In the studied section, the carbonate layers are strongly folded indicating significant internal deformation of the nappes (Fig. 4.1c). The Morcles fold nappe is characterized by strong parasitic folding in its frontal part and by a ca 20 km long, highly stretched inverse limb. The Wildhorn super-nappe also exhibits significant internal deformation, such as the isoclinal fold separating the Diablerets and Mont Gond nappes (Fig. 4.1c). These observations indicate that in the studied region ductile deformation was significant during formation of the nappes.

4.3 Methods

4.3.1 Mathematical model

Our mathematical model is based on the concept of continuum mechanics (e.g. Mase and Mase, 1970; Turcotte and Schubert, 2014). We assume slow, incompressible deformation under gravity so that inertial forces are negligible. Our model accounts for heat transfer by conduction and advection, as well as heat generation by viscous dissipation and by radioactive heating. Heat transfer and deformation are coupled by shear heating, that is, dissipative deformation is converted into heat to conserve energy. The governing system of partial differential equations is solved numerically. The applied equations are described in detail in Schmalholz et al. (2019). The applied numerical algorithm is based on the finite-difference/marker-in-cell method (e.g. Gerya and Yuen, 2003). The diffusive terms in the force balance and heat transfer equations are discretized on an Eulerian staggered grid while advection and rotation terms are treated explicitly using a set of Lagrangian markers and a 4th order in space / 1st order in time Runge-Kutta scheme. The topography in the model is a material interface defined by a Lagrangian marker chain and this interface is displaced with the numerically calculated velocity field (Duretz et al., 2016). With ongoing deformation, this marker chain needs to be locally remeshed which is achieved by adding marker points in the deficient chain segments.

We consider a visco-elasto-plastic deformation behavior and assume a power-law, Maxwell, viscoelastic model and Drucker-Prager yield criterion (see details in Schmalholz et al., 2019). In the applied creep flow laws, we add a constant pre-factor f to vary the effective viscosities in order to test the impact of different effective viscosities on the model results.

Table 4.1 – The list of the reference model parameters, where f is a custom pre-factor, A is the pre-exponential factor, n is the power-law exponent, Q is the activation energy, λ is the thermal conductivity, ρ_{ref} is the density at reference pressure ($P_{\text{ref}} = 0$ Pa) and temperature ($T_{\text{ref}} = 0$ °C), Q_r is the radioactive heat production, C is the cohesion and ϕ is the friction angle. Some parameters have constant values: $C_p = 1050$ J.K^{-1} is the heat capacity, $G = 10^{10}$ Pa is the shear modulus, $\alpha = 3 \times 10^5$ K^{-1} is the thermal expansion coefficient, $\beta = 10^{-11}$ Pa^{-1} is the compressibility and $F = 2^{(1-n)/n} 3^{-(n+1)/(2n)}$ is a geometry factor (needed to convert flow law parameters from axial compression experiments into an invariant form). The creep flow law parameters (A, n and Q) are: [1]Westerly granite (Hansen et al., 1983), [2]calcite (Schmid et al., 1977) and [3]mica (Kronenberg et al., 1990).

Lithology	f	A [Pa^{-n}s^{-1}]	n	Q [J.mol^{-1}]	λ [W.m^{-1}K^{-1}]	ρ_{ref} [kg.m^{-3}]	Q_{r} [W.m^{-3}]	C [Pa]	ϕ [°]
Basement[1]	1.0	3.16×10^{-26}	3.3	1.87×10^5	3.0	2800	2.5×10^{-6}	10^7	30
Cover[2]	0.1	1.58×10^{-25}	4.2	4.45×10^5	2.5	2700	5×10^{-7}	10^7	30
Strong layer[2]	1.0	1.58×10^{-25}	4.2	4.45×10^5	2.5	2750	5×10^{-7}	10^7	30
Weak units[3]	1.0	1.00×10^{-138}	18.0	5.10×10^4	2.0	2700	1×10^{-6}	10^6	5

The effective viscosity is defined by the ratio of stress to (viscous) strain rate and has the form

$$\eta_{\text{eff}} = fFA^{-\frac{1}{n}} \dot{\epsilon}_{\text{II}}^{\frac{1}{n}-1} \exp\left(\frac{Q}{nRT}\right), \tag{4.1}$$

where the expression to the right of f corresponds to the effective viscosity from standard creep flow laws determined by rock deformation experiments. Material parameters, such as effective viscosities, must be indepenent from the chosen coordinate system and, therefore, the dependence on strain rate is expressed by the quantity $\dot{\epsilon}_{\text{II}}$, which is the square root of the second invariant of the (viscous) strain rate tensor. The equation for η_{eff} is given above because the magnitude and distribution of η_{eff} will be displayed for the performed simulations in the next section. All other parameters are explained and listed in Table 4.1.

4.3.2 Model configuration

The applied model configuration mimics a 200 km long section of the upper crustal region of a simplified passive margin (Fig. 4.2). We consider four model units with distinct mechanical properties, namely basement, cover, strong layer and weak unit. The basement unit represents the crystalline basement, the cover unit represents the Ultrahelvetic and Penninic nappes, the strong layer represents the major carbonate layers (Malm and Urgonian) and the weak unit represents the shale-rich units. The initial geometry of the basement unit represents the crystalline upper crust of a passive continental margin with 15 km thickness, tapering down to 5 km thickness (Fig. 4.2). The Infrahelvetic basin is represented by an idealized half-graben that is 5 km deep and 25 km wide. The Infrahelvetic and the more distal (right model side) Helvetic basin are separated by an idealized horst structure. We cover the entire passive margin structure with sediments, to obtain a total (basement + sediments) model thickness of 25 km. The model stratigraphy is consisting of three units (cover, strong layer and weak units) and each unit has homogenous material parameters. Both the half-graben and the basin are filled with weak units up to a depth of 13.5 km. On top of the weak units we place a 1.5 km thick strong layer. Our initial geometry represents the stage during the Alpine orogeny, when the proximal

passive margin region, including the Infrahelvetic and Helvetic basins, is still relatively undeformed, but the Ultrahelvetic and Penninic units have been already thrust on top of it (Fig. 4.1b). We consider the overthrust units by adding a 10 km thick, homogenous unit of cover sediments (without distinction between the Ultrahelvetic and Penninic units) on top of the model basement and basins (Fig. 4.2). Adding this 10 km thick unit is important to consider appropriately the ambient pressure and temperature, which control the brittle-plastic yield strength and the temperature dependent effective viscosities.

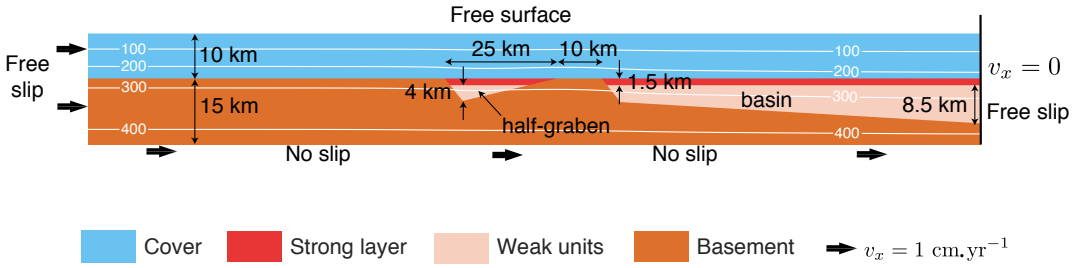

Figure 4.2 – Reference model configuration. The white contours show isotherms and the labels are the corresponding temperatures in °C.

We apply boundary conditions that are similar to sandbox experiments of fold-and-thrust belts and orogenic wedges (Fig. 4.2). The left lateral model boundary moves to the right with a constant horizontal velocity of 1 cm.yr^{-1}, while the right lateral boundary does not move horizontally. There are no shear stresses at the vertical model boundaries (i.e. free slip boundary conditions). The bottom boundary also moves with a horizontal velocity of 1 cm.yr^{-1}, but does not move vertically. This velocity boundary condition generates a velocity discontinuity at the bottom right corner of the model, which is typical for sandbox experiments and numerical simulations of accretionary wedges (e.g. Buiter et al., 2006). The top boundary is a free surface, using the algorithm of Duretz et al. (2016). We apply constant temperature boundary conditions of 10 °C at the top and 420 °C at the bottom of the model. There is no heat flux across the lateral model boundaries. We apply an initially equilibrated temperature field which results in a ca 16 °C.km^{-1} initial geothermal gradient. Applied parameters are listed in Table 4.1.

4.4 Results

We present first the main results of a reference simulation, for the configuration described above, and then results of simulations in which some parameters are varied. All simulations show some common, general features: With increasing bulk shortening, the initially flat topography is increasing most around the right model boundary, representing a "back-stop" (Fig. 4.3). The models develop a wedge shape with a topography tilting towards the left model side. With progressive shortening, the increasing topography reaches the left model boundary and the topographic slope reduces, generating again a more horizontal topography. Also, initially the basement deformation occurs around the bottom right corner and progressively propagates towards the left (Fig. 4.3). With progressive shortening the

models become generally thicker but the sedimentary units above the basement become relatively thicker than the underlying basement because the sediments are thrust above the basement. The thickened sedimentary cover results in increasing basement temperatures, hence decreasing its teperature-dependent viscosity. The temperature increase of the top of the basement is visible by the vertical position of the 300 °C isotherm in figure (4.3). Such basement temperature increase and the related shift to a thick-skinned deformation was also reported by Bauville and Schmalholz (2015) in their numerical models of fold-and-thrust belts. Basement deformation results in the partial or total closure of the half-graben and associated extrusion of the basin fill. The specific model evolution, however, depends on the applied flow laws and model stratigraphy, which will be discussed in the following in comparison with the reference simulation.

4.4.1 Reference model

We apply the configuration and parameters described in the previous section and displayed in figure 4.2 to generate a reference simulation for later comparison (Figs. 4.3 and 4.4). Initially, elastic stress builds up during a few hundred thousand years until the brittle-plastic yield stress and the steady-state ductile creep stress are reached. For the applied model configuration, the brittle-ductile transition occurs at about 6-8 km depth. We quantify deviatoric stress magnitudes with the square root of the second invariant of the deviatoric stress tensor, τ_{II}, and maximal deviatoric stresses reach ca 250 MPa at the brittle-ductile transition (Fig. 4.4). Maximal strain rates in the developing shear zones are between 10^{-13} and 10^{-12} s^{-1}, in broad agreement with strain rate estimates for natural shear zones (e.g. Pfiffner and Ramsay, 1982; Boutonnet et al., 2013; Fagereng and Biggs, 2018). The largest stresses occur around the brittle-ductile transition in the cover, whereas stresses in the basement and in the strong layer are significantly smaller (Fig. 4.4).

The model shows several key phases of the formation of a nappe stack: (1) Detachment of a sedimentary unit of the right basin, mimicking the Helvetic basin, from their original substratum (Figs. 4.3a and b, and 4.4a and c). (2) Significant horizontal transport of ca 30 km with little internal deformation indicated by the relatively undeformed strong layer in the detached unit (Figs. 4.3b to d, and 4.4b to c). (3) Formation of a fold nappe due to ductile closure of the left half-graben, mimicking the Infrahelvetic basin, and associate extrusion of the sedimentary half-graben fill (Figs. 4.3c to e). (4) Stacking of the nappe originating from the right basin above the fold nappe from the left half-graben (Figs. 4.3d and e).

During the initial stages of deformation, the strong layer of the right basin is gently folding, or buckling (Fig. 4.3a). Stress becomes concentrated around the contact of this strong layer and the basement horst (Fig. 4.5m) causing increased strain rates in this region. With progressive deformation a localized shear zone, dominated by brittle-plastic deformation, develops across the strong layer, eventually detaching it from the basement (Fig. 4.5j to l). This shear zone develops within the strong layer so that a small piece of the strong layer remains attached to the basement (Fig. 4.5t). The detachment of the strong layer causes a significant stress drop in the strong layer and the basement (Fig. 4.5m to

p). Once detached, the strong layer and parts of the underlying weak unit passively move sub-horizontally over the horst initiating the horizontal nappe transport.

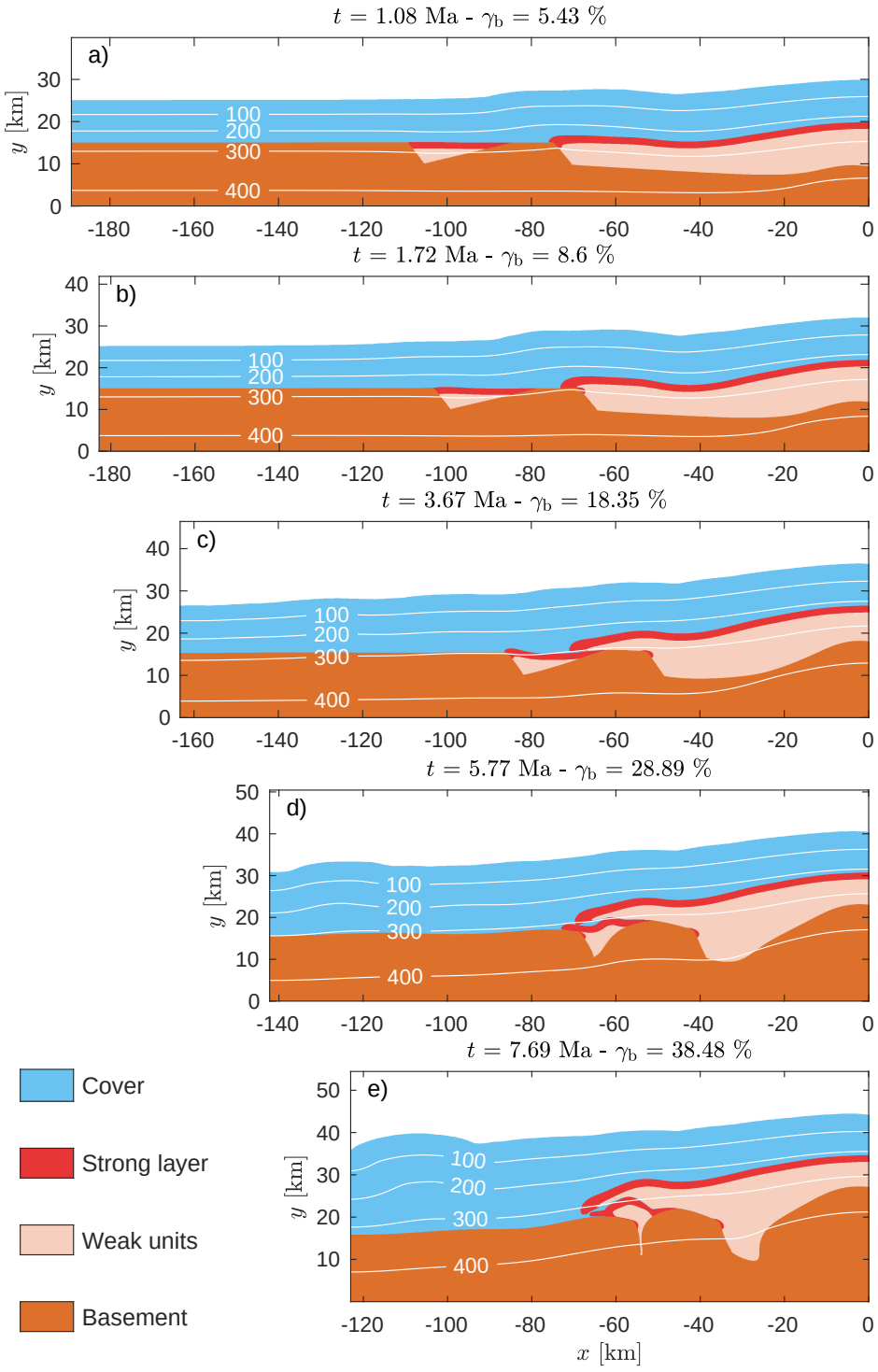

Figure 4.3 – Structural and thermal evolution of the reference model for different times, t, and bulk shortening, γ_b. The white contours show isotherms and the labels are the corresponding temperatures in °C.

Quantification of elastic strain rates shows that elastic deformation is active during the detachment process and that, hence, elastic stresses are not completely relaxed visco-plastically (Fig. 4.5e to h). During the detachment, some parts of the weak cover, originally

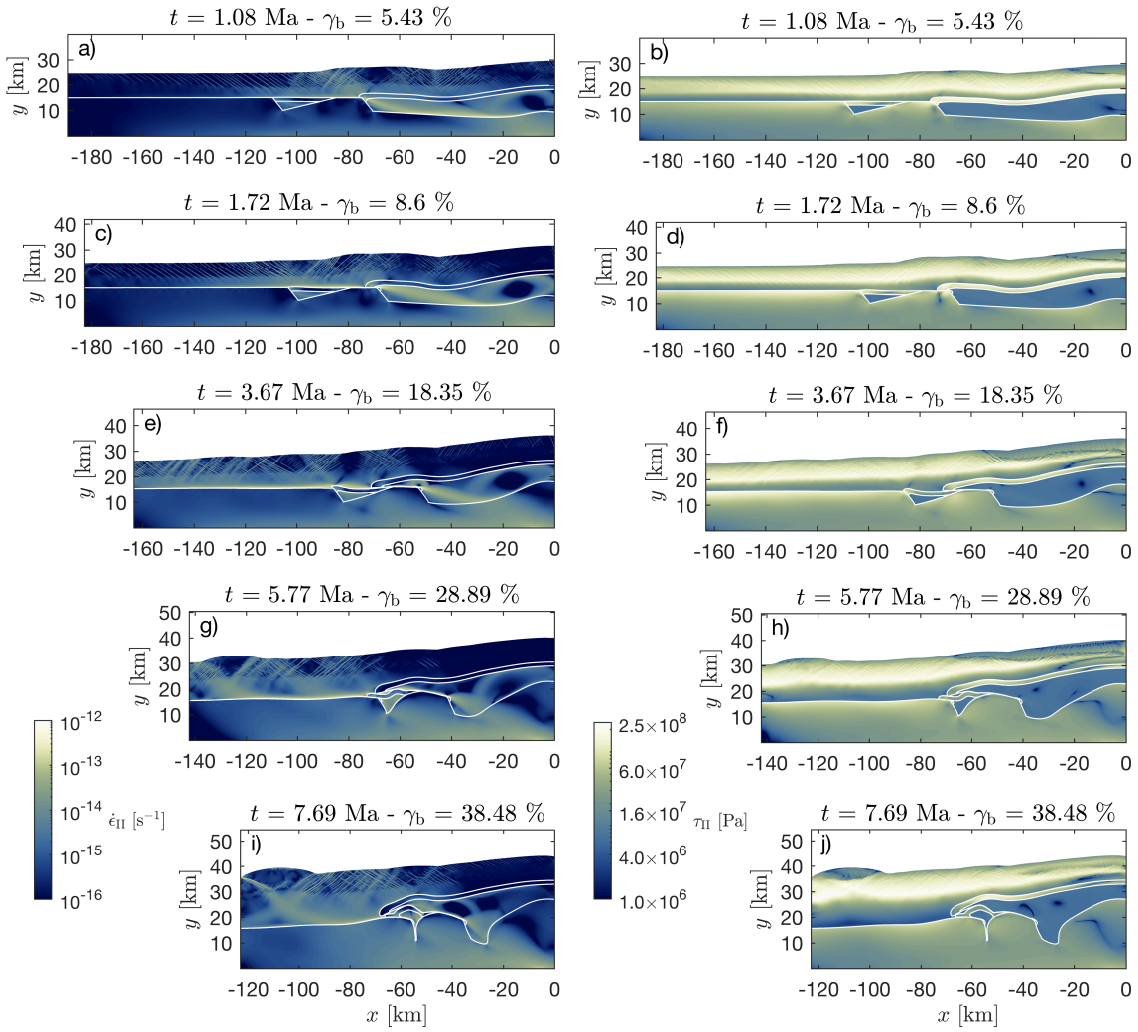

Figure 4.4 – Evolution of the strain rate (left column) and deviatoric stress (right column) fields of the reference model for different times, t, and bulk shortening, γ_b. Strain rate and deviatoric stress are quantified with the square root of the second invariant of the strain rate, $\dot{\epsilon}_{II}$, and deviatoric stress, τ_{II}, tensor, respectively. Magnitudes of $\dot{\epsilon}_{II}$ and τ_{II} are displayed with logarithmic colorscale. Colormaps are from Crameri (2018).

residing above the strong layer, are dragged below the detaching strong layer (Fig. 4.5). During the horizontal transport, the detached unit, consisting of the strong layer and some weak units, is displaced above the cover material. Significant horizontal transport is facilitated because the underlying basement and the strong layer of the left half-graben are significantly more competent than the weak units at the base of the overthrusting nappe.

While the detached unit from the right basin is overthrusting the fill of the left half-graben, this fill is also sheared out of the half-graben due to (i) shear stresses generated by the overthrusting unit and (ii) closure of the half-graben due to ductile deformation of basement units. During overthrusting, some parts of the cover units are incorporated between the overthrusting unit and the fill of the left half-graben. Finally, a nappe consisting of the fill from the right basin has been stacked above a fold nappe made of fill from the left half-graben. The entire process of nappe detachment, transport and stacking occurs during ca 8 Myr for the applied bulk shortening velocity of 1 cm.yr^{-1}. At the end of the simulation, the temperatures of the strong layer range between 250 °C at the topmost

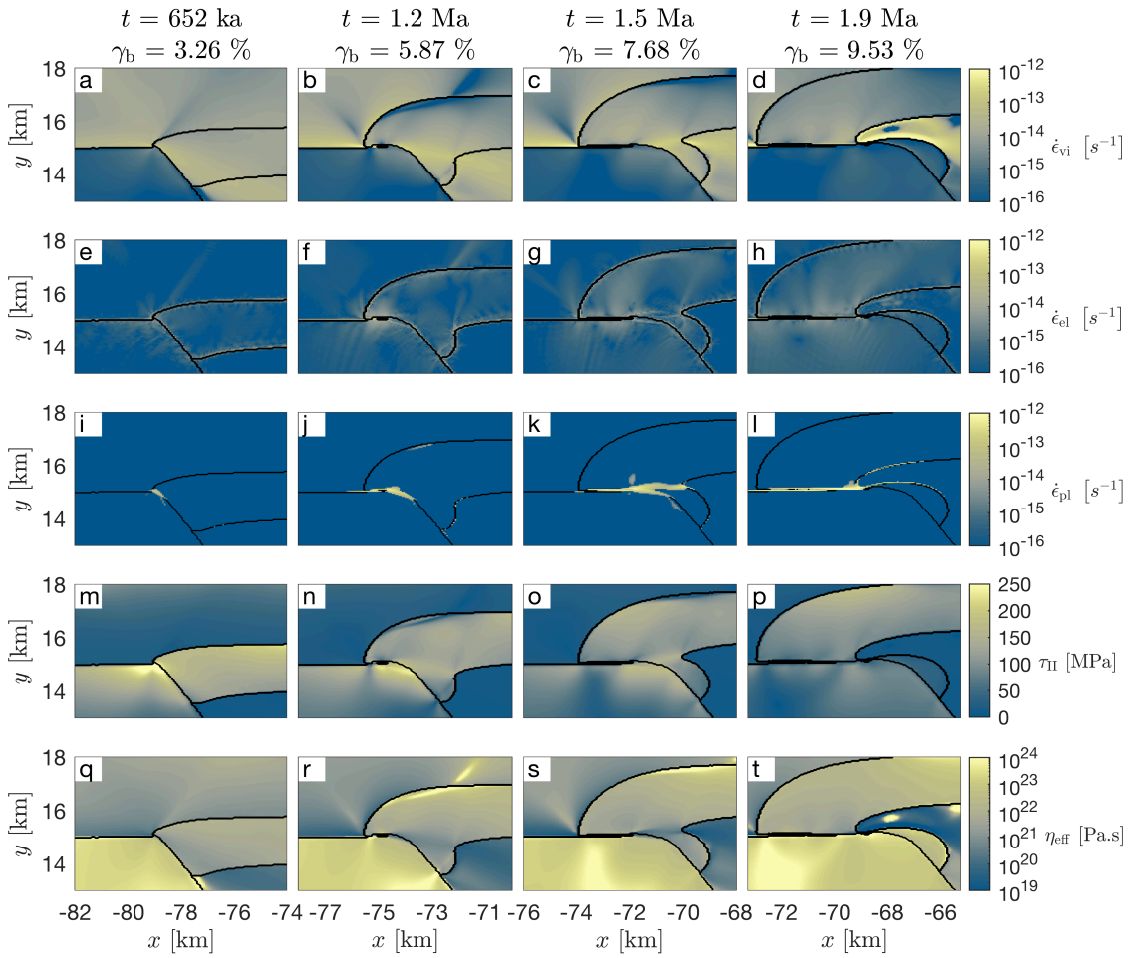

Figure 4.5 – Enlargement of different stages of the detachment of the strong layer from the basement horst for different times, t, and bulk shortening, γ_b (see figure 4.4 for entire model domain). Colorplots of viscous strain rates (a-d), elastic strain rates (e-h), plastic strain rates (i-l), deviatoric stresses (m-p) and effective viscosities (q-t) are displayed. For all strain rate and stress tensor quantities we display their corresponding square root of the second invariants.

position and 350 °C in the root zone of the fold nappe. The final bulk shortening was ca 38 % after ca 8 Myr.

4.4.2 Impact of varying strength contrast

We performed three simulations with the same initial geometry as the reference simulation, but with modified pre-factors, f, in the applied flow laws. All simulations are terminated after a bulk shortening of ca 38 %, corresponding to the one of the reference simulation. In a first simulation, we used a smaller effective viscosity only for the basement ($f = 0.33$). Here, the basement is weak enough to deform significantly from the beginning of shortening. Yield stresses are not reached at the contact of the basement horst with the strong layer (Fig. 4.6a). The strong layer does, hence, not detach from the basement and overthrusting does not take place. Instead, a several km large fold nappe develops in the strong layer of the right basin. Due to the highly distributed basement deformation, the half-graben closes only partially, resulting in a moderate buckling of the strong layer, but not in fold nappe formation. Also, a nappe stack does not form in the simulation.

In a second simulation, we used a stronger cover ($f = 0.5$ instead of $f = 0.1$). The effective viscosities of basement and cover are similar, hence, a mostly evenly distributed thick-skinned deformation is present from the beginning of shortening (Fig. 4.6c and d). A large scale fold develops above the horst, but the overturned limb made of the strong layer eventually detaches from the basement by necking. Although the overthrusting stage results in a significant horizontal displacement, this displacement is only half of the one in the reference simulation and not enough to form a nappe stack. Due to the stronger shear drag from the top, the strong layer of the left half-graben is almost entirely sheared out from the half-graben. The strong layer of the left half-graben forms an overthrust nappe with significant horizontal displacement and with significant internal extension.

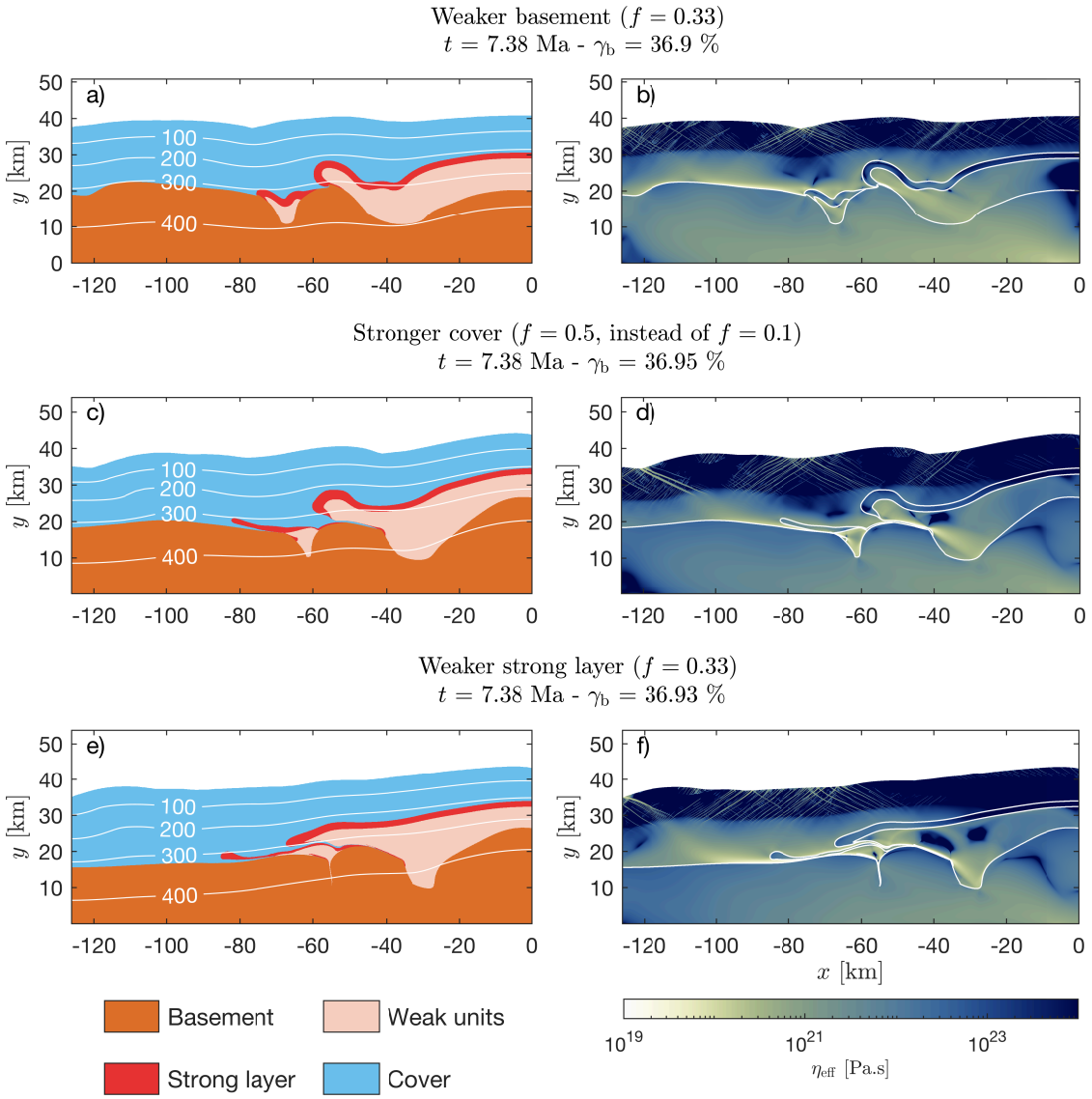

Figure 4.6 – The final geometry, temperature and viscosity fields of three simulations with different f factor for certain model units (see text).

In a third simulation, we used weaker strong layers ($f = 0.33$). The development of the sediment units of the basin is largely similar to that in the reference model (Fig. 4.6). The only notable difference is that before the strong layer is detached from the basement,

it forms a shear fold that is on the scale of a few km. The development of the units of the left half-graben is largely different compared to the reference simulation. Since the strong layer is weaker, the drag from the overriding units is sufficient to detach the strong layer from its left contact with the basement and displace it several tens of km to the left. During this displacement, the strong layer from the left half-graben is highly stretched and almost necking at its tail. Due to significant horizontal displacements, a nappe stack forms with two thrust sheets on the top of each other. However, the strong layer from the left half-graben is displaced considerably further towards the left than the strong layer from the right basin.

The final result of the three simulations, especially with respect to nappe detachment, transport and stacking, differs significantly from the result of the reference simulation, although the effective viscosities of individual model units have been modified by factors of only three to five (Fig. 4.6). The results indicate that the effective viscosity contrast between the model units has a first-order impact on the results.

At the onset of nappe formation, after ca 5% bulk shortening, the reference simulation and the three simulations with different f factors exhibit different distributions and magnitudes of effective viscosity (Fig. 4.7). The maximal viscosity contrast in the reference simulation is up to five orders of magnitude inside the model domain, mainly between weak units in the basin and the uppermost cover (Fig. 4.7a). The effective viscosity at the top of the basement is in the order of 10^{24} Pa.s and the viscosity of the cover directly above the basement is at least one order of magnitude smaller. The strong layers have locally similar maximal effective viscosities than the top basement in the order of 10^{24} Pa.s. The effective viscosity contrast between strong layer and weak units in the right basin is ca three orders of magnitude (Fig. 4.7a). The above mentioned viscosity ratios between model units are required to generate the nappe detachment, transport and stacking in the reference simulation. In the three models with different f factors in some model units, one of these viscosity ratios is different and, hence, the final result differs from the one of the reference simulation (Fig. 4.7).

4.4.3 Impact of multilayers

We also run simulations in which we replaced the single strong layer in the reference model with two thinner ones that are separated by weak units. We run three simulations with different initial thickness distributions of the two strong layers and alternating weak units. The initial thickness configuration is displayed on the right of the three panels in Fig. 4.8. The material parameters of every unit are the same as in the reference model. The basement deformation agrees with the one in the reference model. The deformation of the strong layers is different. Initially, the strong layers of the right basin form more intense, shorter wavelength (due to their smaller thickness) buckle folds, in agreement with the dominant wavelength theory (e.g. Biot, 1961; Schmalholz and Mancktelow, 2016).

In the simulations, where the upper strong layer rests directly below the cover (Fig. 4.8b, c), the top layer is being detached and transported in a similar fashion as in the reference model. The lower layer, on the other hand, forms a fold nappe first, with an

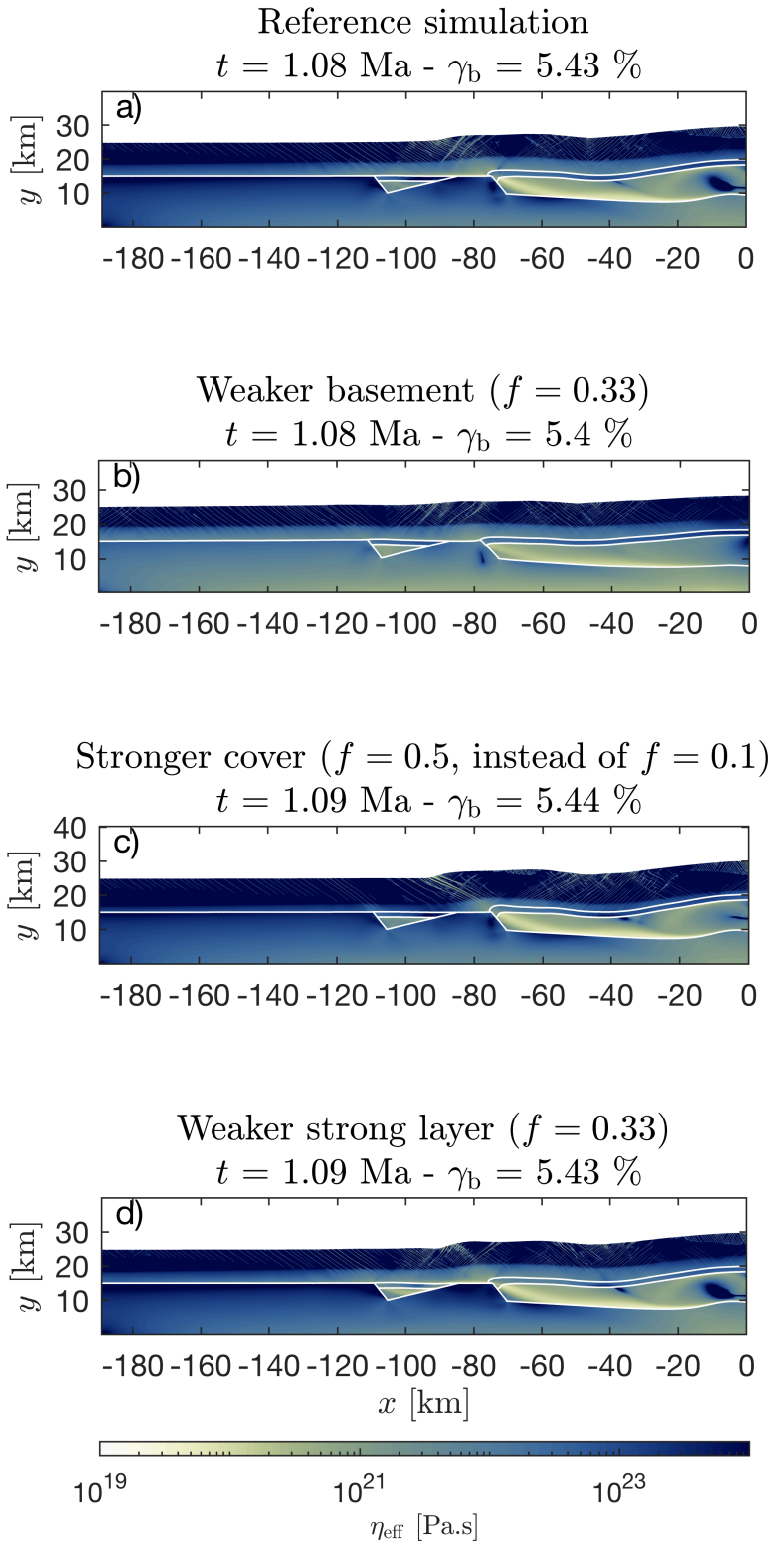

Figure 4.7 – Effective viscosity for four simulations with different f factor for certain model units after a bulk shortening of ca 5.4%. Panel a) displays the reference simulation and panels b) to d) displays the three simulations shown in figure 4.6.

extremely thinned inverse limb. Eventually this inverse limb develops boudinage, and once necking takes place it detaches from the basement. In the simulation, in which a weak unit is located between the upper strong layer and the cover (Fig. 4.8a), both layers form folds

and detach from the basement horst by necking in the inverse limb. After the detachment, the internal deformation of the strong layers is negligible.

The deformation of the units of the left half-graben is similar to the reference model, when weak units are located between the upper strong layer and the cover (Fig. 4.8a). The main difference to the reference simulation is that the weak unit located on top of the half-graben is sheared out, and both strong layers form a fold nappe with a more intensely stretched inverse limb. In the models, in which the upper strong layer is in direct contact with the cover (Fig. 4.8b, c), the deformation of the strong layers in the half-graben is considerably different than it is in the reference model. Because the strong layer on the top of the left half-graben is much thinner, the drag from the overriding unit is sufficient to displace this layer considerably horizontally. The drag from the top shears the upper strong layer of the left half-graben above the basement to the left and it detaches the layer from the half-graben. As a result, buckle and shear folds form around the left tip of the layer (Fig. 4.8b). The upper strong layer starts moving sub-horizontally without considerable internal deformation, and eventually forms a rootless nappe. The lower strong layer of the half-graben stays mostly in place, until the weak units are extruded from the half-graben due to its closure. Then, the lower strong layer forms a fold nappe, with a highly stretched inverse limb (Fig. 4.8b, c).

4.4.4 Impact of softening mechanisms

We also test the impact of two different softening mechanisms that can enhance strain localization (Fig. 4.9). The first mechanism is thermal softening by shear heating due to the conversion of mechanical work into heat and the resulting decrease of the temperature dependent viscosity (e.g. Yuen et al., 1978; Kaus and Podladchikov, 2006; Jaquet and Schmalholz, 2017; Kiss et al., 2019). Although this mechanism is activated in all simulations, for the applied 1 cm.yr^{-1} convergence velocity its impact on structure development is negligible. However, for faster bulk shortening, with 5 cm.yr^{-1} convergence velocity, thermal softening is sufficient to cause spontaneous shear zone formation (Kiss et al., 2019). For the simulation with 5 cm.yr^{-1} convergence velocity, all other parameters are identical to the ones in the reference simulation. There are two striking differences between the two simulations. First, in the high velocity simulation prominent ductile shear zones are formed in the cover that also promote the appearance of more localized brittle deformation zones (Fig. 4.9a). Second, heat production in the ductile shear zone raises the temperature of the units close to the "back-stop" on the right model side. Thus, the basement deformation in the right model domain is more intense, the left half-graben in the basement is not being closed and the sediment fill is not being squeezed out (Fig. 4.9a).

The other considered softening mechanism is plastic strain softening. Such softening is frequently applied in numerical models of crustal deformation in order to enforce highly-localized brittle deformation by decreasing the friction angle as a function of accumulated plastic strain (e.g. Buiter et al., 2006). Such softening algorithm generates mesh-dependent results, but we apply it here for comparison, because such strain softening is applied in

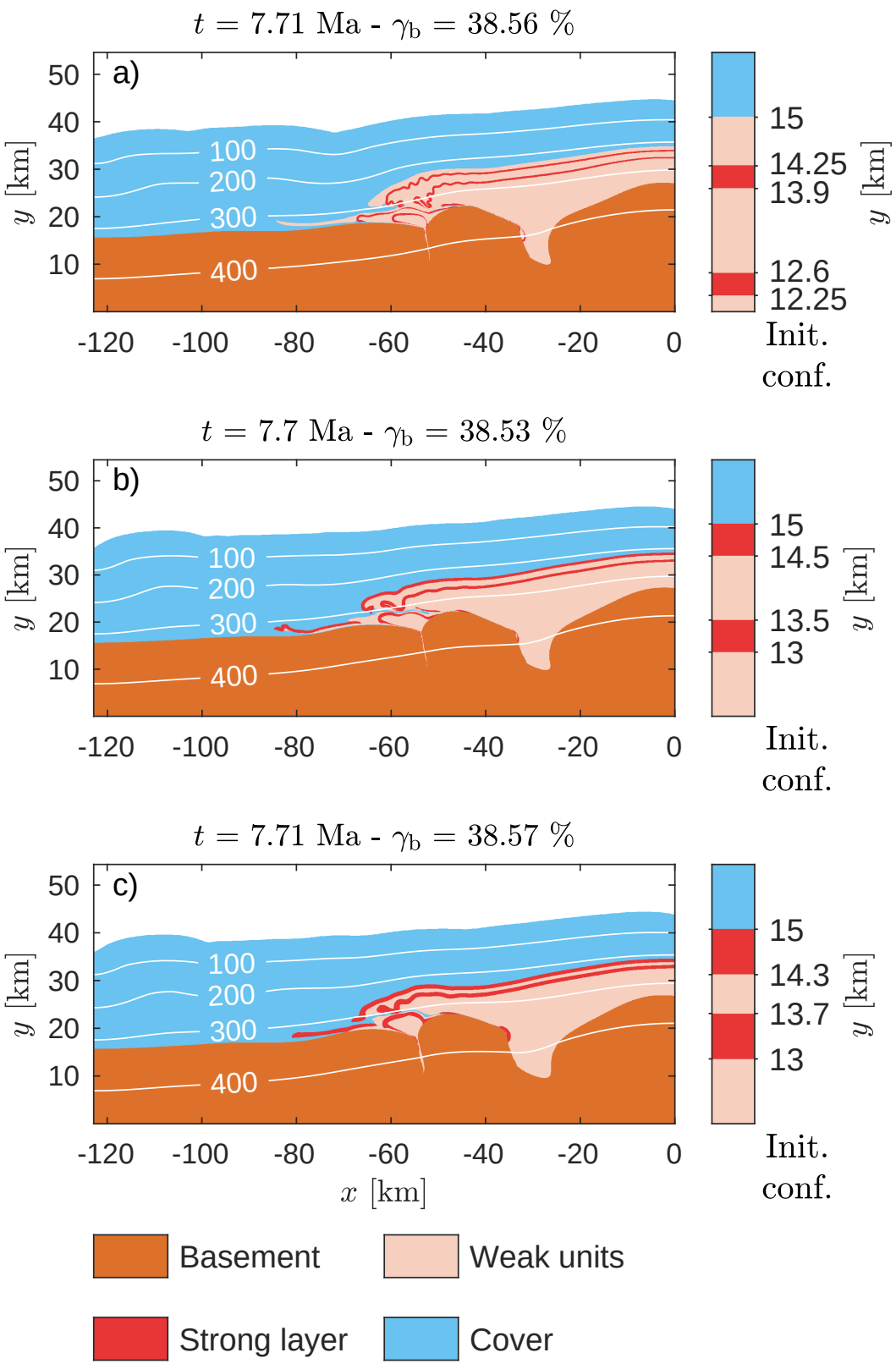

Figure 4.8 – The final geometry of three simulations with two strong layers with the isotherms of the corresponding temperature field. The initial model stratigraphy around the upper region of the half-graben and basin is displayed on the right of each panel. The model stratigraphy is laterally homogenous, so the overall initial configuration is similar to that in Figure (4.2).

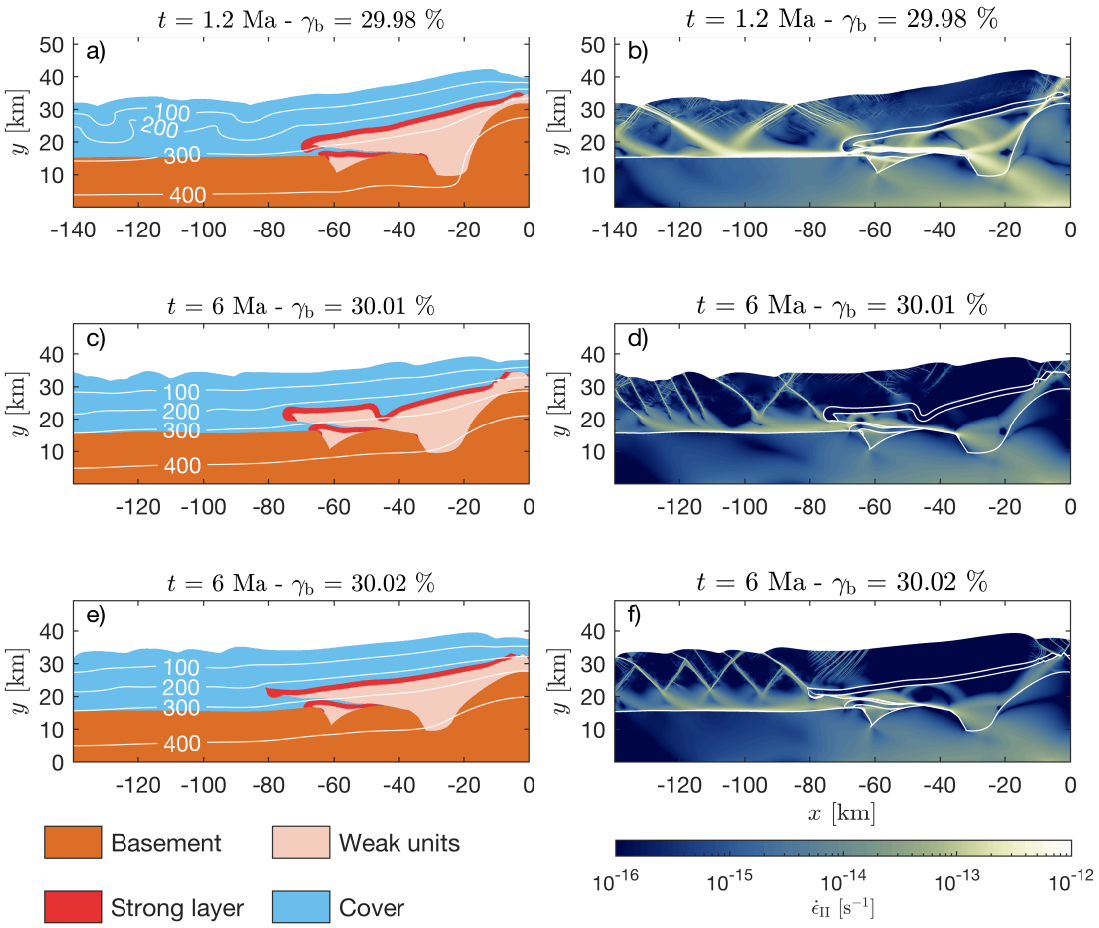

Figure 4.9 – The geometry and the strain-rate field of three simulations after ca 30% bulk shortening, with various softening mechanisms. Panels a) and b) show results of a simulation with a convergence rate of 5 $\mathrm{cm.yr^{-1}}$, in which thermal softening has a significant impact. Panels c) and d) show results of a simulation with strain softening that reduces friction angle from the initial 30 degrees to 5 degrees. Panels e) and f) show results of a simulation with strain softening that reduces friction angle from the initial 15 degrees to 5 degrees.

many numerical models of fold-and-thrust belts (e.g. Buiter et al., 2006; Erdős et al., 2014; Ruh et al., 2014). We used two different parameter sets to model strain softening. In the first case (Fig. 4.9b), we start with a friction angle of 30° that we linearly decrease to 5° between an accumulated plastic strain of 0.5 and 1.5. Compared to the reference simulation, we observe strongly localized brittle deformation that is characterized by high angle ($\gg 0°$ from horizontal) and small displacement (< 10 km) overthrusts. This is the only simulation, where a strong back-thrust forms over the right basin that also deforms the strong layer. In the second case (Fig. 4.9c), we start with a friction angle of 15° that we linearly decrease to 5° between accumulated plastic strain of 0.5 and 1.5. Such initially lower friction angle is often suggested to mimic fluid-pressure reduced effective friction angles (e.g. Erdős et al., 2014). In this simulation, the detachment mechanism of the right, strong layer from the horst is different, as the initial buckling and folding phase is entirely missing, and plastic yielding dominates from the beginning of deformation. Initially, the angle of thrusting is ca 35° from the horizontal. Once a sufficient amount of weak units are

sheared on top of the horst, the transport direction is sub-horizontal. Similarly to the other simulations with significant softening mechanisms, the basement around the half-graben is only deformed to a small degree and the half-graben is not closed.

4.5 Discussion

4.5.1 Numerical robustness

We investigated the impact of different numerical resolutions on the model results to test the robustness of these results. Such resolution test is important for the presented simulations, because weak material, such as cover and weak units, is entrapped along thin regions between stronger model units, such as strong layer and basement. Entrapment of weak material between strong material can cause mechanical decoupling if resolved numerically. We compare the reference model with an original resolution of 3001×1001 (width×height) numerical grid points (initially 66×25 m grid spacing) with two simulations having identical configuration and parameters, but with smaller resolutions of 1501×501 (initially 133×50 m) and 751×251 (initially 267×100 m). The resulting structures after 38% of bulk shortening are essentially identical (Fig. 4.10). Similarly, the strain rate fields below the brittle-ductile transition are similar too. However, the strain rate distribution in the brittle part and around the brittle-ductile transition is resolution dependent (Fig. 4.10). This is typical for the applied non-associated plasticity scheme with the Drucker-Prager yield criterion, that is merely a stress limiter, inhibiting the stresses to exceed the failure limit. Thus the exact geometry of the brittle-plastic shear bands is resolution dependent, but the effective load bearing capacity of the brittle layer converges with increasing resolution (Yamato et al., 2019, their appendix). Keeping in mind these limitations regarding the brittle-plastic deformation, the results in our main area of interest, that is the ductile nappe stacking, are essentially independent on the resolution within the studied range. Hence, our results are numerically robust concerning the detachment, transport and stacking of nappes under dominantly ductile deformation.

4.5.2 Comparison of the model results with the geological observations

There are several features of the Helvetic Nappe System that we could successfully reproduce in our thermo-mechanical model. Similarly to Bauville and Schmalholz (2015), a structure resembling a fold nappe has been formed by the extrusion of the sedimentary fill from a half-graben. During formation of this fold nappe, the half-graben has been closed and the sediments squeezed between the two basements resemble the structure of the Chamonix zone located between the Aiguilles-Rouges and Mont-Blanc massifs (Fig. 4.1c). Hence, our model generated the first-order structural features of the Infrahelvetic complex in W-Switzerland, namely a recumbent fold nappe with a root located between two deformed basement massifs. Additionally, our model reproduced the detachment and sub-horizontal transport of sedimentray units from a model passive margin structure. The thrust nappe, which originates from the rigth basin in our model, resembles the Wildhorn super-nappe. The horizontal transport of this thrust nappe is in the order of 30 km in the

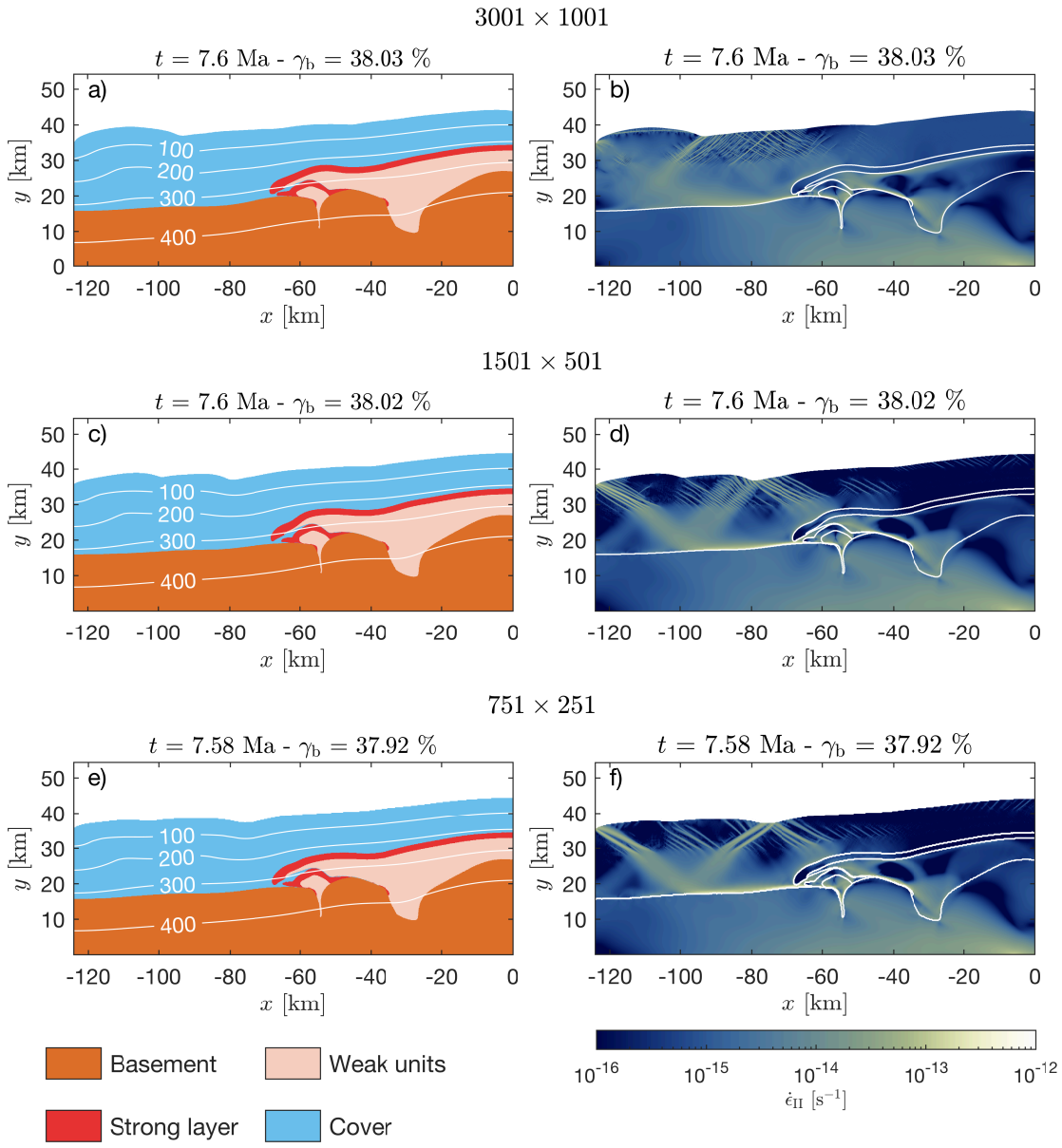

Figure 4.10 – The geometry and the strain-rate field of three simulations after ca 38% bulk shortening for different numerical resolutions.

model. Furthermore, in the model this thrust sheet is stacked above the fold nappe and the final model structure resembles a thrust nappe that is stacked above a fold nappe, as observed in the Helvetic nappe system. Moreover, there is a considerable amount of cover units entrapped between the fold nappe and the thrust sheet. The entrapped lower region of the cover unit resembles the Ultrahelvetic units so that our model can explain how these Ultrahelvetic units have been entrapped between the Morcles fold nappe and the Wildhorn super-nappe (Fig. 4.1c). At the end of the simulated formation of the nappe system, the maximum temperature in the nappe system ranges between 250 °C and 350 °C, which is in agreement with the metamorphic peak temperatures of the Helvetic nappe system reported by Kirschner et al. (1996) and Ebert et al. (2007). In the simulations, the nappe stack is formed within ca 8 Myr, which is also in broad agreement with the estimated time

span of main formation of the Morcles fold nappe from ca 28 to 17 Ma (Kirschner et al., 1995). The simulations with two thin strong layers, separated by weak units, can explain the significant parasitic, or second order, folding of the two main carbonate units (Quinten and Urgonian limestone formations) which is observed in the Wildhorn super-nappe.

Some features of the Helvetic Nappe System are not reproduced by the simulations. In the frontal part of the fold nappe, originating from the left half-graben, the front is first thrust out of the half-graben and the overturned limb develops subsequently. This deformation generates a "nose-like" structure in the frontal part of the fold nappe, which is not observed. Also, in all simulations the fold nappe has only a minor second order folding, in contrast with the prominent parasitic folds of the Morcles nappe. Reproducing these natural, second-order parasitic folds with their correct scale with respect to the first-order fold nappe would require an even higher numerical resolution. In the numerical models, we also likely overestimated the amount of shale-rich sediments in the right basin, mimicking the Helvetic basin, as the total volume of the Wildhorn super-nappe south of the Morcles nappes is much thinner than in the simulations. There was also likely a significant amount of vertical flattening, and presumably pressure solution related volume decrease, after the main phase of nappe formation and during the exhumation of the nappe system, which is not modelled in our simulations. Moreover, several basement shear zones have been mapped in the Aiguilles-Rouges and in the Mont-Blanc massifs, which are not present in the simulations. This is likely because (i) the straight bottom boundary of the model may prohibit any significant vertical displacement of the basement units and hence inhibit significant shear zone formation, (ii) the model basement is mechanically homogeneous and there are no heterogeneities that can trigger shear zone localization and (iii) the amount of brittle-plastic deformation is underestimated in the basement. We considered a horizontal model base while during natural nappe formation the overall basement-cover interface was likely dipping, or tilting, in the direction of subduction (i.e. direction of basal velocity), so that a model bottom inclinded towards the subduction direction would be more realistic. The deformation at our model bottom is viscous and the surface slope for evolving crustal wedges with a viscous base depends on the viscous shear stress at the base, whereby larger shear stresses are related to higher surface slopes (e.g. Ruh et al., 2012). Keeping the basal viscous shear stress the same, a tilting of the model base towards the subduction direction would reduce the surface slope. Therefore, in our models the surface slopes towards the foreland (left) region represent high end-member surface slopes so that effects of gravity-related forces directed towards the foreland region are on the higher end.

Finally, the applied "numerical sandbox" model configuration and velocity boundary conditions constrain the deformation in the model domain. During the large-scale dynamics of Alpine orogenic wedge formation, the straight bottom and right model boundaries do not exist. Processes such as laterally-varying vertical isostatic adjustment, flexure due to subduction and back-thrusting, or back-folding, generate geodynamic conditions for the formation of the Helvetic nappe system which are clearly more dynamic and complex than implied by the considered model configuration. Lithospheric scale numerical models can self-consistently model the generation of orogenic wedges and major crustal shear zones,

including effects of isostasy, flexure and back-folding (e.g. Erdős et al., 2014; Jaquet et al., 2018; Jourdon et al., 2019; Erdős et al., 2019). With higher numerical resolution such lithosphere models may eventually be able to resolve the upper crustal deformation with a resolution as applied in our model.

4.5.3 Tectonic inheritance, mechanical heterogeneities and potential softening mechanisms

Geological reconstructions of the Helvetic nappe system showed the correlation of the nappes with their original positions along the pre-Alpine European passive margin, which was characterized by half-grabens and horsts (e.g. Epard, 1990; Boutoux et al., 2014). In agreement with previous modelling studies (e.g. Beaumont et al., 2000; Wissing and Pfiffner, 2003; Bellahsen et al., 2012; Lafosse et al., 2016; Bauville and Schmalholz, 2017), our results suggest that tectonic inheritance in the crust in the form of half-grabens and horsts has a strong impact on the development of fold and thrust nappes during crustal deformation. Our results indicate that two features of the tectonic inheritance are important, namely the geometry and the magnitude of mechanical heterogeneities. The geometry of half-grabens and horsts controls the location of nappe initiation (Bauville and Schmalholz, 2017). The basement and sediments must, of course, have different mechanical strength, otherwise the geometry of the basement would be unimportant. Our results suggest that tectonic inheritance is necessary to model the evolution of the Helvetic nappe system, but not sufficient. The results show that specific strength, or effective viscosity, contrast between basement and sediments and within the sediments are required to model nappe structures resembling those of the Helvetic nappe system (Figs. 4.6 and 4.7). The reference simulation exhibits a viscosity contrast between weak units and strong layer and basement in the order of four orders of magnitude (Fig. 4.7a). Although the effective viscosity in the basement and strong layer is in the order of 10^{24} Pa.s, the stresses in the basement and strong layer are far below the brittle-plastic yield stress and typically smaller than 100 MPa (Fig. 4.4). If the effective viscosity contrast between strong layer and basement is not large enough, then the sediments of the right basin are not detached in the manner of a thrust sheet from their original position (Fig. 4.6a). One possibility to enforce detachment also for smaller viscosity contrasts is the application of plastic strain softening and/or initially reduced friction angles (Fig. 4.9b and c). Application of strain softening favors the formation of thrust sheets in the models, but prohibits the formation of fold nappes (Fig. 4.9b and c). The importance of tectonic inheritance and the pre-Alpine configuration on the nappe formation during Alpine orogeny underlines the importance of geological field work and associated geological reconstructions, because only such field based reconstructions can provide estimates for the pre-Alpine configurations. Our results are consistent with those of Duretz et al. (2011) which showed that inherited mechanical heterogeneities, promoting large lateral strength contrast, are essential to trigger exhumation of lower crustal granulites as observed in the Bohemian Massif. Generally, our results are consistent with a variety of studies, which show the importance of structural inversion of extensional systems during compressional deformation and are based on geological field

observation, analogue deformation experiments and numerical models (e.g. Gillcrist et al., 1987; Buiter and Adrian Pfiffner, 2003; Buiter et al., 2009; Bellahsen et al., 2012; Bonini et al., 2012; Lafosse et al., 2016; Granado and Ruh, 2019).

For the applied model configuration, a significant localization due to thermal softening does not occur for a convergence velocity of 1 cm.yr^{-1}, but it does for 5 cm.yr^{-1}. Average convergence velocities during the Alpine orogeny are typically estimated to be in the order of 1 cm.yr^{-1} (Schmid et al., 1996). However, some short periods with higher convergence velocities cannot be excluded. So if there were short periods during the formation of the Helvetic nappe system with convergence velocities larger than ca 5 cm.yr^{-1}, then thermal softening might have been important.

There is field evidence for grain size reduction associated with mylonitic shear zones at the base of nappes in the Helvetic nappe system (e.g. Ebert et al., 2007, 2008). We did not consider the microscale grain size reduction in our models for several reasons: First, the major mylonitic shear zones with significant grain size reduction have a thickness in the order of 10 m. Although we use high resolution models we have a numerical grid size of ca 66×25 m, hence, this resolution is still not large enough to resolve the internal deformation within shear zones having thickness of 10 m. Second, recent numerical simulations including grain size reduction and combined diffusion and dislocation creep flow laws suggest that grain size reduction does not have a dramatic impact on strain localization (Schmalholz and Duretz, 2017), which is in agreement with theoretical results of Montési and Zuber (2002). The reason is that a piezometer-type stress to grain size relation, when subsituted into a grain-size-sensitive diffusion creep flow law, generates a power-law type flow law with stress exponents similar to the one of the corresponding dislocation creep flow law (e.g. Montési and Zuber, 2002). However, other studies argue that microscale processes such as coupled grain evolution and damage mechanisms can generate significant strain localization and that these mechanisms have been responsible for generating subduction and plate tectonics (e.g. Bercovici and Ricard, 2014). Therefore, future simulations should consider such coupled microscale processes in order to quantify their importance on the first order tectonic nappe detachment, overthrusting and stacking.

4.6 Conclusions

The presented 2D thermo-mechanical simulations of shortening of the upper crustal region of a passive margin consider initial mechanical heterogeneities and can explain key aspects of tectonic nappe formation. Two types of heterogeneities are considered: (1) a lateral heterogeneity due to the basement-cover interface that is characterized by half-grabens and horsts, and (2) a vertical heterogeneity due to alternating sedimentary layers with different mechanical strength. The simulations can model the detachment and sub-horizontal transport of a nappe and the stacking of two nappes. Detachment of sedimentary units occurs due to stress concentrations in strong sediment layers around the basement-sediment contact, which result in a localized brittle-plastic shear band that detaches the strong layer from the basement. Horizontal transport is controlled by basement-cover geometry and occurs by moving relatively stronger sediment units above thinner and weaker units. The

detached and horizontally transported units resemble a thrust nappe. Structures resembling fold nappes form by the ductile closure of a half-graben and the associated extrusion of the sedimentary half-graben fill; in agreement with previous modelling studies. In the simulations, the thrust nappe initiates before the fold nappe, because it is located closer to the "back-stop" of the applied model configuration. The thrust nappe exhibits a larger horizontal displacement than the fold nappe so that the thrust nappe can be stacked above the fold nappe.

The considered lateral variation of the basement-cover interface and associated mechanical heterogeneity is necessary to model nappe formation and stacking, but it is not sufficient. Additionally, a specific effective viscosity contrast between basement and strong and weak sediments is required. For our model configuration, an effective viscosity contrast of approximately four orders of magnitude between weak sediments and strong sediments and basement is required. Simulations with smaller viscosity contrasts did not generate the detachment and transport of thrust nappes. Nappe detachment and transport are modeled with standard creep flow laws and a Drucker-Prager yield criterion, without the application of strain softening algorithms. Considering several strong layers in the models can explain the second-order internal folding observed within some thrust nappes.

Based on the first-order agreement between our model results and natural data, we propose a macroscale "nappe theory" for the Helvetic nappe system of Western Switzerland. Our "nappe theory" can be self-consistently calculated and reproduced with a well-established continuum mechanics thermo-mechanical theory and with standard creep flow laws and a Drucker-Prager yield criterion, which are based on rock deformation experiments. We propose that the pre-Alpine configuration of the European passive margin was characterized by important mechanical heterogeneities resulting from (i) a basement-cover contact with half-grabens and horst, and (ii) the alternation of mechanically strong and weak sediment units. During the Alpine continental collision, the passive margin is shortened and sheared due to external compressive stresses. During margin deformation, mechanical heterogeneities control the detachment, transport and stacking of nappes. The sedimentary units of the Wildhorn super-nappe are detached due to the existence of horsts, or basement highs, causing stress concentrations and brittle-plastic shear bands. The Wildhorn super-nappe was transported mainly above weak shale-rich units and weak Ultrahelvetic units, which have been entrapped from above to below the Wildhorn super-nappe. Formation of the Morcles fold nappe occured by dominantly ductile closing of a half-graben, bounded by basement massifs that form now the Aiguilles-Rouges and Mont-Blanc massifs, and the associated squeezing-out of sediments from this half-graben.

Acknowledgements

This work was supported by SNF grant No. 200020-149380 and the University of Lausanne.

References

Aharonov, E. and C. H. Scholz
2018. A physics-based rock friction constitutive law: Steady state friction. *Journal of Geophysical Research: Solid Earth*, 123(2):1591–1614.

Argand, E.
1916. *Sur l'arc des Alpes occidentales.* G. Bridel.

Avouac, J.-P., L. Meng, S. Wei, T. Wang, and J.-P. Ampuero
2015. Lower edge of locked main himalayan thrust unzipped by the 2015 gorkha earthquake. *Nature Geoscience*, 8(9):708.

Bailey, E. B.
1935. *Tectonic essays: mainly Alpine.* Clarendon P.

Bauville, A., J.-L. Epard, and S. M. Schmalholz
2013. A simple thermo-mechanical shear model applied to the morcles fold nappe (western alps). *Tectonophysics*, 583:76–87.

Bauville, A. and S. M. Schmalholz
2015. Transition from thin-to thick-skinned tectonics and consequences for nappe formation: Numerical simulations and applications to the helvetic nappe system, switzerland. *Tectonophysics*, 665:101–117.

Bauville, A. and S. M. Schmalholz
2017. Tectonic inheritance and kinematic strain localization as trigger for the formation of the helvetic nappes, switzerland. *Swiss Journal of Geosciences*, 110(2):523–534.

Beaumont, C., J. A. Muñoz, J. Hamilton, and P. Fullsack
2000. Factors controlling the alpine evolution of the central pyrenees inferred from a comparison of observations and geodynamical models. *Journal of Geophysical Research: Solid Earth*, 105(B4):8121–8145.

Bellahsen, N., L. Jolivet, O. Lacombe, M. Bellanger, A. Boutoux, S. Garcia, F. Mouthereau, L. Le Pourhiet, and C. Gumiaux
2012. Mechanisms of margin inversion in the external western alps: Implications for crustal rheology. *Tectonophysics*, 560:62–83.

Bercovici, D. and Y. Ricard
2014. Plate tectonics, damage and inheritance. *Nature*, 508(7497):513.

Bertrand, M.
1884. Rapports de structure des alpes de glaris et du bassin houiller du nord. *Bull. Soc. geol. France.*, 3:318–330.

Biot, M. A.
1961. Theory of folding of stratified viscoelastic media and its implications in tectonics and orogenesis. *Geological Society of America Bulletin*, 72(11):1595–1620.

Bonini, M., F. Sani, and B. Antonielli
2012. Basin inversion and contractional reactivation of inherited normal faults: A review based on previous and new experimental models. *Tectonophysics*, 522:55–88.

Boutonnet, E., P. H. Leloup, C. Sassier, V. Gardien, and Y. Ricard
2013. Ductile strain rate measurements document long-term strain localization in the continental crust. *Geology*, 41(8):819–822.

Boutoux, A., N. Bellahsen, O. Lacombe, A. Verlaguet, and F. Mouthereau
2014. Inversion of pre-orogenic extensional basins in the external western alps: structure, microstructures and restoration. *Journal of Structural Geology*, 60:13–29.

Boyer, S. E. and D. Elliott
1982. Thrust systems. *Aapg Bulletin*, 66(9):1196–1230.

Bucher, W. H.
1956. Role of gravity in orogenesis. *Geological Society of America Bulletin*, 67(10):1295–1318.

Buiter, S. J. and O. Adrian Pfiffner
2003. Numerical models of the inversion of half-graben basins. *Tectonics*, 22(5).

Buiter, S. J., A. Y. Babeyko, S. Ellis, T. V. Gerya, B. J. Kaus, A. Kellner, G. Schreurs, and Y. Yamada
2006. The numerical sandbox: comparison of model results for a shortening and an extension experiment. *Geological Society, London, Special Publications*, 253(1):29–64.

Buiter, S. J., O. A. Pfiffner, and C. Beaumont
2009. Inversion of extensional sedimentary basins: A numerical evaluation of the localisation of shortening. *Earth and Planetary Science Letters*, 288(3-4):492–504.

Casey, M. and D. Dietrich
1997. Overthrust shear in mountain building. In *Evolution of Geological Structures in Micro-to Macro-scales*, Pp. 119–142. Springer.

Crameri, F.
2018. Scientific colour-maps.

Dal Piaz, G. V.
2001. History of tectonic interpretations of the alps. *Journal of geodynamics*, 32(1-2):99–114.

Di Toro, G., R. Han, T. Hirose, N. De Paola, S. Nielsen, K. Mizoguchi, F. Ferri, M. Cocco, and T. Shimamoto
2011. Fault lubrication during earthquakes. *Nature*, 471(7339):494.

Dietrich, D. and M. Casey
1989. A new tectonic model for the helvetic nappes. *Geological Society, London, Special Publications*, 45(1):47–63.

Duretz, T., B. Kaus, K. Schulmann, D. Gapais, and J.-J. Kermarrec
2011. Indentation as an extrusion mechanism of lower crustal rocks: Insight from analogue and numerical modelling, application to the eastern bohemian massif. *Lithos*, 124(1):158 – 168. Granulite facies metamorphism and the rheology of the lower crust.

Duretz, T., D. May, and P. Yamato
2016. A free surface capturing discretization for the staggered grid finite difference scheme. *Geophysical Journal International*, 204(3):1518–1530.

Durney, D.
1982. Some observations concerning the question of gravity gliding and hinterland compression in the western helvetic nappes. In *Int. Conf. on Planar and Linear Fabrics of Deformed Rocks, Zurich, Abstr*, P. 92.

Ebert, A., M. Herwegh, A. Berger, and A. Pfiffner
2008. Grain coarsening maps for polymineralic carbonate mylonites: a calibration based on data from different helvetic nappes (switzerland). *Tectonophysics*, 457(3-4):128–142.

Ebert, A., M. Herwegh, B. Evans, A. Pfiffner, N. Austin, and T. Vennemann
2007. Microfabrics in carbonate mylonites along a large-scale shear zone (helvetic alps). *Tectonophysics*, 444(1-4):1–26.

Epard, J. L.
1990. *La nappe de Morcles au sud-ouest du Mont-Blanc.* PhD thesis, Université de Lausanne.

Epard, J.-L. and A. Escher
1996. Transition from basement to cover: a geometric model. *Journal of Structural Geology*, 18(5):533–548.

Erdős, Z., R. S. Huismans, and P. v. d. Beek
2019. Control of increased sedimentation on orogenic fold-and-thrust belt structure–insights into the evolution of the western alps. *Solid Earth*, 10(2):391–404.

Erdős, Z., R. S. Huismans, P. van der Beek, and C. Thieulot
2014. Extensional inheritance and surface processes as controlling factors of mountain belt structure. *Journal of Geophysical Research: Solid Earth*, 119(12):9042–9061.

Escher, A., H. Masson, and A. Steck
1993. Nappe geometry in the western swiss alps. *Journal of structural Geology*, 15(3-5):501–509.

Escher von der Linth, A.
1841. Geologische carte des cantons glarus und seiner umgebung, nebst profilen. *Verhandlungen der Naturforschenden Gesellschaft in Zürich*, Pp. 52–62.

Fagereng, Å. and J. Biggs
2018. New perspectives on 'geological strain rates' calculated from both naturally deformed and actively deforming rocks. *Journal of Structural Geology*.

Gerya, T. V. and D. A. Yuen
2003. Characteristics-based marker-in-cell method with conservative finite-differences schemes for modeling geological flows with strongly variable transport properties. *Physics of the Earth and Planetary Interiors*, 140(4):293–318.

Gillcrist, R., M. Coward, and J.-L. Mugnier
1987. Structural inversion and its controls: examples from the alpine foreland and the french alps. *Geodinamica acta*, 1(1):5–34.

Goguel, J.
1948. *Introduction à l'étude mécanique des déformations de l'écorce terrestre: par Jean Goguel,... 2e édition*. Impr. nationale.

Granado, P. and J. B. Ruh
2019. Numerical modelling of inversion tectonics in fold-and-thrust belts. *Tectonophysics*, 763:14–29.

Hansen, F., N. Carter, et al.
1983. Semibrittle creep of dry and wet westerly granite at 1000 mpa. In *The 24th US Symposium on Rock Mechanics (USRMS)*. American Rock Mechanics Association.

Heim, A.
1906. Die vermeintliche «gewölbeumbiegung des nordflügels der glarner doppelfalte» südlich vom klausenpass, eine selbstkorrektur. *Vjsch. natf Ges. Zurich.*, 51:403–431.

Herwegh, M., J. Linckens, A. Ebert, A. Berger, and S. Brodhag
2011. The role of second phases for controlling microstructural evolution in polymineralic rocks: A review. *Journal of Structural Geology*, 33(12):1728–1750.

Herwegh, M. and O.-A. Pfiffner
2005. Tectono-metamorphic evolution of a nappe stack: A case study of the swiss alps. *Tectonophysics*, 404(1-2):55–76.

Jaquet, Y., A. Bauville, and S. M. Schmalholz
2014. Viscous overthrusting versus folding: 2-d quantitative modeling and its application to the helvetic and jura fold and thrust belts. *Journal of Structural Geology*, 62:25–37.

Jaquet, Y., T. Duretz, D. Grujic, H. Masson, and S. M. Schmalholz
2018. Formation of orogenic wedges and crustal shear zones by thermal softening, associated topographic evolution and application to natural orogens. *Tectonophysics*, 746:512–529.

Jaquet, Y. and S. M. Schmalholz
2017. Spontaneous ductile crustal shear zone formation by thermal softening and related stress, temperature and strain rate evolution. *Tectonophysics*.

Jourdon, A., L. Le Pourhiet, F. Mouthereau, and E. Masini
2019. Role of rift maturity on the architecture and shortening distribution in mountain belts. *Earth and Planetary Science Letters*, 512:89–99.

Kaus, B. J. and Y. Y. Podladchikov
2006. Initiation of localized shear zones in viscoelastoplastic rocks. *Journal of Geophysical Research: Solid Earth*, 111(B4).

King Hubbert, M. and W. W. Rubey
1959. Role of Fluid Pressure in Mechanics of Overthrust Faulting. *Geological Society of America Bulletin*, 70:115.

Kirschner, D. L., M. A. Cosca, H. Masson, and J. C. Hunziker
1996. Staircase 40/ar39ar spectra of fine-grained white mica: Timing and duration of deformation and empirical constraints on argon diffusion. *Geology*, 24(8):747–750.

Kirschner, D. L., Z. D. Sharp, and H. Masson
1995. Oxygen isotope thermometry of quartz-calcite veins: Unraveling the thermal-tectonic history of the subgreenschist facies morcles nappe (swiss alps). *Geological society of America bulletin*, 107(10):1145–1156.

Kiss, D., Y. Podladchikov, T. Duretz, and S. M. Schmalholz
2019. Spontaneous generation of ductile shear zones by thermal softening: Localization criterion, 1d to 3d modelling and application to the lithosphere. *Earth and Planetary Science Letters*, 519:284–296.

Kronenberg, A. K., S. H. Kirby, and J. Pinkston
1990. Basal slip and mechanical anisotropy of biotite. *Journal of Geophysical Research: Solid Earth*, 95(B12):19257–19278.

Lafosse, M., A. Boutoux, N. Bellahsen, and L. Le Pourhiet
2016. Role of tectonic burial and temperature on the inversion of inherited extensional basins during collision. *Geological Magazine*, 153(5-6):811–826.

Lugeon, M.
1902. Les grandes nappes de recouvrement des alpes du chablais et de la suisse. *Bull. Soc. geol. France.*, 4:723.

Mase, G. E. and G. Mase
1970. *Continuum mechanics*, volume 970. McGraw-Hill New York.

Masson, H.
1976. Un siècle de géologie des préalpes: de la découverte des nappes à la recherche de leur dynamique. *Eclogae geologicae Helvetiae*, 69:527–575.

Masson, H., S. helvétique des sciences naturelles. Commission géologique, R. Herb, A. Steck, and S. N. Ayrton
1980. *Helvetic Alps of Western Switzerland*. Wepf and Company.

Merle, O.
1989. Strain models within spreading nappes. *Tectonophysics*, 165(1-4):57–71.

Merle, O.
1998. *Emplacement mechanisms of nappes and thrust sheets*, volume 9. Springer Science & Business Media.

Merle, O. and B. Guillier
1989. The building of the central swiss alps: an experimental approach. *Tectonophysics*, 165(1-4):41–56.

Montési, L. G. and M. T. Zuber
2002. A unified description of localization for application to large-scale tectonics. *Journal of Geophysical Research: Solid Earth*, 107(B3).

Murchison, R. I.
1849. On the geological structure of the alps, apennines and carpathians, more especially to prove a transition from secondary to tertiary rocks, and the development of eocene deposits in southern europe. *Quarterly Journal of the Geological Society*, 5(1-2):157–312.

Pfiffner, O. A.
1993. The structure of the helvetic nappes and its relation to the mechanical stratigraphy. *Journal of structural Geology*, 15(3-5):511–521.

Pfiffner, O. A.
2014. *Geology of the Alps*. John Wiley & Sons.

Pfiffner, O.-A., M. Burkhard, R. Hänni, A. Kammer, R. Kligfield, N. Mancktelow, J. Menkveld, J. Ramsay, S. Schmid, and R. Zurbriggen
2011. Structural map of the helvetic zone of the swiss alps, including vorarlberg (austria) and haute savoie (france).

Pfiffner, O.-A. and J. Ramsay
1982. Constraints on geological strain rates: arguments from finite strain states of naturally deformed rocks. *Journal of Geophysical Research: Solid Earth*, 87(B1):311–321.

Poirier, J.
1980. Shear localization and shear instability in materials in the ductile field. *Journal of Structural Geology*, 2(1-2):135–142.

Poulet, T., M. Veveakis, M. Herwegh, T. Buckingham, and K. Regenauer-Lieb
2014. Modeling episodic fluid-release events in the ductile carbonates of the glarus thrust. *Geophysical Research Letters*, 41(20):7121–7128.

Price, N. J. and J. W. Cosgrove
1990. *Analysis of geological structures*. Cambridge University Press.

Price, N. J. and K. R. McClay
1981. Thrust and nappe tectonics. Geological Society of London.

Ramsay, J. G., M. Casey, and R. Kligfield
1983. Role of shear in development of the helvetic fold-thrust belt of switzerland. *Geology*, 11(8):439–442.

Rubey, W. W. and M. King Hubbert
1959. Role of fluid pressure in mechanics of overthrust faulting: Ii. overthrust belt in geosynclinal area of western wyoming in light of fluid-pressure hypothesis. *Geological Society of America Bulletin*, 70(2):167–206.

Ruh, J. B., T. Gerya, and J.-P. Burg
2014. 3d effects of strain vs. velocity weakening on deformation patterns in accretionary wedges. *Tectonophysics*, 615:122–141.

Ruh, J. B., B. J. Kaus, and J.-P. Burg
2012. Numerical investigation of deformation mechanics in fold-and-thrust belts: Influence of rheology of single and multiple décollements. *Tectonics*, 31(3).

Schaer, J.-P.
2010. Swiss and alpine geologists between two tectonic revolutions. part 1: from the discovery of nappes to the hypothesis of continental drift. *Swiss Journal of Geosciences*, 103(3):503–522.

Schardt, H.
1893. *Sur l'origine des Préalpes romandes Zone du Chablais et du Stockhorn*. Verlag nicht ermittelbar.

Schmalholz, S. M. and T. Duretz
2017. Impact of grain size evolution on necking in calcite layers deforming by combined diffusion and dislocation creep. *Journal of Structural Geology*, 103:37–56.

Schmalholz, S. M., T. Duretz, G. Hetényi, and S. Medvedev
2019. Distribution and magnitude of stress due to lateral variation of gravitational potential energy between indian lowland and tibetan plateau. *Geophysical Journal International*, 216(2):1313–1333.

Schmalholz, S. M. and N. S. Mancktelow
2016. Folding and necking across the scales: a review of theoretical and experimental results and their applications. *Solid Earth*, 7(5).

Schmid, S., J. Boland, and M. Paterson
1977. Superplastic flow in finegrained limestone. *Tectonophysics*, 43(3-4):257–291.

Schmid, S. M., O.-A. Pfiffner, N. Froitzheim, G. Schönborn, and E. Kissling
1996. Geophysical-geological transect and tectonic evolution of the swiss-italian alps. *Tectonics*, 15(5):1036–1064.

Scholz, C. H.
1998. Earthquakes and friction laws. *Nature*, 391(6662):37.

Smoluchowski, M.
1909. Ii.—some remarks on the mechanics of overthrusts. *Geological Magazine*, 6(5):204–205.

Steck, A.
1999. *Carte tectonique des Alpes de Suisse occidentale et des régions avoisinantes*. Service hydrologique et géologique national.

Termier, P.
1906. *La synthèse géologique des Alpes*.

Termier, P.
1922. A la glorie de la terre: souvenirs d'un geologue.

Tollmann, A.
1973. *Grundprinzipien der alpinen Deckentektonik*. Deuticke.

Trümpy, R.
1980. *Geology of Switzerland: An outline of the geology of Switzerland*. Interbook.

Trumpy, R.
1991. The glarus nappes: A controversy of a century ago: in modern controversies in geology (proceedings of the hsu symposium edited by dw muller, ja mckenzie, and h. *Weissert: Academic Press, London*, Pp. 385–404.

Turcotte, D. and G. Schubert
2014. *Geodynamics*. Cambridge university press.

Voight, B.
1976. *Mechanics of thrust faults and decollement*, volume 32. Halsted Press.

Wang, K. and Y. Fialko
2015. Slip model of the 2015 mw 7.8 gorkha (nepal) earthquake from inversions of alos-2 and gps data. *Geophysical Research Letters*, 42(18):7452–7458.

Wissing, S. and O.-A. Pfiffner
2003. Numerical models for the control of inherited basin geometries on structures and emplacement of the klippen nappe (swiss prealps). *Journal of structural geology*, 25(8):1213–1227.

Yamato, P., T. Duretz, and S. Angiboust
2019. Brittle/ductile deformation of eclogites: insights from numerical models. *Geochemistry, Geophysics, Geosystems*.

Yuen, D., L. Fleitout, G. Schubert, and C. Froidevaux
1978. Shear deformation zones along major transform faults and subducting slabs. *Geophysical Journal International*, 54(1):93–119.

CHAPTER 5

Summary

5.1 Main results

Chapter 2

A ductile shear zone which is generated spontaneously by thermal softening during a velocity-driven bulk deformation exhibits the following fundamental features: (1) After a transient period of temperature increase the temperature in the shear zone remains constant for linear viscous flow and quasi-constant for power-law viscous flow. (2) The shear stress in the shear zone is largest at the onset of shear zone formation and subsequently decreases towards a (quasi-)constant value associated with the establishment of a (quasi-)constant temperature. (3) The width of temperature variation across the shear zone is 6 to 8 times wider than the variation of the corresponding finite strain. Therefore, the shear zone does not exhibit a sharp, and hence easily observable, temperature variation between highly-strained shear zone and little-strained wall rock. (4) The shear zone is continuously widening during shearing due to thermal conduction between shear zone and wall rock.

Different versions of the Brinkman number can predict the onset of shear zone generation by thermal softening.

We determined that the thickness of shear zones is driven by thermal conduction. The thermal thickness is:

$$W_{\mathrm{T}} \approx 2\sqrt{\kappa t}, \tag{5.1}$$

and the shear zone thickness (observable, finite strain thickness)

$$W_{\gamma} \approx \frac{W_{\mathrm{T}}}{7} \tag{5.2}$$

We derived a new analytical formula that predicts the maximal temperature inside the shear zone:

$$T_{\max} \approx -1.13\ \frac{Q}{nR}\left[\ln\left(\frac{\Delta v^2 nR}{\lambda Q}A^{-\frac{1}{n}}\left\{\frac{\Delta v}{\sqrt{\kappa t}}\right\}^{\frac{1}{n}-1}\right)+1.1\right]^{-1}. \tag{5.3}$$

This temperature prediction requires only information on the bulk deformation, such as far-field velocity, flow law and thermal parameters, and, therefore, no *a priori* knowledge of the shear zone itself, such as thickness, flow stress and strain rate. Temperature predictions across the scales of geological velocities show first order agreement with several natural shear zones including Alpine basement nappes, eclogite shear zones and pseudotachylites. We show with 1D, 2D and 3D numerical simulations that this temperature prediction is valid for shear zone generation under both bulk simple and pure shear.

Our results indicate that shear zone generation by thermal softening likely occurs during lithosphere deformation in the continental lower crust and the mantle lithosphere for typical lithospheric velocities of few cm.yr^{-1} or bulk strain rates between 10^{-16} and 10^{-14} s^{-1}. For these deformation conditions, shear stresses of few hundred MPa can already cause shear zone generation by thermal softening.

Based on our results and their application to lithospheric flow laws and deformation conditions, we argue that spontaneous shear zone generation by thermal softening is a

feasible and likely the primary mechanism for spontaneous lithospheric scale shear zone generation. Thermal softening is probably a key constituent of subduction initiation, for example, at a thinned passive continental margin. Additional processes, such as grain size reduction, fabric development or fluid-related reactions can cause additional softening during progressive shear zone evolution and likely intensify the strain localization.

Chapter 3

We show with 2D thermo-mechanical numerical simulations that induced SI occurs due to thermal softening at passive margins with exhumed sub-continental mantle. SI occurs for convergence velocities of 2 cm.yr^{-1}, Moho temperatures between 525 and 600 °C and reasonable maximal deviatoric stresses around the Moho of ca 800 MPa. For the presented configuration, subduction initiates in the margin region of thinned continental crust. The modeled SI agrees with subduction scenarios that are geologically reconstructed for the closure of the Piemont-Liguria basin during the western Alpine orogeny.

The temperature in the mantle shear zone can be predicted with the analytical formula presented in Chapter 2.

Chapter 4

Inherited mechanical heterogeneities, such as (1) a lateral heterogeneity due to the basement-cover interface that is characterized by half-grabens and horsts, and (2) a vertical heterogeneity due to alternating sedimentary layers with different mechanical strength, can have great impact on the crustal deformation of shortening passive margin. The detachment, the sub-horizontal transport and the stacking of two nappes can be reproduced with visco-elasto-plastic rheology and standard flow-laws. The detached and horizontally transported units resemble a thrust nappe. Structures resembling fold nappes form by the ductile closer of a half-graben and the associated extrusion of the sedimentary half-graben fill; in agreement with previous modelling studies. The thrust nappe exhibits a larger horizontal displacement than the fold nappe so that the thrust nappe can be stacked above the fold nappe.

Based on the first-order agreement between model results and natural data, we propose a "nappe theory" for the Helvetic nappe system of Western Switzerland: The pre-Alpine configuration of the European passive margin was characterized by mechanical heterogeneities resulting from (i) a basement-cover contact with half-grabens and horst, and (ii) the alternation of mechanically strong carbonate and weak shale-rich sediment units. During the Alpine continental collision, the passive margin is shortened due to external compressive stresses; bouyancy forces probably played a minor role. The large-scale deformation configuration was close to the one applied to model tectonic wedges. During the margin deformation, mechanical heterogeneities control the detachment, transport and stacking of nappes. The sedimentary units of the Wildhorn super-nappe are detached due to the existence of a horst, or basement high, causing stress concentrations and brittle-plastic shear bands, eventually detaching the sedimentary units. The Wildhorn super-nappe was transported above weak shale-rich units and weak Ultrahelvetic units, which have been entrapped from above to below the Wildhorn super-nappe. Formation of the Morcles fold nappe occured by dominantly ductile closing of a half-graben, bounded by

basement massifs that form now the Aiguilles-Rouges and Mont-Blanc massifs, and the associated squeezing-out of sediments from this half-graben. The above described "nappe theory" can be calculated self-consistently with a thermo-mechanical theory, based on continuum mechanics, and with standard creep flow laws and a Drucker-Prager yield criterion, which are both based on rock deformation experiments.

5.2 Outlook

In Chapter 2 we provided a theoretical investigation on ductile strain localization by thermal softening. Although this model was derived from fundamental laws of nature, it would be interesting to design experiments and test the applicability of the model for deforming rocks. The localization criteria could be tested easily, as localized vs. distributed deformation is easily detectable in rock samples. Alternatively, the temperature prediction could be tested as well if one can find a reliable way to record the in-situ temperature (e.g. thermo-couple, infrared camera).
An alternative direction could be including other rheological weakening mechanism in the models, on top of shear heating. Here the list of possibilities is close to infinite. For small ΔT, maybe the two most critical addition could be the addition grain-size evolution and fluid related weakening. For large ΔT, the most important would be to include phase-transitions and reactions coupled to the thermo-mechanics.

The aforementioned mechanisms are possibly relevant also for forced subduction initiation. However, only staying to the proposed physical model, a systematic study of subduction initiation with different geometries and rheologies, would be desirable.

In Chapter 4 we propose a "nappe theory" for the Helvetic nappe system. However, there are some aspect we did not investigate and that is feasible with the current computational power. A possibility would be to have systematic simulations with varied slope of the model domain, representing the flexure of the subducting plate. An other possibility for example is to have inclined strong layers representing syn-rift sedimentation or transition of sedimentary facies in a prograding system. This would be desirable, since in our models we had clearly too much of the Helvetic sediments. Once two orders of magnitude higher computational power will be available (that should happen within 5-10 years) it would become possible to either resolve mylonite shear zones in this configuration or to resolve nappes with the same details as we did here, in a lithospheric scale model with self-consistently developing orogenic wedge.

Acknowledgements

First and foremost I would like to thank Stefan, for giving me the opportunity to work in the group. I am grateful that you gave me the freedom to spend nearly three years to works on a 1D code and for letting me to do some extra teaching assistance instead of working on the webpage. You managed to create a really vibrant and motivating environment, and you put together a group, where I could learn a lot from the others as well. I think it will be a real challenge to find a better group.

Yuri, thank you for organizing the Friday research seminars. It was a great fun to learn more about thermodynamics and numerics. I am also really glad I had the opportunity to work with you and to learn about the art of dimensional analysis and scaling.

Thibault, thank you for not only taking care of my professional development but also of my social life, when I just arrived to Lausanne. I really enjoyed those dinners and drinks. Of course, Cindy, thank you too.

I would like to thank all you guys in the numerics-tectonics group: Thibault, Vangelis, Annelore, Cindy, Josh, Lorenzo, Luda, Ludo, Richard, Sam, Yoann. Your enthusiasm was really motivating, and it is really cool that there was always someone I could ask, if had some problems. I am also grateful for the having some great fun during the "post-curricular activities".

Special thanks to Annelore, Ludo and Yoann, for helping me to survive with my French.

I thank Jean-Luc, Lukas and Othmar for the discussions on structural geology and petrology either on field trips or during coffee breaks. Gyuri, some of our discussions were quite fruitful and it was great to speak Hungarian with someone time to time.

I would like to thank for all members of ISTE for being such welcoming and friendly people.

I also would like to thank Anne, Anne-Marie and Krystel, for being always super kind and helpful.

Finally, I thank my family and my friends for the support and for making sure I have some fun, when I'm visiting home.